REVIEW

Check for updates

Advances in the designs and mechanisms of MoO₃ nanostructures for gas sensors: a holistic review

Ritu Malik,[a] Nirav Joshi[b] and Vijay K. Tomer [iD] *[c]

The rapid expansion and development of industrial sectors and corridors pose a significant threat to the world today owing to the deteriorating air quality resulting from the release of harmful and toxic gases into the atmosphere. To combat and tackle air pollution, reliable and precise sub-ppm detection of these gases is highly desirable for human safety and the environment. For a gas sensor to perform its level best, the choice of nanomaterials is a critical factor that can significantly impact the robustness, stability, cost-effectiveness, sensitivity, and selectivity of the sensing device. Molybdenum trioxide (MoO_3), as an n-type semiconducting metal oxide, has been rated as a research hotpot material in recent years due to its utility in a wide range of important technological applications. Owing to the advancement of synthetic techniques, it has been made possible to explore numerous novel nanostructures and integrate them into smart gas sensing devices. In this quest, this review is an effort to highlight the various nanostructures of MoO_3 and the influence of these morphologies on the gas sensing performance. A detailed morphological overview of pristine MoO_3 nanomaterials ranging from one-dimensional (1-D) to three-dimensional (3-D) nanostructure formation, followed by the preparation of different heterostructures including MoO_3/metal oxides (p-type and n-type), MoO_3/noble metal decoration, and MoO_3/2D materials in the thematic domain of gas sensing, has been presented. Finally, a future outlook on the further progress of MoO_3 gas sensors based on the current scenario is also suggested.

Introduction

Recent advancement in technology and its rapid adoption by the society has indeed marked an unparalleled impression on the quality of our lives. Nevertheless, the increasing usage of energized devices and various other components to sustain the routine lifestyle has undoubtedly harmed Earth with increased emissions of toxic and greenhouse gases and the spilling of hazardous chemicals/substances into the atmosphere.[1–5] As a consequence, the last two decades have witnessed a surprising upsurge in environmental monitoring technologies along with routine industrialization. One important aspect in mitigating environmental pollution is monitoring toxic and hazardous gases, where the search for faster, more sensitive, and low power consumption gas sensors is never-ending.[6–10] As an example, the efficient and quick detection of harmful gases as a result of accidents at petrochemical plants/sewage plants/mines could not only save money but also many important lives[11–15] with the

assistance of a distributed network of gas sensors.[16,17] A single sensor in such a network should accurately identify gases present in a complex mixture, be sensitive enough to detect harmful gases at lower concentrations, function at low power consumption, and be cheap enough to provide high spatial resolution across a wide range of sensors.[18–22] Yet, commercially available gas sensors are not mature with respect to some of these characteristics. In particular, the selectivity between NH_3, NOx, and CO for room temperature operation is still a matter of concern for commercially available gas sensors, particularly in the low ppm range.[23–26] Besides, most of the existing gas sensors work at temperatures tens or hundreds of degrees above room temperature and require a huge amount of power for their functioning.[27–29] So far, numerous gas sensors including acoustic, electrochemical, optical, and resistance have been developed based on their working principle; however, metal oxide (MOx)-based resistive gas sensors have enjoyed a privilege over other materials due to their high sensitivity, easy fabrication, lightweight, low fabrication cost, and simple detection method.[5,30–35]

Molybdenum trioxide (MoO_3) is an intriguing wide band gap n-type semiconductor with three unique polymorphous crystalline forms—orthorhombic α-MoO_3 (thermodynamically stable phase), monoclinic β-MoO_3 (low temperature metastable phase), and hexagonal h-MoO_3 phases.[36–40] MoO_3 has several merits such as a unique layered structure, tunable band gap (2.8–3.6 eV),

[a] *Department of Physics, D.C.R. University of Science & Technology, Murthal-131039, Haryana, India*

[b] *São Carlos Institute of Physics, University of São Paulo, CP 369, São Carlos 13560-970, São Paulo, Brazil*

[c] *Department of Materials Science & Nanotechnology, D.C.R. University of Science & Technology, Murthal-131039, Haryana, India. E-mail: vjtomer@gmail.com*

high electron mobility, low cost-phase-controlled synthesis, non-toxicity, and excellent electrochemical property, which prompts increasing interest in this fascinating material. In particular, α-MoO$_3$ has excited the research community with its layered anisotropic structure wherein the layers are parallel to the (010) crystal plane.[41–43] Every layer is composed of two further sublayers, which are formed by corner-sharing MoO$_6$ octahedra along the [001] and [100] directions. The two sublayers then bind together with van der Waals forces by sharing the edges of the octahedra along the [001] direction to form MoO$_6$ octahedra layers.[44,45] These layers then alternately stack along the [010] direction to form an α-MoO$_3$ structure.[46–48] This unique layered structure of α-MoO$_3$ increases the content of pentavalent Mo^{5+} ions, which possesses strong affinity to oxygen.[49,50] Since gas sensors function by the reaction between oxygen and the adsorbed analyte gas molecules, the presence of Mo^{5+} increases the adsorption effect, thus resulting in enhanced gas sensor response.[49,51–54] In recent times, MoO$_3$-based gas sensors have been intensively investigated for determining the trace concentration of toxic gases such as NO$_2$,[55] H$_2$,[56] ethanol,[57] CO,[58] NH$_3$,[59] and triethylamine.[60] The main governing factors that affect the sensitivity of a gas sensor are its size, morphology, and structure.[61,62] Thus, great efforts are being invested so as to improve the gas-sensing performance of MoO$_3$ by incorporating tailored nanostructures with controlled shapes, sizes, and morphologies. Owing to this, nanostructured MoO$_3$ with zero-dimensional (0-D), one dimensional (1-D), two dimensional (2-D), and three dimensional (3-D) morphologies have been synthesized (Scheme 1) employing various synthesis methods such as hydrothermal,[63] solvothermal,[64] sol–gel,[65,66] co-precipitation,[67] physical vapor deposition,[68] thermal evaporation,[69] RF magnetic sputtering,[54] chemical vapor deposition,[70] and spray-pyrolysis.[71]
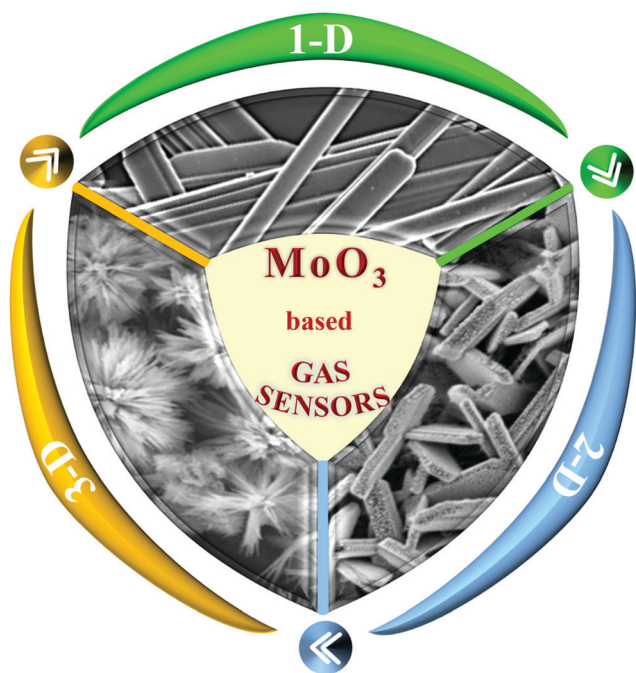
Also, because of its intrinsic structural anisotropy, α-MoO$_3$ has demonstrated rich nanostructured morphologies; therefore, in the past few years, efforts have been made to enhance the sensitivity and enable the sensor to perform at low concentration by designing nanostructures that not only possess high crystallinity but also high surface to volume (S/V) ratio such as nanobelts,[72,73] nanorods,[74,75] nanofibers,[76,77] nanoplates,[78,79] nanosheets,[80,81] nanowires,[82] and nanoflowers.[83,84] In particular, a high S/V ratio enables the swift diffusion of analyte gas molecules into the sensor layer, thus resulting in quicker response, higher selectivity, better sensitivity, and lower power consumption; however, the selectivity and operation temperature remain major constraints for MoO$_3$-based gas sensors. To overcome these challenges, great progress has been achieved in the recent past, which is reflected in the increased number of scientific articles primarily focusing on the formation of heterostructures, surface functionalization with a noble metal, and use of light illumination.[85–89]

Considering these aspects, a review article is the need of hour, which can summarize the latest happenings in gas sensing technology while putting forth a detailed morphological investigation of nanostructured MoO$_3$ in the current scenario of the sensing domain. This review has been drafted in line with the holistic coverage of MoO$_3$-based gas sensors since it is one of the metal oxide materials that have experienced excessively increased interest in the recent years (Scheme 2). Although there are many reports on the detection of harmful and toxic gases using resistive gas sensors,[25,29,30,90–95] none such review on MoO$_3$ could be located in the research database, which can provide a holistic overview of the sensing abilities and performances of this rising star of the SMOx family. The review is divided into three main sections, which provide an in-depth overview of the detection of hazardous gases using different MoO$_3$ nanostructures (1-D, 2-D, and 3-D). Different morphologies of MoO$_3$ in relation to their gas sensing attributes are addressed, while key challenges and future research perspectives have been discussed, which could serve as a roadmap for exploring this fascinating material not only for gas sensing but also for other technologically important applications.

Scheme 1   Schematic of the illustration of various morphologies of the MoO$_3$-based gas sensor.
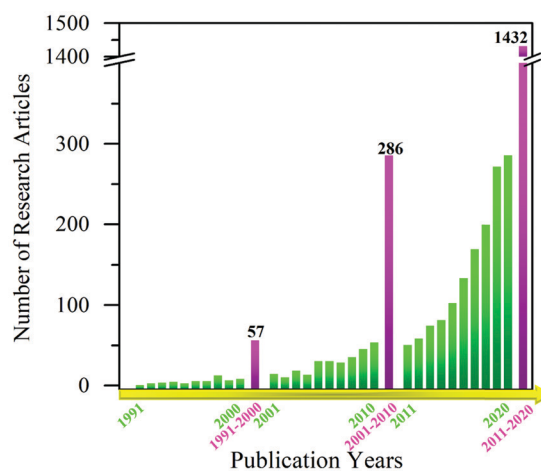
Scheme 2   Yearly publications demonstrating the increasing interest in MoO$_3$-based gas sensors in the last three decades (Source: ISI Web of Science database and search criteria 'MoO$_3$ + gas sensor').

Open Access Article. Published on 01 June 2021. Downloaded on 7/5/2021 5:20:53 PM. This article is licensed under a Creative Commons Attribution-NonCommercial 3.0 Unported Licence.

One dimensional (1-D) MoO₃ nanostructures for gas sensors

In recent years, the development of 1-D MoO$_3$ nanostructures with a high S/V ratio has received tremendous attention due to their speedy charge transfer throughout one spatial dimension in the range of 1–100 nm.[96–98] 1-D nanostructure materials consist of a networked structure, which reduces agglomeration while simultaneously facilitating the diffusion of the analyte gas molecules on the material surface.[99,100] Ultralong 1-D structures are known for providing a direct transport path for electrons to propagate along the axis, which greatly enhances the gas sensing performance. Moreover, gas sensors made of these 1-D nanostructures offer ultra-sensitivity, fast response, higher stability, low-temperature operation, and less power consumption.[101,102] To date, a variety of 1-D nanostructures including nanobelts,[60,72,73,96,99,101–105] nanoribbons,[56,59,100,106,107] nanorods,[74,75,97,108–113] nanofibers,[76,114] nanowires,[82] and microrods[98,115,116] of MoO$_3$ have been utilized in gas sensors and the following section summarizes these nanostructures with their gas sensing performance and mechanism. An overview of gas sensors based on 1-D MoO$_3$ nanostructures is listed in Table 1.

MoO₃ nanobelts (NBs)

Nanobelts of MoO$_3$ are one of the most prominent 1-D morphologies that have attracted huge attention owing to their single crystalline nature and large aspect ratio. It is due to their faceting nature, which makes NBs suitable candidates for probing size- and dimensionality-dependent physical or chemical phenomena. Yang et al.[103] prepared NBs of Zn-doped MoO$_3$ using the hydrothermal (HT) method and demonstrated the ethanol sensing performance. The group prepared the nanocomposites in various Mo/Zn ratios, and the FESEM images in Fig. 1a–f reveal that the increase in the Zn ionic content in the layered MoO$_3$ causes an increase in the spaces between its layers to accommodate more Zn ions, thereby broadening the width of the MoO$_3$ nanobelts. The operating temperature (OT)-dependent response toward 1000 ppm ethanol gas in Fig. 1h reveals that Zn doping in MoO$_3$ not only causes depreciation in the OT by 100 °C but also enhances the

Table 1 A detailed overview of the gas sensing performance using 1-D MoO$_3$-based gas sensors

Class	Material	Synthesis method	Gas	Conc. (ppm)	Operating temp. (°C)	Response	Resp./Reco. time (s/s)	Ref.
Nanobelt	MoO$_3$/Fe$_2$(MoO$_4$)$_3$	Hydrothermal	Toluene	50	250	5.3	<30/<30	191
	MoO$_3$/ZnO	Hydrothermal	Ethanol	100	250	19	2.5/3.5	192
	MoO$_3$	Hydrothermal	Ethanol	800	300	174	42^a/4^a	193
	Zr/MoO$_3$	Hydrothermal	Xylene	100	206	7.99	32/264	194
	MoO$_3$/Fe$_2$O$_3$	Hydrothermal	Xylene	100	206	6.9	87/190	195
	Ce/MoO$_3$	Hydrothermal	TMA	50	240	17.4	<10/<20	196
	MoO$_3$	Chemical spray pyrolysis	NO$_2$	100	200	68(%)	15/150	55
	Fe/MoO$_3$	Hydrothermal	Xylene	100	206	6.1	20/75	117
	Au/MoO$_3$	Hydrothermal	1-butyl amine	100	240	300	23/388	197
	In$_2$O$_3$/MoO$_3$	Hydrothermal + chemical synthesis	TMA	10	260	31.69	6/9	198
	Zn–MoO$_3$	Hydrothermal	Ethanol	1000	240	321	15/121 (100 ppm)	103
	RuO$_2$/MoO$_3$	Chemical synthesis	TEA	1	260	12.8	2/10	60
	Fe$_2$O$_3$/MoO$_3$	2-Step hydrothermal	Xylene	100	233.5	22.48	4/102	104
	CoMoO$_4$/MoO$_3$	Hydrothermal + dipping-annealing process	TEA	100	220	104.8	<10/<10	105
	Au/MoO$_3$	Hydrothermal + chemical synthesis	TMA	50	280	70	6/9	72
	Pt/MoO$_3$	Hydrothermal + chemical reduction	Formaldehyde	200	RT	39.3	17.8/10.5 (100 ppm)	73
	W/MoO$_3$	Hydrothermal	TMA	50	200	13.8	6/11	101
	Pd/MoO$_3$	Spray pyrolysis + chemical dip	NO$_2$	100	200	95.2(%)	74/297	102
	Cd/MoO$_3$	Hydrothermal	H$_2$S	100	140	378.5	23/45 (50 ppm)	96
	MoO$_3$	Hydrothermal	TMA	50	240	582	15/50 (1 ppm)	99
Nanoribbon	MoO$_3$	Hydrothermal	H$_2$	1000	200	14.1	21/75	100
	MoO$_3$/Graphene	Hydrothermal	H$_2$	1000	RT	20.5	10/30	106
	MoO$_3$	Hydrothermal	H$_2$	1000	RT	17.3	10.9/30.4	56
	MoO$_3$	Hydrothermal	H$_2$	100	RT	3.2^a	3/16	107
	MoO$_3$	Hydrothermal	NH$_3$	25	450	60	21/216.9 (5 ppm)	59
Nanorod	NiCo$_2$O$_4$/MoO$_3$	Hydrothermal + chemical deposition	Ethanol	1	350	20	N.G.	74
	Ag–MoO$_3$	Hydrothermal + chemical reduction	TEA	100	200	408.6	3/107	75
	MoO$_3$	Hydrothermal	TEA	100	300	101.74	4/88	97
	MoO$_3$/BiVO$_4$	Hydrothermal + metal organic deposition	TEA	20	125	1.86	15/110	108
	MoO$_3$/GO	Solvothermal + annealing	NH$_3$	100	200	15.3	5/84	109
	MoO$_3$	Hydrothermal	NO$_2$	20	110	84	20/45	110
	h-MoO$_3$	Chemical bath technique	NH$_3$	50	200	67	183/202	111
	p-Si/MoO$_3$	Hydrothermal + physical vapor deposition	CO$_2$	100	250	12.08	8/15	112
	rGO/MoO$_3$	Hydrothermal + in situ microwave	H$_2$S	40	110	44.7	109/36	113
Nanofiber	SnO$_2$/MoO$_3$	Hydrothermal + wet chemical	CO	300	300	2.4	1430/1524	76
	MoO$_3$	Hydrothermal	Ethanol	100	275	25	45/138	114
Nanowire	MoO$_3$	Hydrothermal	H2	1.5(%)	260	0.85	28/42 (500 ppm)	82
Microrod	MoO$_3$	Hydrothermal	Ethanol	500	332	8.24	N.G.	98
	MoO$_3$	Probe sonication	TMA	1000	200	2533	8/9 (1 ppm)	115
	h-MoO$_3$	Microwave assisted hydrothermal	Acetone	10	200	1.48	60/500	116

^{a} Not given.

© 2021 The Author(s). Published by the Royal Society of Chemistry
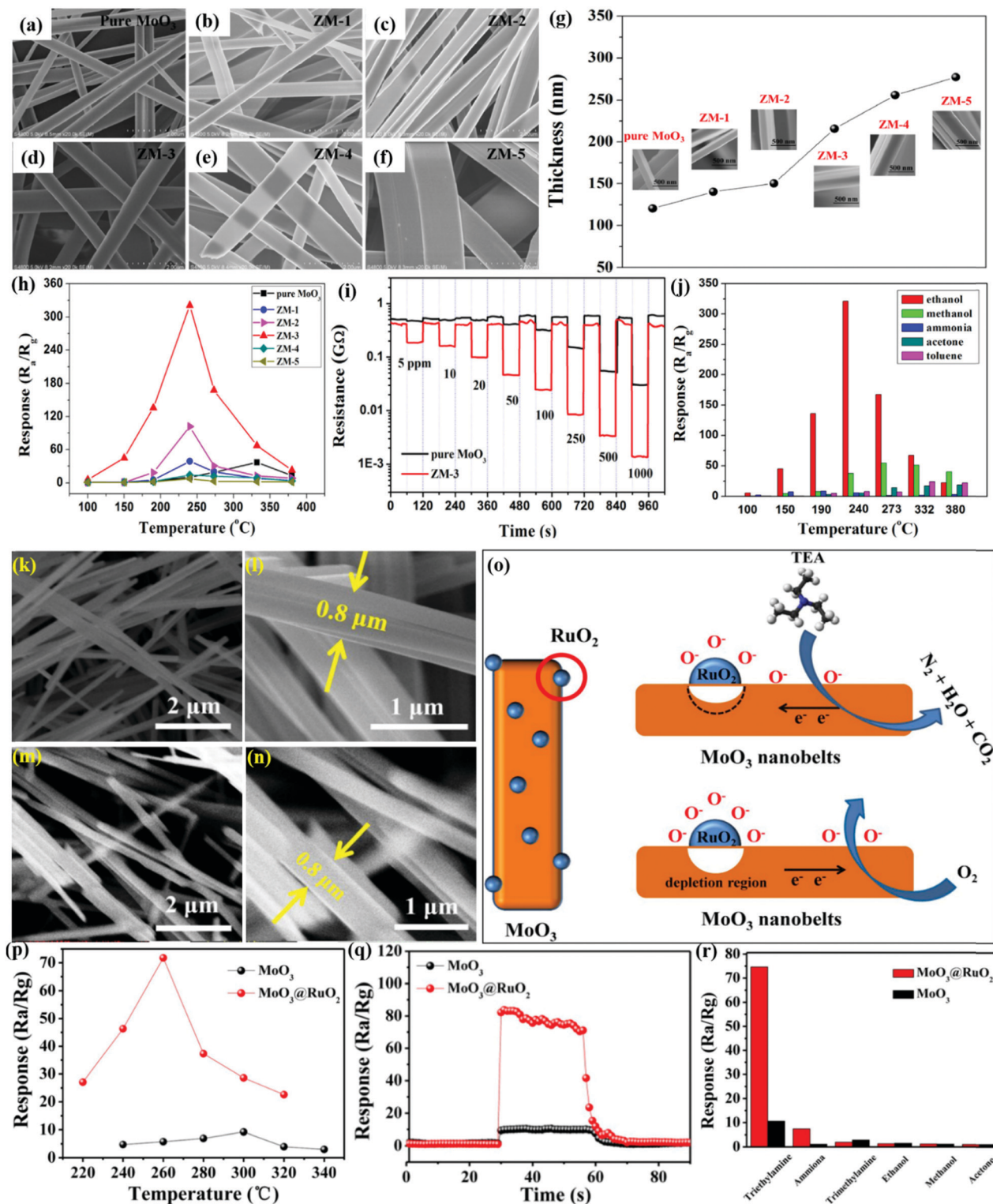
Fig. 1 (a–f) FESEM images of pure MoO₃ NBs and ZM-1–ZM-5; (g) the average thicknesses of pure MoO₃ NBs and Zn-doped MoO₃ NBs; (h) gas sensing responses of the sensors based on pure MoO₃ NBs and Zn-doped MoO₃ NBs to 1000 ppm ethanol at different OTs; (i) response and recovery curves of the sensors based on pure MoO₃ NBs and ZM-3 to different concentrations of ethanol at the OT of 240 °C; (j) cross-sensitivity to various gases at different temperatures; reproduced with permission from ref. 103, copyright 2017 Elsevier. (k and l) FESEM images of pure MoO₃ NBs; (m and n) FESEM images of RuO₂/MoO₃ NBs; (o) schematic diagram of the possible gas sensing mechanisms of RuO₂/MoO₃ NBs; (p) response to 10 ppm TEA gas *versus* OT; (q) response transient to 10 ppm TEA at 300 °C; (r) responses of pristine and RuO₂/MoO₃ NBs gas sensors to different gases (10 ppm) at 300 °C. Reproduced with permission from ref. 60, copyright 2019 Elsevier.

response at least 15 times than pure MoO_3 NBs. Besides, the response (T_{res}) and recovery (T_{rec}) transients to different concentrations of ethanol at the OT of 240 °C in Fig. 1i display good reversibility along with a selective response to the ethanol gas was also observed among the other tested gases in Fig. 1j. The improved gas sensing performance was accredited to the increased ethanol concentration, enhanced dehydrogenation progress at a lower temperature, diminishing probability of ethoxy recombination, and the narrowed band gap owing to Zn doping. To further promote the sensing properties and selectivity improvement, the combination of two metal oxides could be an ideal method. For example, Wang and his group[60] combined MoO_3 NBs with RuO_2 nanoparticles by a simple soaking method and demonstrated that the prepared $MoO_3@RuO_2$ nanocomposites had superior sensing characteristics. The morphology of the NBs (diameter ~ 0.8 μm) was confirmed in the FESEM results as displayed in Fig. 1(k and l); however, no apparent change in the morphology and dimension of the MoO_3 NBs was observed on account of the addition of RuO_2 nanoparticles (Fig. 1(m and n)). Due to the n-type behavior of pristine MoO_3 NBs and $MoO_3@RuO_2$ nanocomposites, it was quite evident that pristine MoO_3 NBs demonstrated an impressive sensing performance (Fig. 1o) while the electronic movement greatly impacted the resistance of the nanocomposite. While evaluating the sensing response for triethylamine (TEA) gas, the results in Fig. 1p illustrated that an OT dependent response of 9.22 and 71.43 was observed at 260 °C and 300 °C for MoO_3 NBs and $MoO_3@RuO_2$ nanocomposites, respectively. The transient response curve in Fig. 1q not only illustrated a fast response and recovery (2 s and 10 s) behavior for the prepared nanocomposites but also displayed the benefit of functionalization of pristine MoO_3 NBs with RuO_2 nanoparticles in enhancing the sensing properties. In addition, the histogram results in Fig. 1r also confirmed the good selective response of the $MoO_3@RuO_2$ nanocomposites for TEA gas. The TEA sensing mechanism in Fig. 1o illustrated that the existence of highly catalytic RuO_2 NPs significantly increases the resistance of the nanocomposites in air. Also, the O_2 molecules in air tend to get absorbed to generate oxide ions while a great mass of electron is trapped onto the oxygen. These electrons flow from MoO_3 to RuO_2 to generate a potential barrier at their interface, which gets reduced in the TEA atmosphere, thus causing 5 times greater response for the $MoO_3@RuO_2$ nanocomposites than that of pure MoO_3 NBs.

Xylene is a toxic and colorless VOC, whose over exposure results in cardiovascular and kidney problems. To detect xylene, the formation of n–n heterostructures is a novel approach, following which the group of Qu et al.[104] detected xylene gas by preparing an n–n type heterostructure comprising of Fe_2O_3 NPs and MoO_3 NBs by a two-step HT method. The morphological analysis results in Fig. 2a and b shows that the MoO_3 NBs are ~ 200–300 nm in width while ~ 2–3 mm in length; also, the nanobelt structure of MoO_3 was retained even after uniformly doping Fe_2O_3 NPs (Fig. 2c and d). The sensor response to xylene gas at different OTs in Fig. 2e displayed that although pure MoO_3 detected xylene gas at a lower temperature than the Fe_2O_3/MoO_3 NBs, yet the former exhibited a lower maximum response than the nanocomposite. The selectivity results in Fig. 2f reveal that the response to xylene gas was the highest

for Fe_2O_3/MoO_3 NBs, and $\sim 250\%$ improvement in the sensitivity was observed than that using pure MoO_3 NBs. The research group attributed the superior sensing performance to the unique n-type heterojunction between MoO_3 NBs and Fe_2O_3 nanospheres. Another example was reported by Wang and co-workers[105] on very known p–n heterostructures because of their effective charge separation, long-life of the charge carrier to make them more favorable to achieve high sensor response, and selective sensing toward target analytes. They utilized a simple dipping-annealing process and developed p–n heterojunctions of $CoMoO_4$ and MoO_3. The MoO_3 NBs were smooth, having 100 nm thickness, 100–300 nm width, and a few micrometers length (Fig. 2g), while the rough surface of $CoMoO_4/MoO_3$ nanocomposites in Fig. 2h illustrated the successful growth of the $CoMoO_4$ NPs on the MoO_3 NBs. The TEM results in Fig. 2i and j further confirm the uniform dispersion of $CoMoO_4$ nanoparticles (20–50 nm diameter) on the surface of the MoO_3 NBs. The sensing results toward triethylamine (TMA) gas in Fig. 2k reveal that the $CoMoO_4/MoO_3$ nanocomposites-based sensors show better sensing performance while causing a reduction of 60 °C in the optimum temperature as compared to the pristine MoO_3 NBs. The sensing response as a function of TMA concentration in Fig. 2l reveals the stronger response (4-fold) of the nanocomposite to 200 ppm TMA than pure MoO_3, while the dynamic responses in Fig. 2m seem to be perfectly repeatable and reproducible during 3 cycles of switch 'on' and 'off' measurement. It was concluded that the formation of a potential barrier between $CoMoO_4$ (p-type) and MoO_3 (n-type), the stronger oxygen adsorption of $CoMoO_4$, and the formation of crystallographic defects all together resulted in superior sensing performance.

Noble metal NPs such as Ag, Au, Pt, and Pd, with their outstanding catalytic effect, have been known to improve the sensing attributes of the MoO_3 NBs. For instance, Zhang et al.[72] prepared catalytic Au NPs doped MoO_3 NBs via the hydrothermal method and displayed superior sensing performance to TMA gas. The MoO_3 NBs were 100–300 nm wide and 10–20 μm in size (Fig. 3(a and b)), while the FESEM image in Fig. 3c revealed that several Au NPs were stuck on the surface of the NBs. In addition, the HRTEM image in Fig. 3d displayed the non-continuous distribution of Au NPs (diameter ~ 10–20 nm) on the MoO_3 NBs surface, which confirms the high crystallinity of the MoO_3 NBs and Au NPs. The sensing response of the prepared materials toward TMA gas demonstrated an increase-maximum-decay (IMD) type of pattern with the increase in the OT (Fig. 3e). The OT has a considerable impact on the sensing performance of the material owing to the thermal energy of the analyte gas molecule for clearing the energy barrier of the surface reaction and later converting the adsorbed oxygen for further attracting the electrons from the semiconductor. The dynamic response-recovery curves in Fig. 3f displayed a fast response ($T_{res} \sim 7$ s) and recovery ($T_{rec} \sim 10$ s) time for $Au@MoO_3$ NBs toward 10 ppm TMA gas. Besides, the as-prepared materials also demonstrated the highest response to the TMA gas (Fig. 3g). Overall, the improved sensing performance was accredited to the catalytic Au NPs, which, with the help of reactive oxygen species, improves the electron exchange process between Au NPs and MoO_3.
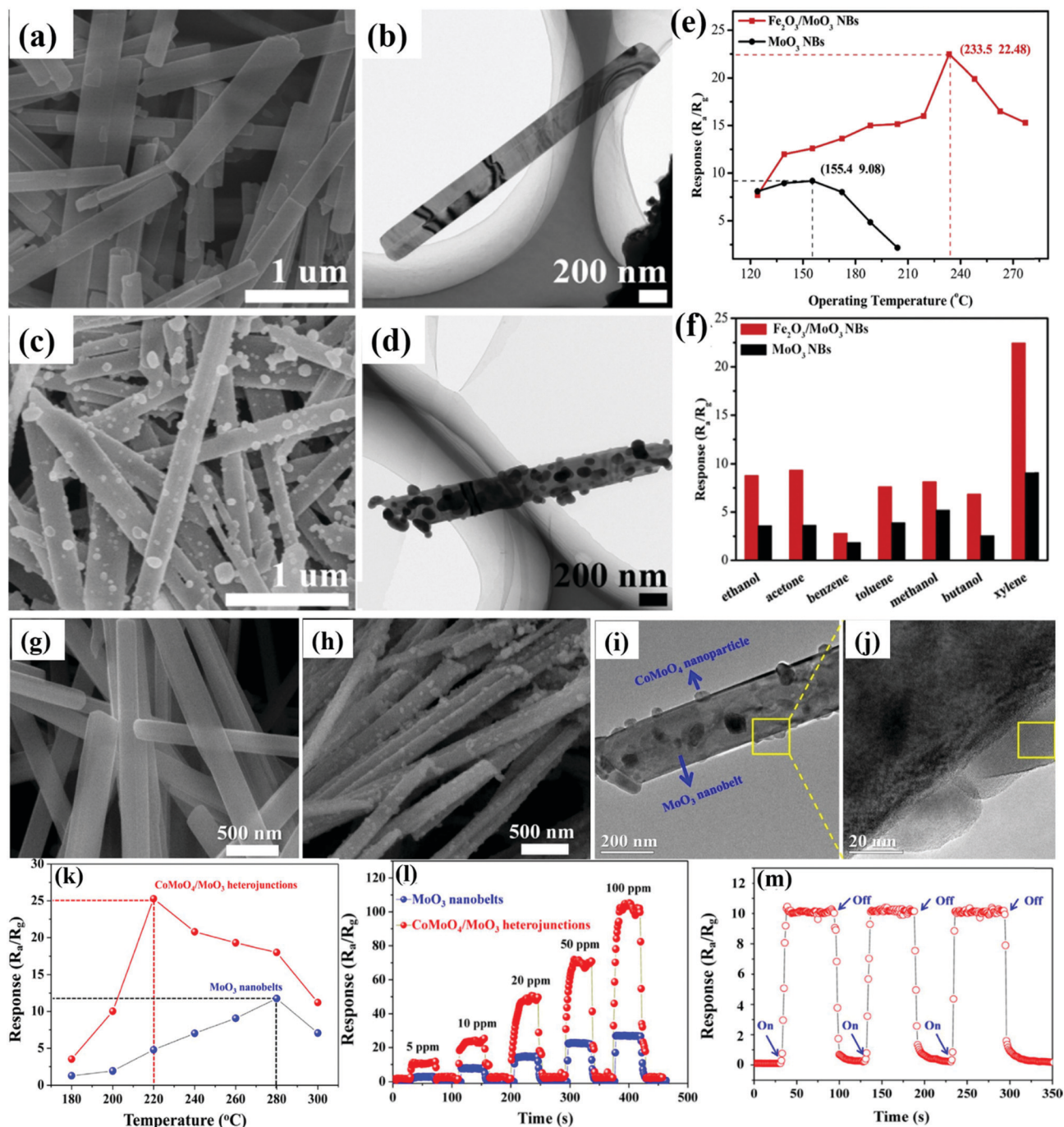
Fig. 2 (a and b) SEM and TEM image of pure MoO_3 NBs; (c and d) SEM and TEM image of Fe_2O_3/MoO_3 NBs; (e) OT dependent response of the sensors to 100 ppm xylene; (f) response of the sensors to 100 ppm various gases at their optimum OT. Reproduced with permission from ref. 104, copyright 2019 Elsevier. (g) FESEM image of pure MoO_3 NBs; (h) FESEM image of the $CoMoO_4/MoO_3$ nanocomposites; (i and j) low and high-magnification TEM images of the $CoMoO_4/MoO_3$ nanocomposites; (k) response of the sensors to 10 ppm of TMA at different OTs; (l) response and recovery curves toward different concentrations of TMA; (m) response and recovery curves of the sensor based on the $CoMoO_4/MoO_3$ nanocomposites to 5 ppm TMA after 3 cycles of gas on and off at 220 °C. Reproduced with permission from ref. 105, copyright 2018 Elsevier.

In the last couple of decades, the detection of VOCs in indoor environments has received much attention. VOCs are produced as a result of gaseous emission from commonly uses household products such as nail paints, wall paints, furniture, and cleansers, and cause both short- and long-term effects on human health. Formaldehyde (HCHO) is one of the VOCs found in many daily usage products, such as carpets, wood, and other plastic products widely used in every household. There have been several ways to enhance the selectivity of a sensor for a specific VOC and have remained a great topic of interest among researchers. For example, Gu and coworkers[73] prepared MoO_3 NBs using a facile HT method and surface-decorated
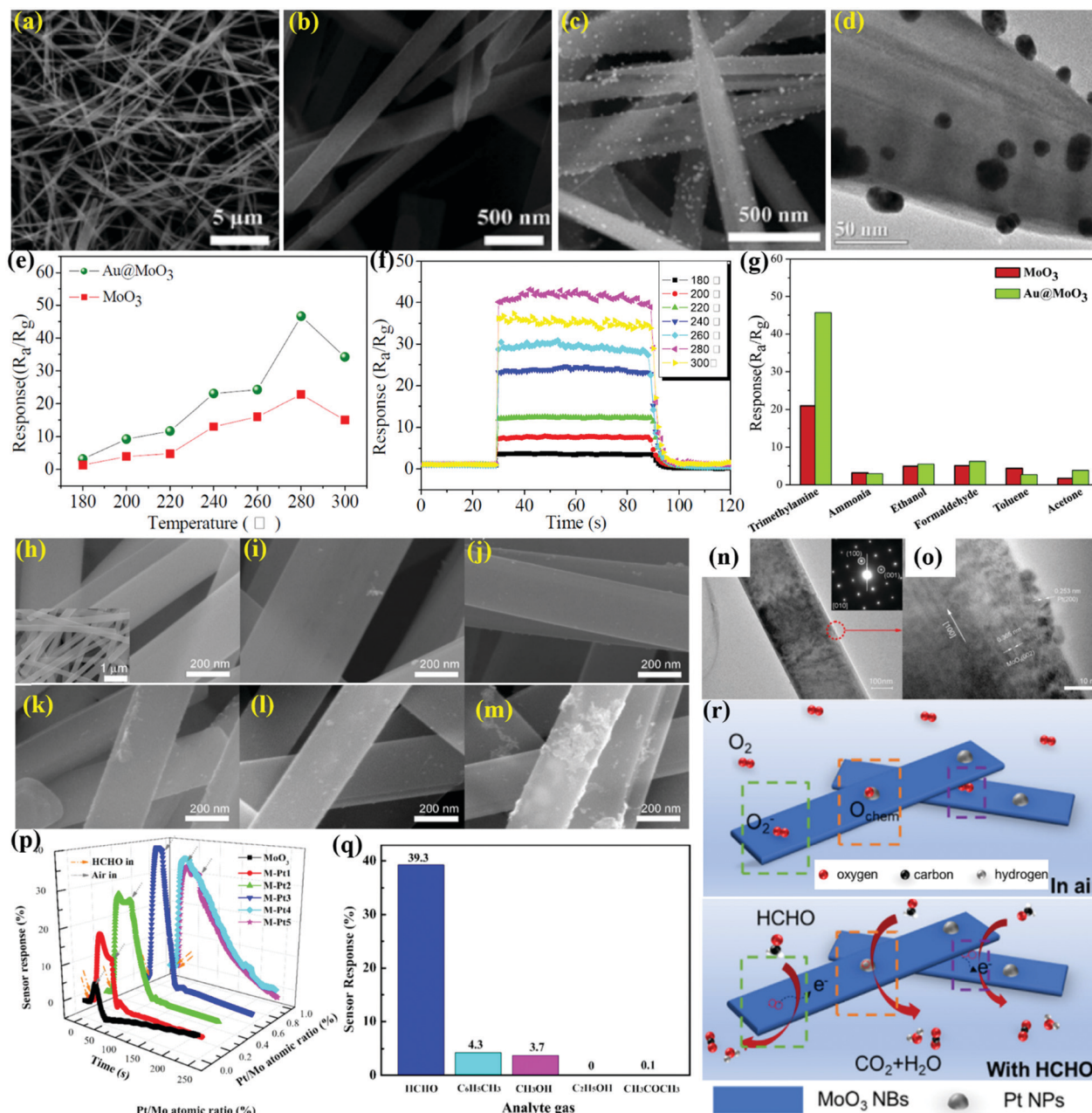
Fig. 3 (a and b) FESEM images of pure MoO_3 NBs, (c) FESEM image Au@MoO_3 nanocomposites; (d) TEM images of Au@MoO_3 nanocomposites; (e) response curves of the sensors to 10 ppm trimethylamine gas at different OTs; (f) response and recovery time curves of the sensors based on Au@MoO_3 NBs to 10 ppm TMA at different OTs; (g) response values of the Au@MoO_3 nanocomposites sensor toward 10 ppm different gases at the working temperature of 280 °C. Reproduced with permission from ref. 72, copyright 2016 Elsevier. (h) The SEM images of the pristine nanowires, the inset picture is a low-magnified SEM image; (i–m) SEM images of Pt/MoO_3 NBs; (n and o) TEM images of Pt-decorated MoO_3 NBs; (p) the dynamic sensor response of pristine and Pt/MoO_3 NBs toward HCHO gas of 200 ppm at 27 °C; (q) sensor response to different gases with concentrations of 200 ppm; (r) the schematic diagram for the HCHO sensing behavior of Pt/MoO_3 NBs in air and in HCHO-containing atmosphere. Reproduced with permission from ref. 73, copyright 2019 Elsevier.

them with Pt NPs to illustrate superior sensing response toward HCHO gas. The SEM image in Fig. 3h reveals the width of pristine MoO_3 NBs to be ∼200–400 nm with very minute thickness (inset). The other SEM images (Fig. 3(i–m)) further displayed the increasing presence of Pt NPs with its loading amount on the MoO_3 NBs. The TEM images in Fig. 3n and o for M-Pt3 (Pt-loading amount = 0.61%) not only confirm the

presence of the highly crystalline MoO_3 NBs but also reveal the occurrence of small Pt NPs on the surface of the MoO_3 NBs. The response results in Fig. 3p expose the poor performance of pure MoO_3 NPs, while with the appropriate Pt%-decorated MoO_3 (M-Pt3) NBs cause an improved sensing response to formaldehyde gas. An outstanding selectivity to formaldehyde gas among other interferent gases is illustrated in Fig. 3q. The M-Pt3 sensor

shows no response to ethanol, while a negligible response of 0.1% acetone was observed. The sensing mechanism in Fig. 3r reveals that the astounding sensing performance was due to the presence of highly catalytic Pt NPs, which reduces the adsorption activation energy of HCHO on the surface of MoO_3 and also assists in forming the spillover region around the Pt NPs on the surface of the MoO_3 NBs. Overall, according to the research reported by Xu et al.,[117] the oxygen species tends to preferably adsorb on Mo^{5+}, causing an increase in the intensity of chemisorbed oxygen on the surface of the NBs, thus enhancing the gas sensing response. In addition, the higher specific surface area of the NBs provides more absorption sites and contributes positively to gas sensor response.

MoO_3 nanoribbons (NRbs)

Similar to nanobelts, the nanoribbons (NRbs) morphology has been quite a popular 1-D MoO_3 morphology for preparing gas sensors with (especially, hydrogen sensor) great sensing performance in every aspect of response/recovery time, selectivity, stability, etc. In this quest, Yang and coworkers[100] prepared α-MoO_3 NRbs of various sizes by the HT method at different temperatures. The SEM images in Fig. 4a revealed the NRbs-like morphology wherein the dispersion and average length of the NRbs increase with the HT temperature. The double-layered MoO_6 octahedra in α-MoO_3 comprise of pentavalent ion Mo^{5+}-induced structural defects, which exhibits high affinity to hydrogen gas (Fig. 4b). The room temperature (RT) response toward hydrogen in Fig. 4c indicated an increase in the sensitivity with the HT temperature. Besides, the response/recovery speed was also found to increase on account of initially treating the sensors in the hydrogen atmosphere (Fig. 4d). The results pointed to the fact that an increase in HT causes an increase in chemisorbed oxygen and Mo^{5+} concentration. On the other hand, Mo^{5+} in the α-MoO_3 lattice becomes an obvious choice for the absorption of oxygen species; an increase in the Mo^{5+} concentration with increasing HT leads to the chemisorption of more oxygen species on the NRbs surface (red curve in Fig. 4e), which ultimately enhances the response to hydrogen gas.

Recently, 2-D materials have mostly been in focus for the development of gas sensors due to their outstanding electronic properties.[118–121] A suitable combination of these 2-D material with oxide nanostructures offers spontaneous electron transfer and ensures that the diffusion of gas molecules results in an improvement in the sensor response along with the optimization of the response/recovery times of the gas sensor.[122] Yang et al.[106] demonstrated a one-step HT method for uniformly loading orthorhombic MoO_3 NRbs on the exfoliated graphene oxide (GO) supporting layers (Fig. 4f–1). The SEM image in Fig. 4f–2 revealed that the as-synthesized products were composed of large amounts of NRbs (length ~10 μm) loaded on the graphene nanosheets, while MoO_3 NRbs were also clearly located on either side of the graphene nanosheet, as shown in Fig. 4f–3. The hydrogen sensing responses in Fig. 4g displayed the negligible response of pure graphene nanosheets despite the fact that a little addition of graphene in MoO_3 NRbs enhances the response and reduces the T_{res}/T_{rec} time considerably.

The selectivity results for the GO/MoO_3 NRbs in Fig. 4h further attest to the fact that the sensor responded perfectly to H_2 gas. Such a high response was credited to the formation of innumerable MoO_3/graphene heterojunctions (Fig. 4i) and also the high surface area of the nanocomposite as a result of adding the graphene networks, which not only loosened the structure but also enhanced the conductivity of the sensor.

Yang et al.[123] also prepared Fe-doped orthorhombic MoO_3 (α-MoO_3) nanoribbons and demonstrated superior H_2 sensing performance. The first-principles density functional theory (DFT) calculations were used to calculate the adsorption of O_2 and H_2 molecules on the surface of Fe/MoO_3 (Scheme 3). It was observed that oxygen was adsorbed parallel to the surface of Fe/MoO_3 in three modes, i.e., along the x-axis (mode O-1) with adsorption energy of −0.539 eV, y-axes (mode O-2) with adsorption energy of −0.461, or perpendicular to the plane of the Fe-doped MoO_3 (mode O-3) with adsorption energy of −0.673 eV. The results in Scheme 3a reveal that oxygen preferred to adsorb on Fe-doped MoO_3 in the O-3 mode. In addition, the H_2 molecules adsorbed parallelly to the oxygen ions on the surface of the Fe/MoO_3 while interacting with the pre-adsorbed oxygen ions. The difference in the electronic density in Scheme 3b indicated that the charges to the oxygen atoms numbered 1 was −0.09e, and those numbered 2 was −0.06e in the adsorbed oxygen molecule. This causes the transfer of −0.15e from the Fe–MoO_3 to the adsorbed oxygen molecule. These theoretical results further confirmed the capturing of the electrons from the adsorbed oxygen on the surface of Fe/MoO_3.

In most cases, metal oxide-based gas sensors operate at high temperatures (100–200 °C), which hinders the monitoring of the gas composition in explosive species environment since high temperatures could trigger an explosion. In this way, RT sensors are more favorable due to low power consumption, simplified manufacturing processes, and reduced operating costs.[124–128] Yang et al.[56] utilized a simple HT method to prepare MoO_3 NRbs and demonstrated superior hydrogen sensing performance. A ribbon-like morphology was observed in the SEM image (Fig. 4j) for pure MoO_3 with an average thickness, width, and length of ~90 nm, 270 nm, and 20 μm, respectively; however, the sample calcined in hydrogen gas atmosphere at 300 °C (Fig. 4k) demonstrated a depreciated size in all the dimensions as compared to the pristine MoO_3 NRbs. The room temperature response transients to H_2 gas in Fig. 4l revealed a typically n-type sensing performance and a fast response/recovery speed. Besides, the histogram results in Fig. 4m further indicated the excellent selectivity of the MoO_3 NRbs sensors toward H_2 gas. It was also revealed that the sample annealed in a hydrogen atmosphere was ~2.5 more responsive to H_2 gas compared to pristine MoO_3. The reason was the higher concentrations of Mo^{5+} and chemisorbed oxygen ions in MoO_3 treated at 300 °C (Fig. 4n) under hydrogen atmosphere, which triggered the redox reactions due to increased collision between H_2 and O_2^-.

MoO_3 nanorods (NRs)

Owing to the obvious advantages offered by the multi-component heterostructures, which included tunable chemical composition and synergistic properties, Yuan et al.[74] prepared 1D α-MnO_3 NRs
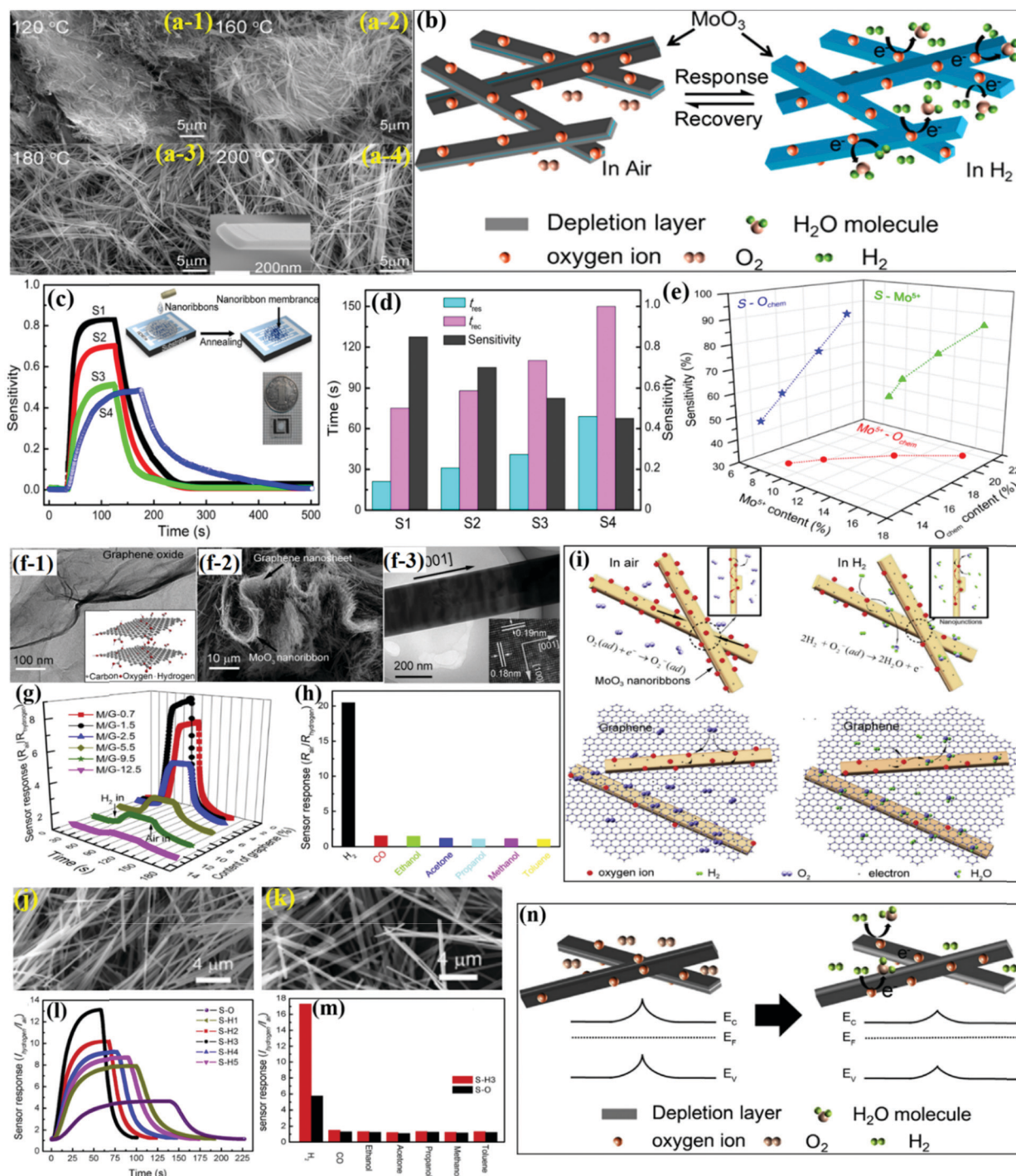
Fig. 4 (a) SEM images of the as-prepared samples synthesized at different OT; (b) schematic diagram of the H_2 sensing mechanism of MoO_3 NRbs; (c) dynamic response of different MoO_3 sensors toward 500 ppm of H_2; (inset) schematic illustration of the fabrication process of the sensor; (d) sensitivity, response time, and recovery time of different MoO_3 sensors; (e) relation among the sensitivity (S), Mo content, and O_{chem} content of the MoO_3 NRbs. Reproduced with permission from ref. 100, copyright 2015 American Chemical Society. (f-1) TEM image and schematic diagram of graphene oxide used as the hydrothermal precursor; (f-2) SEM image of the MoO_3 NRbs/graphene nanocomposite; (f-3) HRTEM images of individual MoO_3 NRbs; (g) the RT response curves of the MoO_3 NRbs/graphene to 500 ppm H_2 in air; (h) selectivity to 1000 ppm H_2 of M/G-1.5 against other gases with the same concentration; (i) schematic diagram of pure MoO_3 NRbs and MoO_3 NRbs/graphene under air and H_2-containing atmospheres. Reproduced with permission from ref. 106, copyright 2017 Elsevier. (j) SEM images of the original MoO_3; (k) SEM image of MoO_3 treated at 400 °C; (l) the dynamic response curves toward 750 ppm H_2 gas at 25 °C; (m) the selectivity of S-H3 to different gases with concentrations of 1000 ppm; (n) the schematic diagram of the H_2 sensing mechanism of the sensor based on MoO_3 NRbs both in air and in H_2 atmosphere. Reproduced with permission from ref. 56, copyright 2019 Elsevier.
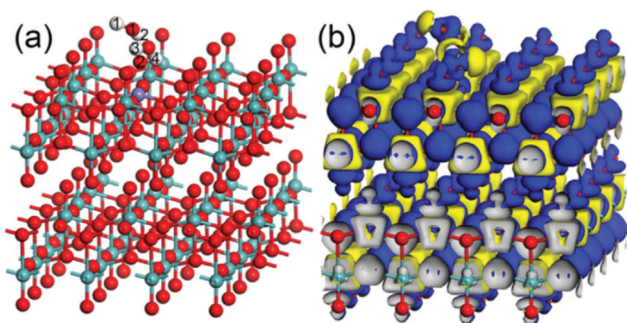
Scheme 3 The optimized structure (a) and the electronic density difference (b) of the adsorption of two H_2 on Fe-doped MoO_3 with one pre-adsorbed oxygen ion. The red, blue, and white balls represent the O, Mo, and H atoms. Reproduced with permission from ref. 123, copyright 2021 Elsevier.

using a facile HT method and used them as the backbone for growing porous $NiCo_2O_4$ nanosheets (Fig. 5a) *via* the chemical bath deposition (CBD) method. The FESEM results in Fig. 5b-1 and b-2 for α-MoO_3 NRs reveal its clean surface with uniform length (20 μm) and width (200 nm). A cluster of porous $NiCo_2O_4$ nanosheets coated on the surface of 1D α-MoO_3 NRs (Fig. 5b-3) further indicated a porous and complex surface of the $NiCo_2O_4$/α-MoO_3 composite. The gas sensing results in Fig. 5c displayed the negligible response of pure 1D α-MoO_3 NRs and $NiCo_2O_4$ toward ethanol, while the $NiCo_2O_4$/α-MoO_3 composite indicated a p-type semiconductor behavior. Furthermore, the $NiCo_2O_4$/α-MoO_3 composite showed good repeatability and excellent stability without any deviation in the response upon alternate purging of fresh air and 1 ppm ethanol vapor (Fig. 5d). The cross-responses to different gases in Fig. 5e also revealed the highest response of the $NiCo_2O_4$/α-MoO_3 composite toward the gas. The research group attributed the superior response to the unique heterostructure between α-MoO_3 and $NiCo_2O_4$, which, owing to their different acid–base and reductive–oxidative properties, promote the adsorption and oxidation of ethanol.

As stated earlier, the surface doping of SMOx with noble metals is also considered a brilliant approach owing to their higher catalytic activity.[129–134] In particular, Ag NPs, being comparatively cheaper and having higher catalytic performance, have been extensively explored in promoting the sensing performance of oxide-based sensors. Considering this, Tian *et al.*[75] successfully demonstrated the decoration of Ag NPs on the surfaces of α-MoO_3 NRs. The morphological results in Fig. 5f-1 reveal the presence of α-MoO_3 NRs with smoother surfaces having lengths and diameters of about 10 μm and 200–300 nm, respectively. Ag NPs of ∼20 nm size were clearly observed in the Ag–MoO_3 sample (Fig. 5f-2), which was further confirmed in the TEM results in Fig. 5g-1 and g-2. The sensing response results in Fig. 5h unveiled the utility of Ag decoration on pure α-MoO_3 for enhancing the response toward TEA gas. The effect of temperature on the dynamic transient response curves (Fig. 5i) pointed out the incomplete recovery of response to its baseline due to the slower desorption of the gases. The cross-response results in Fig. 5j confirm the excellent selectivity of the sensor toward TEA gas among a variety of other

tested gases due to the interaction between the basic nature of TEA gas and the acidic MoO_3 surface. Besides, the electronic and chemical sensitization of the Ag NPs was also considered as a major factor for realizing the high response of Ag/α-MoO_3 NRs.

TEA is, as we know, a toxic, volatile, and explosive gas used in the fish processing industry.[4,21] It is, therefore, of utmost importance to design superiorly responsive gas sensors for the real-time detection of TEA at low OT. For example, Yang and coworkers[97] utilized a facile hydrothermal method for preparing α-MoO_3 NRs (Fig. 6a) for detecting TEA gas at low operating temperatures. α-MoO_3 NRs with clean and smooth surfaces and having length of 10 mm and diameter in the range of 200–300 nm are observed in Fig. 6b1–b3. The sensing results for TEA gas in Fig. 6c reveals that MoO_3 with NRs-type morphology possesses a higher response than the particle-based MoO_3 at the same OT. The histograms revealing the response-recovery time in Fig. 6d concluded that a high concentration of TEA causes the T_{res} to be less than 10 s with longer recovery times and *vice versa*. The cross-response results of the sensor for determining its discrimination ability in Fig. 6e revealed that the sensor distinguishably detects TEA gas among other tested gases under identical testing conditions. It was concluded that the high TEA response was not only a result of the attractive forces between the acidic and basic nature of MoO_3 surfaces and TEA molecules, respectively, but was also due to the highly active lattice oxygen and fast adsorption/desorption kinetics from the sensor surface.

As discussed earlier, heterostructure formation plays a key role in the interface to enhance the sensing performance.[21,135,136] Therefore, designing 1D-MoO_3 heterostructures with appropriate counterparts is of great importance in order to achieve excellent TEA sensing performance. Thus, it was further revealed by Bai *et al.*[108] that α-MoO_3 can dissociate the C–N bond present in TEA at the desired temperature. They synthesized the n–n heterojunction of α-MoO_3/$BiVO_4$ *via* the metal–organic decomposition method (Fig. 6f) and showed improved sensitivity toward TEA gas. The SEM and TEM results in Fig. 6g-1 and g-2 clearly show the development of the $BiVO_4$/MoO_3 composite as nanorods and also the growth of $BiVO_4$ nanoparticles on MoO_3 nanorods. The response curves in Fig. 6h showed an IMD trend for all the materials; however, the response of the $BiVO_4$/MoO_3 composite was much better than that of others. However, the longer T_{rec} for the $BiVO_4$/MoO_3 composite was due to the strong binding of the TEA molecules on the surface of α-MoO_3, which ultimately resulted in a poor desorption rate (Fig. 6i). In the end, the excellent selectivity results in Fig. 6j pointed to the fact that TEA, due to its lower C–N bond energy, gets oxidized very easily. It was finally concluded that the n–n heterostructured MoO_3/$BiVO_4$ composite was primarily responsible for the increased sensor response.

MoO_3 nanofibers (NFbs)

Recently, wet chemical approaches and electrospinning methods have increasingly become popular for the preparation of SMOx NFbs as they allow the creation of nanostructures with multiple configurations and morphological features. In line with this, Guo *et al.*[76] prepared SnO_2-doped MoO_3 NFbs (diameter ∼100 nm) by
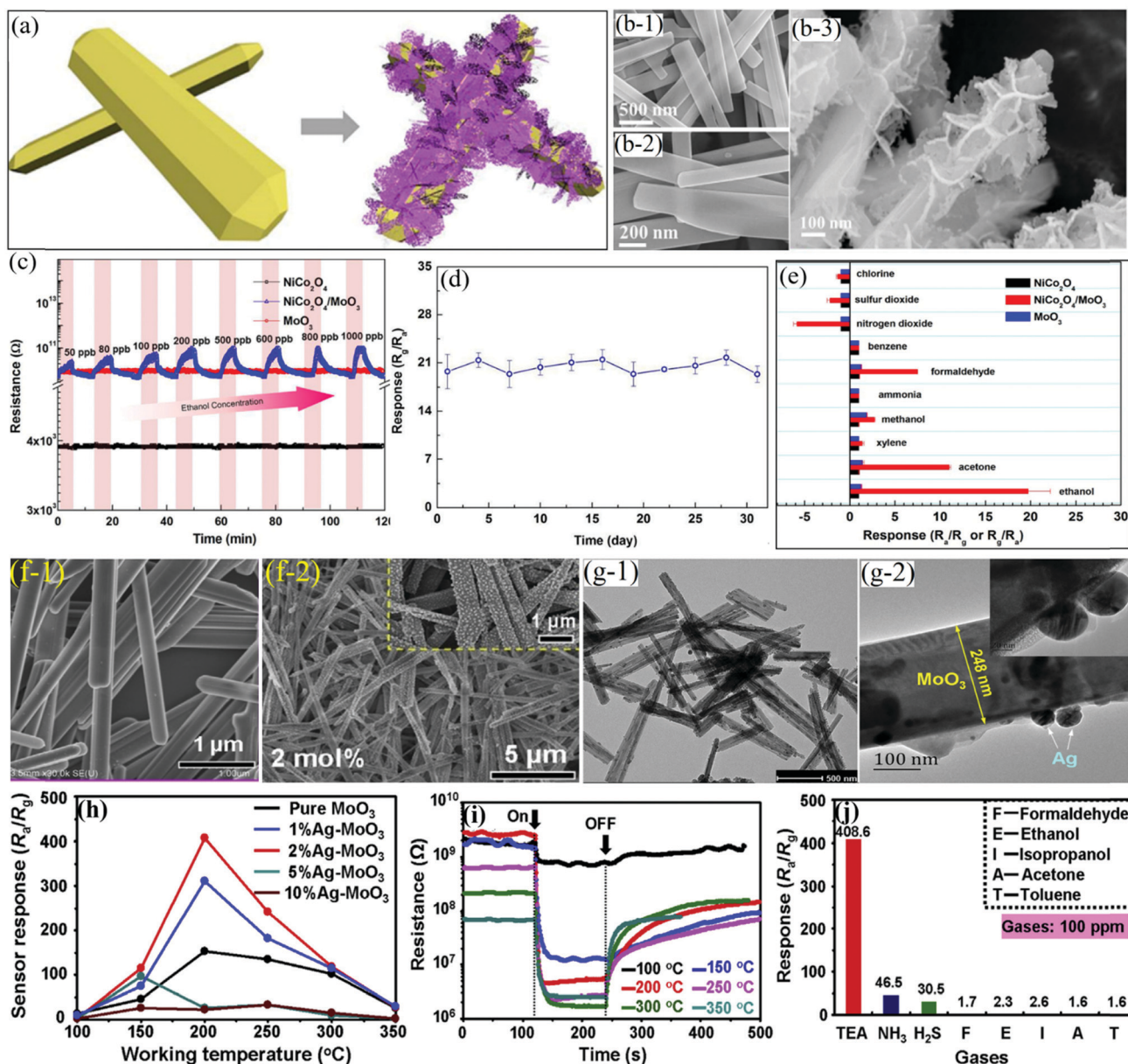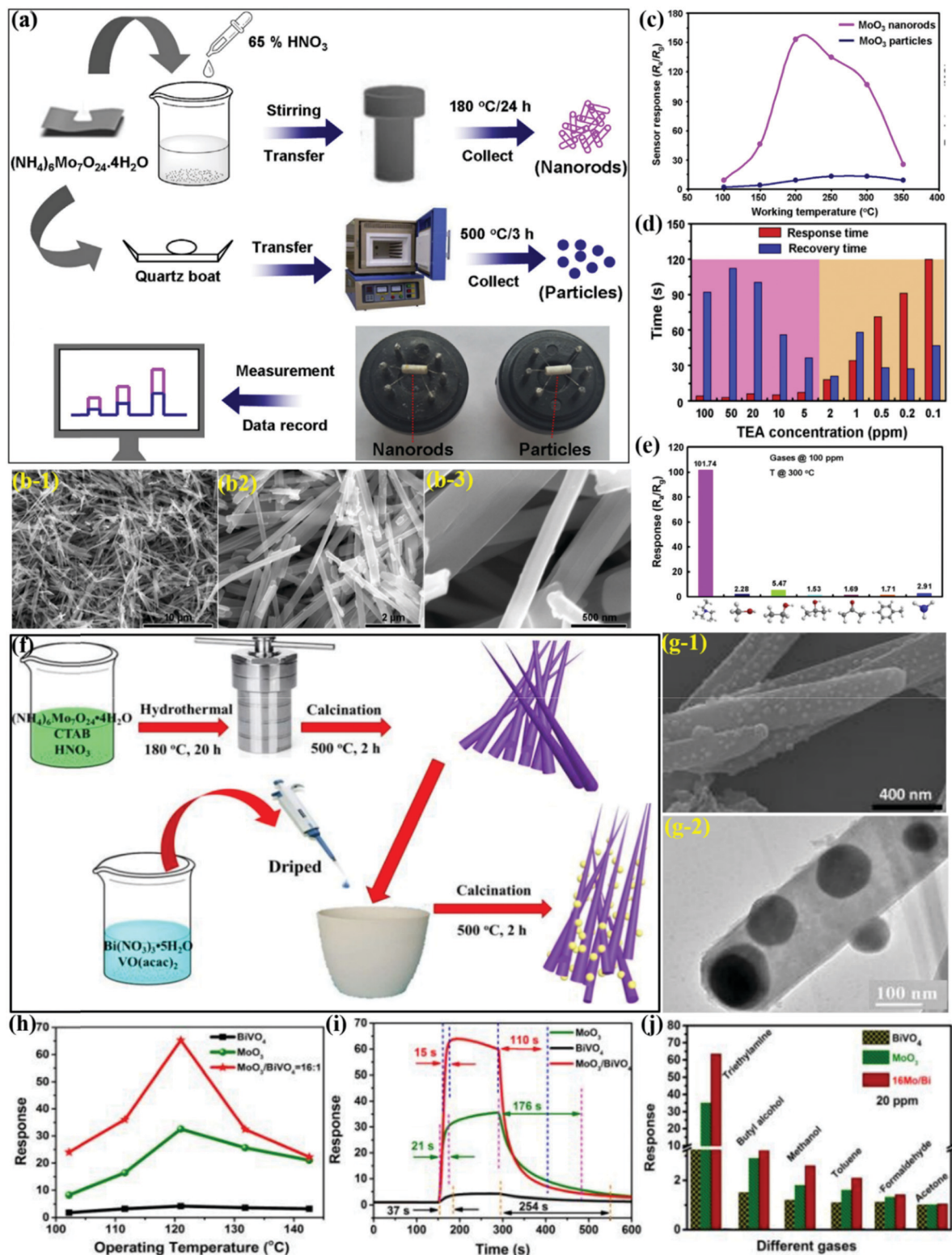
Fig. 5   (a) Schematic illustration of the synthesis of the NiCo$_2$O$_4$/α-MoO$_3$ nanocomposite; (b-1 and b-2) SEM image of pristine α-MoO$_3$; (b-3) magnified SEM image of the NiCo$_2$O$_4$/α-MoO$_3$ composites; (c) dynamic response transients to different concentrations of ethanol; (d) long-term stability of the NiCo$_2$O$_4$/α-MoO$_3$ nanocomposites toward 1 ppm ethanol at 350 °C; (e) selectivity toward 1 ppm interfering gases at 350 °C. Reproduced with permission from ref. 74, copyright 2019 Elsevier. FESEM images of the pure α-MoO$_3$ NRs (f-1) and AgNPs-decorated α-MoO$_3$ nanorods (f-2); (g) TEM images of 2%Ag–MoO$_3$; (h) sensing response toward 100 ppm of TEA at varied OT; (i) sensing transients of the 2%Ag–MoO$_3$ sensor toward 100 ppm of TEA; (j) cross-response of 2%Ag–MoO$_3$ at 200 °C. Reproduced with permission from ref. 75, copyright 2019 Elsevier.

using a wet-chemical method for the detection of carbon monoxide (CO) gas by screen printing the NFbs on alumina substrates (Fig. 7a). The response transients in Fig. 7b reveals the good reversible behavior of SnO$_2$/MoO$_3$ under alternative purging of CO and N$_2$ gases. The concentration-based sensing results in Fig. 7c displayed increasing response with the increment in the CO concentration. Besides, SnO$_2$/MoO$_3$ with NFbs morphology exhibited ~2-folds response to 300 ppm CO than pristine α-MoO$_3$ NBs. The selectivity histograms in Fig. 7d revealed that the nanocomposite sensor showed a better response to CO gas

owing to its fine nanofiber diameter and high S/V ratio. The inset SEM image shows that the SnO$_2$/MoO$_3$ nanocomposite exhibits diversely oriented fibers with the diameter and length in the range of 20–100 nm and 2–8 μm, respectively. It was later concluded that SnO$_2$ doping assisted in enhancing the sensing performances at low OTs, while the unique NFbs morphology of the SnO$_2$/MoO$_3$ nanocomposite and the acidic nature of the doped NFbs improved the sensitivity of the SnO$_2$-doped MoO$_3$ NFbs.

In another work, Mondal et al.[114] tailored highly crystalline and ultra-long MoO$_3$ NFbs by applying the temperature pulsing

Fig. 6   (a) Schematic illustration for the preparation of two MoO₃ products and sensing measurement of the actual sensors; (b) FESEM images of the MoO₃ NRs; (c) sensor responses to 100 ppm TEA vapor as a function of OT from 100 to 350 °C; (d) response and recovery times of the sensor at various concentrations of TEA gas; (e) sensor responses of the MoO₃ NRs to various gases with an identical concentration (100 ppm) at 300 °C. Reproduced with permission from ref. 97, copyright 2019 Elsevier. (f) Schematic diagram of the α-MoO₃/BiVO₄ composite synthetic process; (g) SEM and TEM image of the 16Mo/Bi composite; (h) responses at different OT to 20 ppm TEA; (i) response-recovery time to 20 ppm TEA; (j) response to 20 ppm of different gases at 125 °C. Reproduced from ref. 108, copyright 2020 with permission from the Centre National de la Recherche Scientifique (CNRS) and The Royal Society of Chemistry.
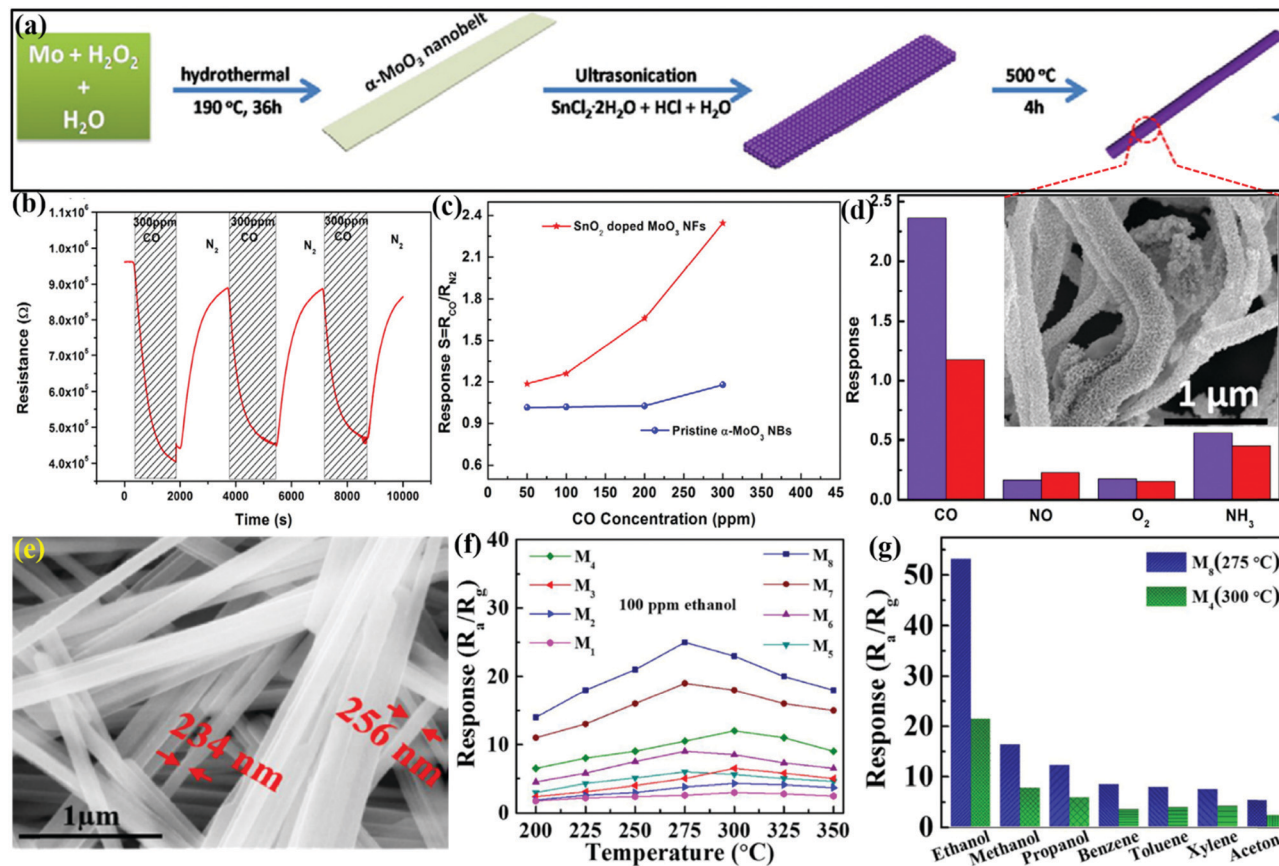
Fig. 7 (a) Schematic illustration of the growth mechanism of SnO$_2$-doped MoO$_3$ NFbs; (b) response–recovery curves of SnO$_2$-doped MoO$_3$ NFbs at 300 °C; (c) responses as a function of the CO concentration at 300 °C; (d) selectivity of pristine α-MoO$_3$ NBs (red) and SnO$_2$/MoO$_3$ NFbs (blue) toward various gases of 300 ppm at 300 °C, (inset) high-magnification SEM micrographs of SnO$_2$/MoO$_3$ NFbs. Reproduced with permission from ref. 76, copyright 2017 Elsevier. (e) SEM image of M4 grown at a constant temperature; (f) response of M1–M8 devices in exposure to 100 ppm ethanol at different OTs; (g) selectivity study toward 200 ppm of different VOCs. Reproduced with permission from ref. 114, copyright 2019 Elsevier.

method during HT growth. The SEM image in Fig. 7e demonstrates the presence of highly crystalline ultra-long nanofibers having several tens of micrometer of length and width in the range of 200–300 nm. The sensing results in Fig. 7f confirmed that MoO$_3$ with NFbs morphology (M5–M8) possesses better response at lower operating temperature than MoO$_3$ with the NBs structure (M1–M4) toward ethanol gas. Owing to the high surface area and more surface defects in MoO$_3$ NFbs, a high selectivity (Fig. 7g) to ethanol gas was observed among the other tested VOCs. At last, it was concluded that the large surface area and presence of surface defects were the prime reasons for the improved sensing performance of the MoO$_3$ NFs.

MoO$_3$ nanowires (NWs)

Metal oxide nanostructures as nanowires offer a great alternative for low-concentration sensing performance and their conventional processing enables integration with electronic devices for large-scale production. Luo *et al.*[82] utilized the HT method to prepare ultra-long α-MoO$_3$ NWs-based flexible nanowire paper (size ~200 mm × 300 mm) on a hydrophobic substrate. The NWs (Fig. 8a) demonstrated high crystallinity, good dispersion, long length (~1 mm), uniform diameter (~300 nm), and good

sensitivity toward H$_2$ gas. The results in Fig. 8b reveal the increasing response of the sensor (prototype of the H$_2$ sensor in the inset) with temperature in the range of 230–260 °C. The response/recovery transient curve in Fig. 8c accounts for fast T_{res} and T_{rec} and matches well with commercial grade sensors for the detection of H$_2$ leakage. Besides, the α-MoO$_3$ NWs paper sensor was found to have excellent repeatability (Fig. 8d) wherein the sensitivity, T_{res}, and T_{rec} are nearly unchanged even after seven repeated cycles. The sensor perfectly detected lower concentration of H$_2$ gas (below 1.5%); however, T_{res} and T_{rec} were increased at these lower concentrations (Fig. 8e). The high H$_2$ sensing response was attributed to the high specific surface and porous structures of the NW paper, which eases the absorption of O$_2$ molecules on the sensor surface.

MoO$_3$ microrods (MRds)

Similar to nanorods, the morphology of microrods (MRds) provides more surface-to-volume ratio to achieve rapid adsorption–desorption results with high sensitivity at low concentrations. Liu *et al.*[98] utilized a facile hydrothermal route to prepare hexagonal MoO$_3$ from peroxomolybdate solution in the presence of NH$_4$Cl. The SEM image in Fig. 8f confirmed a rod-like morphology for
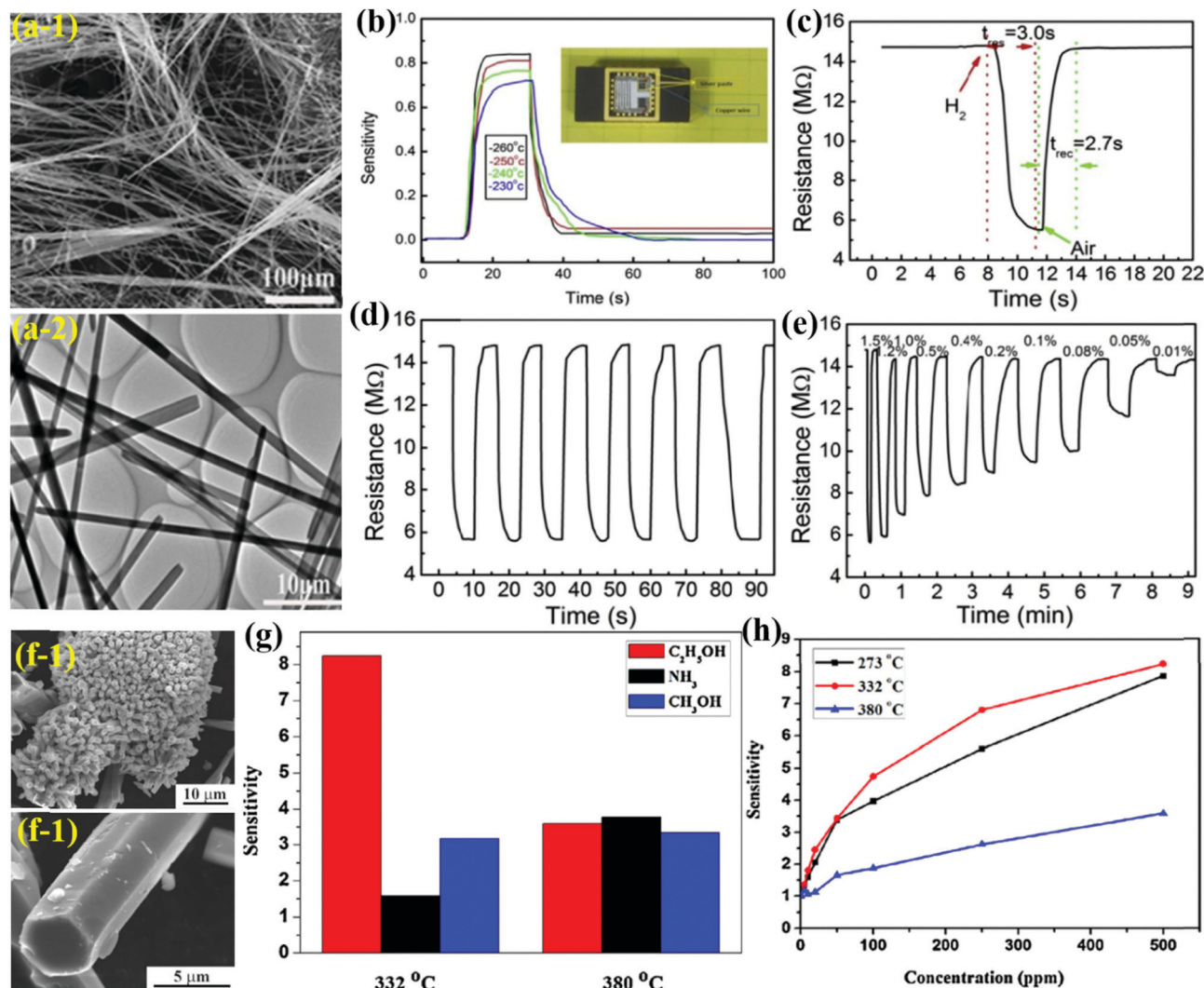
Fig. 8 (a) SEM and TEM images of the as-synthesized α-MoO₃ NWs; (b) the sensitivities of different sensors to 1.5% H₂; (c) response–recovery of the sensor to 1.5% H₂. (d) Repeatability toward 1.5% H₂; (e) dynamic response resistances of the flexible NWs paper for different H₂ concentrations (100 ppm – 1.5%). Reproduced with permission from ref. 82, copyright 2017 Elsevier. (f) Typical SEM image of h-MoO₃ MRds; (g) the selectivity of the h-MoO₃ MRds gas sensor to 500 ppm gases at the OT of 332 °C and 380 °C; (h) sensitivity of the sensors based on h-MoO₃ MRds to the exposure of different concentrations of ethanol at different OTs. Reproduced with permission from ref. 98, copyright 2015 Elsevier.

h-MoO₃ MRds with the length and diameter in the range of 12–25 μm and 1.0–3.5 μm, respectively. The selectivity of the h-MoO₃ MRds in Fig. 8g demonstrated excellent response to ethanol gas among a variety of other tested gases. The sensing results in Fig. 8h divulge that the h-MoO₃ MRds sensor possesses a detection limit of 5 ppm for ethanol and increases with the concentration of ethanol gas.

Two-dimensional (2-D) MoO₃ nanostructures for gas sensors

2-D materials have become increasingly popular due to their sheet-like structures, nanoscale thickness, and high S/V ratio.[4,14,20,134,137–139] As a 2-D carbon nanosheet, graphene, since its discovery, has exhibited important physico-chemical properties, which make it a hotpot material in many techno-logically important applications, including solar photovoltaics, energy materials, and medicine, and has ignited a quest in

discovering other materials that are analogous to graphene in terms of their structure and properties.[5,13,14,20,140,141] The research efforts have progressed with a great pace and a variety of inorganic graphene analogues having layered structures have been developed, which include oxides (TiO₂, SnO₂, WO₃, MoO₃, etc.), chalcogenides (MoSe₂, WS₂, WSe₂, etc.), and a few perovskite-like crystals with sensing applications.[33,142,143] 2-D materials are strong adsorbents of organic molecules, and at high temperatures, they tend to partially lose oxygen to become oxygen-deficient; thus, they are considered as the most suitable candidates in VOCs sensing.[144] Among the various 2-D nanostructures of MoO₃, nanosheet,[64,80,81,145] nanoflake,[146–148] nanoplate,[79,149,150] nanolamella,[151] nanopaper,[152] thin film,[153–156] microsheet[157] and microplanks[158] morphologies of MoO₃ have recently received great research interest in gas sensing applications as they can be used in designing nanodevices with desired crystal orientation due to their

Table 2 A detailed overview of the gas sensing performance using 2-D MoO$_3$-based gas sensors

Class	Material	Synthesis route/morphology	Gas	Conc. (ppm)	Operating temp. (°C)	Response	Resp./Reco. time (s/s)	Ref.
Nanosheet	MoO$_3$	Grinding + sonication	Alcohol	100	300	33	21/10	80
	MoO$_3$	Hydrothermal + calcination	Xylene	10	400	9.1	7.1/6.8	81
	MoO$_3$	Solvothermal + annealing	TMA	50	133	51.47	12/200	64
	Au/MoO$_3$	Hydrothermal + calcination + chemical reduction	Ethanol	200	280	169	22/5	145
Nanoflake	MoO$_3$/rGO	Hydrothermal + calcination	Ethanol	100	310	53	6/54	146
	MoO$_3$/SnO$_2$	Chemical synthesis	H$_2$S	10	115	43.5	22/10	147
	Au/MoO$_3$	Thermal evaporation + sputtering	H$_2$S	15	400	260	60/480	148
Nanoplate	MoO$_3$	Chemical synthesis	Ethanol	800	300	58	10^a/40^a	149
	MoO$_3$	Polymeric solution method	NO$_2$	100	250	47.9	N.G.	150
Nano lamella	Ni/MoO$_3$	Solvothermal	Formaldehyde	100	255	41	4/12	151
Thin film	MoO$_3$/V$_2$O$_5$	Chemical spray pyrolysis	NO$_2$	100	200	80(%)	118/1182	154
	MoO$_3$	Hydrothermal	Ethanol	100	260	23(%)	111/66	155
Microsheet	MoO$_3$	Hydrothermal + thermal oxidation	TEA	100	275	27.1	3/50	157
Micro plank	MoO$_3$	Chemical synthesis	CO	100	150	74.87	80/110	158

^{a} Not given.

anisotropic structures. An overview of gas sensors based on 2-D MoO$_3$ nanostructures is given in Table 2.

MoO$_3$ nanosheets (NSs)

2-D layered MoO$_3$ with a sheet-like structure has emerged as a model oxide material due to its excellent sensing properties toward a range of VOCs. Liu et al.[80] exfoliated bulk α-MoO$_3$ into single and few-layer NSs using grinding and sonication methods (Fig. 9a-1) and they observed an enhanced sensing feature for 2D-MoO$_3$ NSs as compared to its bulk powder counterpart. The sensor structure and the equivalent circuit model for sensor testing are demonstrated in Fig. 9a-2. The dimensions of the MoO$_3$ NSs in the range of 10–100 nm were deduced from the TEM images (Fig. 9b-1), whereas the HRTEM image in Fig. 9b-2 shows the multi-layer edges near the periphery of these NSs, unveiling their 2-D structure. The operating temperature response (Fig. 9c) of bulk MoO$_3$ and MoO$_3$ NSs obtained from different sonication solvents toward 100 ppm alcohol vapor reveal the higher response of MoO$_3$ with NSs morphology. Similar results were also observed in Fig. 9d, wherein the MoO$_3$ NSs exhibited faster response and recovery speed than bulk MoO$_3$. The histogram representing the cross-sensitivity of the MoO$_3$ NSs in Fig. 9e clearly shows that the sensor possesses better response to alcohol among other VOCs. This increased sensing performance of the MoO$_3$ NSs is attributed to its layered structure, offering enhanced surface area and more reactive sites. Contrary to using the exfoliation strategy from single-crystal MoO$_3$, Wang and coworkers[81] used a facile hydrothermal technique to prepare MoS$_2$ NSs and calcine them at different temperatures to obtain MoO$_3$ NSs with varied thickness. The SEM micrograph in Fig. 9f reveals the formation of NSs with uniform and smooth surfaces. The sensing results in Fig. 9g present that the MoO$_3$ NSs detect xylene gas at higher OT than the MoS$_2$ NSs, while the MoO$_3$ calcined at 400 °C (MoO$_3$ NSs-4) shows maximum response among the various MoO$_3$ NSs structures calcined at different OTs. The response/recovery performance of MoO$_3$ NSs-4 studied in Fig. 9h toward 10 ppm xylene showed quicker T_{res} and T_{rec} for the sensor. Further, the cross-sensitivity results of the sensor in

Fig. 9i demonstrated its excellent selectivity toward xylene gas among a variety of other interfering gases. It was finally concluded that the excellent sensitivity was mainly due to the larger SSA, causing increased adsorption of oxygen and the intrinsic porous structure, which results in abundant surface defects.

Another poisonous and colorless VOC, i.e., TMA, has drawn significant attention because initially, the smell seems pungent but it can rapidly paralyze the olfactory system and cause unawareness and headache. Shen and coworkers[64] detected TMA by developing porous α-MoO$_3$ ultrathin NSs using a one-step solvothermal (ST) route, followed by calcination. The main process of the synthetic procedure and the NSs (size between 500 and 800 nm) obtained at different calcination temperatures are presented in Fig. 10a. The OT-based response of α-MoO$_3$ NSs to 50 ppm TMA in Fig. 10b depicts an IMD trend for all the materials, yet the NSs obtained at 400 °C calcination temperature shows the highest response among others. The cross-sensitivity results (Fig. 10c) of α-MoO$_3$-400 to different gases revealed that the response to TMA gas was way higher than to the other test gases. In addition, the sensor displayed minute fluctuation to TMA gas (Fig. 10d) over the course of 3 months, indicating its great stability and reproducibility. This high response was accredited to the porous and ultrathin configuration of α-MoO$_3$-400, which provides numerous active sites for the adsorption of TMA molecules faster on the sensor surface. The adsorption energies for TMA and O$_2$ on α-MoO$_3$ NSs were estimated to be −2.16 and −0.5 eV, respectively, by DFT calculations. The results in Scheme 4a1 and b1 display that the energetically favorable adsorption positions of TMA on α-MoO$_3$ and the α-MoO$_3$ containing O-vacancy (Ov-α-MoO$_3$) are Mo atom and O-vacancy, respectively. Due to the steric hindrance, TMA is primarily physically adsorbed on two oxygen atoms and forms a bridge-like structure (O-TMA-O) in TMA-Ov-α-MoO$_3$. The adsorption energies of TMA on α-MoO$_3$ and Ov-α-MoO$_3$ are −2.16 and −0.25 eV, respectively. The density of states (DOS) results in Scheme 4b1 and b2 exhibit that on introducing the oxygen vacancy, the Fermi level enters the conduction band, thus causing a lowering of the band gap of TMA-Ov-α-MoO$_3$ than that of TMA-α-MoO$_3$. Since the smaller
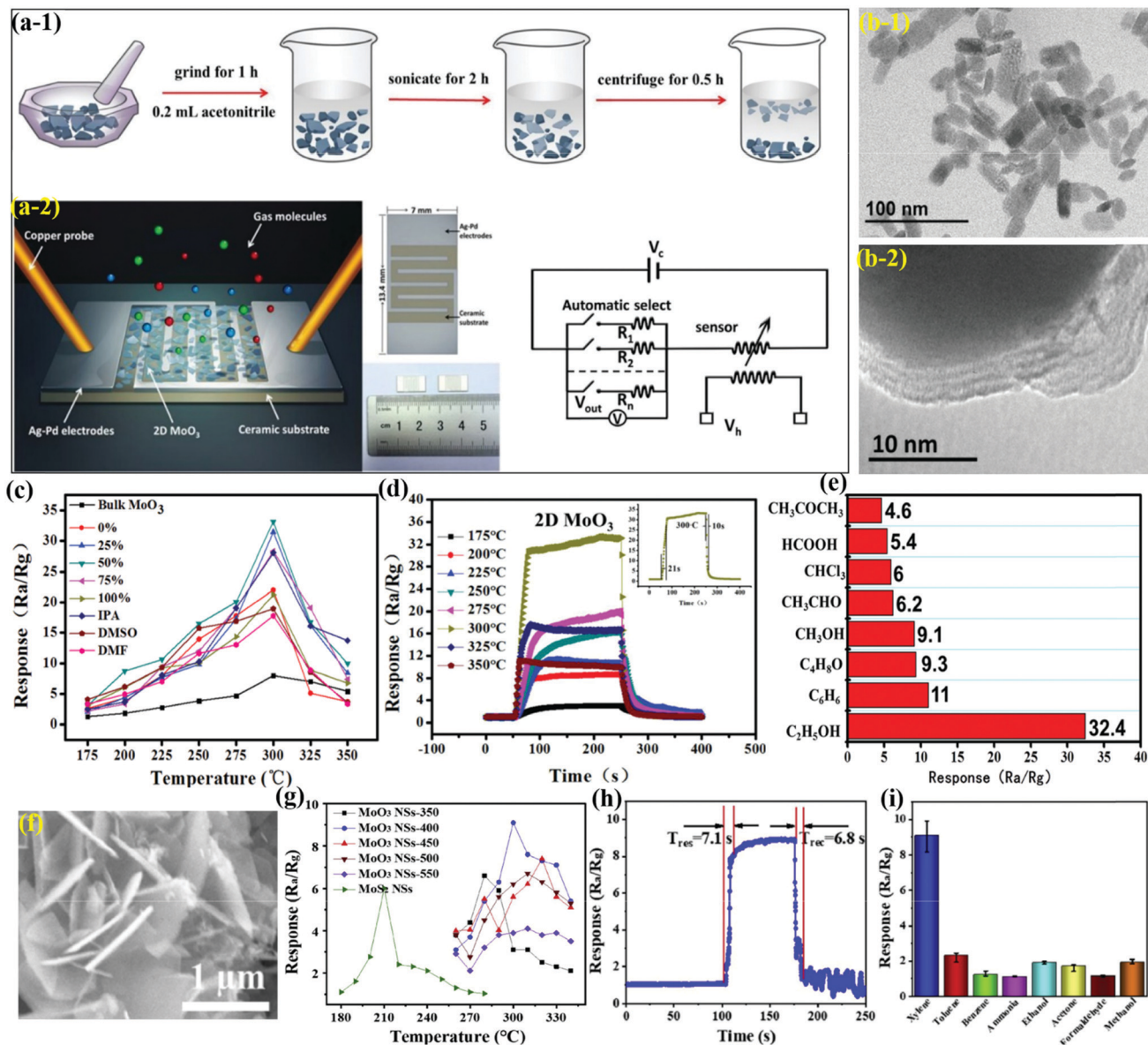
Fig. 9 (a-1) Three-step liquid exfoliation process; (a-2) schematic illustration of the fabricated sensor and the image of the operation principle; (b) TEM image showing the layered nature of the MoO_3 NSs; (c) the results of sensor response using bulk MoO_3 and MoO_3 NSs toward 100 ppm alcohol vapor at different OTs; (d) transient sensor response toward 100 ppm alcohol vapor at different temperatures, (inset) response and recovery curves at its optimum OT; (e) responses of sensors made of MoO_3 NSs toward 100 ppm VOCs. Reproduced with permission from ref. 80, copyright 2016 Royal Society of Chemistry. (f) SEM images of the MoO_3 NSs-400 samples; (g) sensor responses at varied OTs toward 10 ppm xylene; (h) response/recovery curve of the MoO_3 NSs sensor toward 10 ppm xylene at 300 °C; (i) responses of the MoO_3 NSs sensor to 10 ppm of different gases at 300 °C. Reproduced with permission from ref. 81, copyright 2020 Elsevier.

band gap is more favorable for electron transfer, the TMA states appear in the conduction band near the Fermi level, indicating that the interaction between TMA and Ov-α-MoO_3 is enhanced.

Surface modification with noble metals is a known practice in the sensing field. Essentially, noble metal NPs can facilitate the adsorption of oxygen molecules and accelerate the transfer of electrons to metal oxide surfaces.[34] For instance, the Yan et al.[145] used a chemical reduction method for depositing Au NPs onto the MoO_3 surface to prepare Au-loaded MoO_3 NSs. The TEM image in Fig. 10e displays the average distribution of Au NPs of size 10–15 nm on the surface of MoO_3 NSs. The temperature-dependent response

curves for ethanol in Fig. 10f exhibit an 'increase-maximum-decrease' tendency, whereas the Au@MoO_3 NSs possess ∼ 12 times better response than that of pristine MoO_3. The same behavior is illustrated in Fig. 10g, wherein the Au@MoO_3 NSs show the highest response toward ethanol gas, among others. This high sensing response is accredited to the presence of highly catalytic Au NPs, which assist in enhancing gas diffusion on the sensor surface.

MoO_3 nanoflakes (NFks)

Compared to 1D architectures, 2D nanoflakes can provide more efficient electron transport and better mechanical stability due
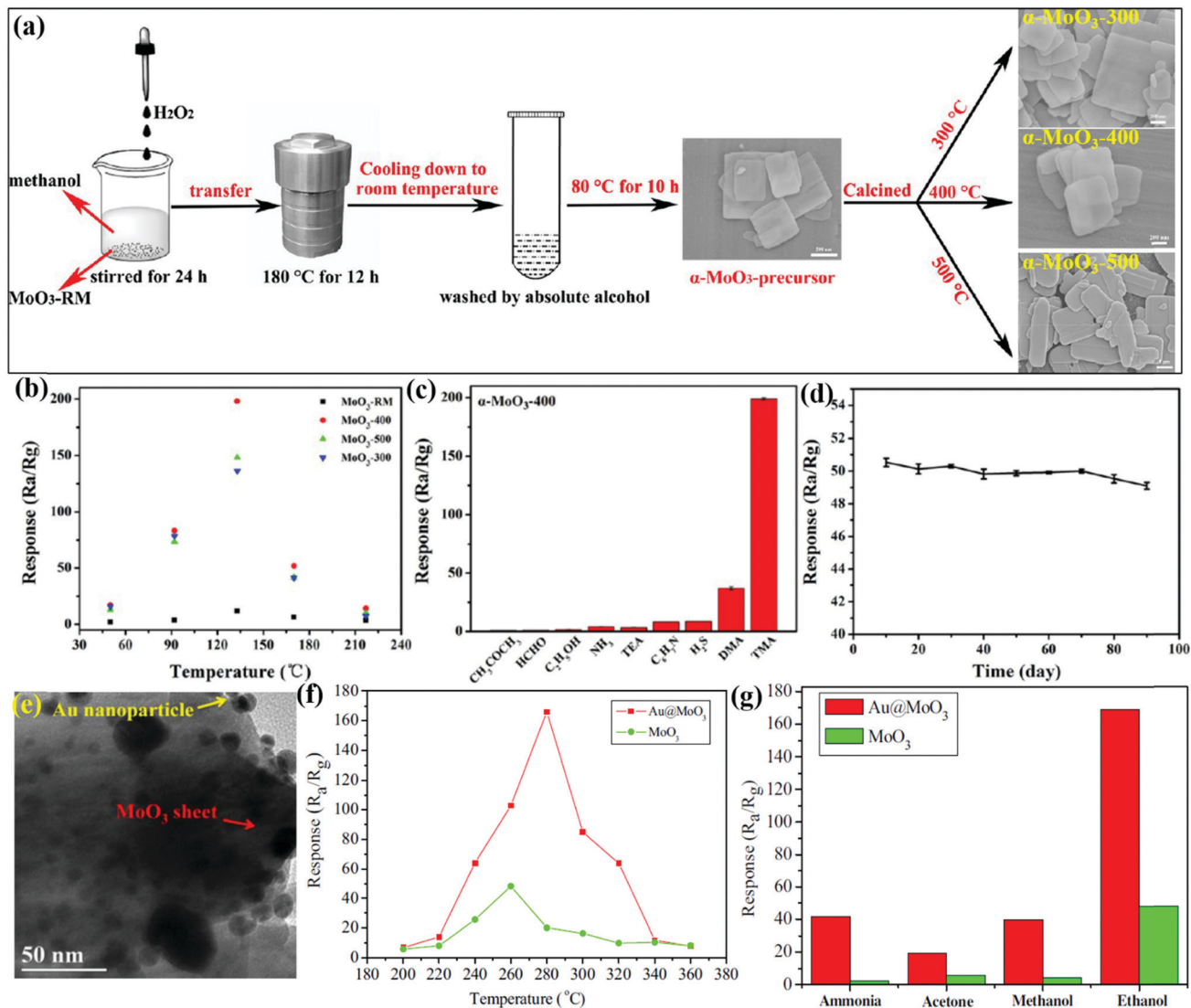
Fig. 10 (a) Schematic diagram for the preparation of α-MoO₃ along with the SEM images of different materials; (b) responses *versus* the OT to 50 ppm TMA gas; (c) responses *versus* 50 ppm of various gases at 133 °C; (d) responses of the α-MoO₃-400 sensor to 10 ppm TMA at 133 °C for 90 days. Reproduced with permission from ref. 64, copyright 2019 American Chemical Society. (e) TEM images of Au@MoO₃ nanocomposite samples; (f) response to 200 ppm ethanol at different OTs; (g) gas responses to 200 ppm of the test gases at 280 °C. Reproduced with permission from ref. 145, copyright 2016 Elsevier.

to fewer grain boundaries. In addition, nano-flakes allow surface reactivity and selectivity to be tuned through crystal facet engineering. Tang *et al.*[146] developed MoO₃ NFks-coupled reduced graphene oxide (MoO₃-rGO) composites for detecting ethanol gas. The preparation process in Fig. 11a reveals that ultrathin MoS₂–GO were prepared first *via* the HT method, which upon calcination under optimum temperature leads to the formation of MoO₃-rGO NFks. The SEM micrograph of MoO₃-rGO in Fig. 11b-1 presents NFks kind of morphology having a diameter in the range from nanometer to micrometer, while the TEM image in Fig. 11b-2 confirms the even distribution of NFks having a diameter 190 nm. These unique 2D NFks of MoO₃-rGO assist in high sensing response toward ethanol gas. The OT dependent response in Fig. 11c indicates the high sensitivity of the MoO₃-rGO sensor against pure MoO₃ due to the slightly large

SSA of MoO₃-rGO than that of MoO₃. Besides, the cross-sensitivity results in Fig. 11d present the excellent sensitivity and selectivity of the MoO₃-rGO sensor to ethanol gas, which is attributed to the high volume of Mo⁵⁺ in the nanocomposite as compared to pristine MoO₃. In addition, the presence of GO substrates in MoO₃-rGO offers large surface accessibility and fast carrier transport, which facilitates gas analyte adsorption/diffusion and transport across the sensor surface, while the defects or edge areas in GO also majorly contribute to the adsorption of the gas molecules.

Considering the potential of the heterostructured nanocomposites consisting of two or more types of metal oxides due to their individual synergetic effect in enhancing the sensing response,[31,159,160] Gao and coworkers[147] prepared porous MoO₃/SnO₂ NFks using graphene sheets (G) as sacrificial templates
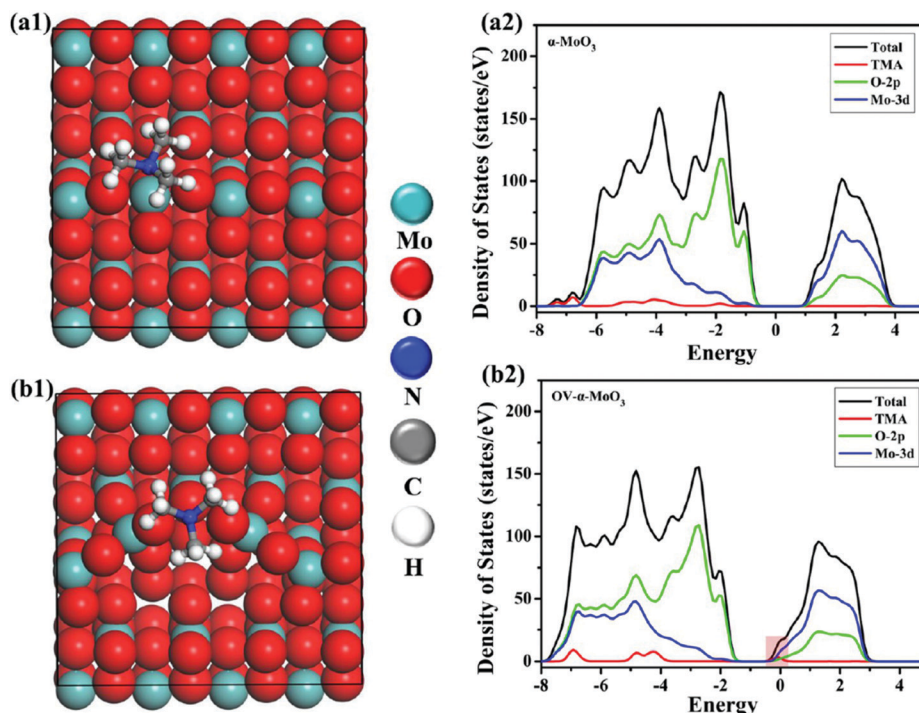
Scheme 4 Structures (top view) of TMA-α-MoO$_3$ (a1) and TMA-Ov-α-MoO$_3$ (b1). The density of states of TMA-MoO$_3$ (a2) and TMA-Ov-MoO$_3$ (b2). Reproduced with permission from ref. 64, copyright 2019 American Chemical Society.

(Fig. 11e) and revealed the excellent sensing performance toward H$_2$S, which is a poisonous, corrosive, and flammable gas. The SEM micrographs of MoO$_3$/SnO$_2$ NFks in Fig. 11f demonstrated the presence of an agglomerated structure with porous SnO$_2$ NFks (diameter ∼8–12 nm). The results in Fig. 11g present that the MoO$_3$/SnO$_2$ NFks demonstrate better sensing properties (∼5 times response) than that of pure SnO$_2$, that too at lower working temperature. The cross-sensitivity results in Fig. 11h further attests to the superior sensing response of the MoO$_3$/SnO$_2$ NFks to H$_2$S gas as compared to the pure SnO$_2$-based sensor. The superior sensing response of the MoO$_3$/SnO$_2$ NFs was credited to the presence of a large surface area and n–n heterojunctions, which favor faster gas diffusion, thus resulting in improved H$_2$S sensing performance. In another work, the group of Comini *et al.*[148] utilized an evaporation-condensation method to prepare Au-loaded MoO$_3$ NFks for the detection of H$_2$S gas. Owing to the smaller dimension and better separation, a large number of H$_2$S molecules became absorbed on the surface of Au–MoO$_3$ NFks, ultimately resulting in enhanced sensing performance. The TEM micrographs in the inset of Fig. 11i reveal the clear presence of homogenized Au NPs (diameter ∼10–12 nm) on the surface of the MoO$_3$ NFks. The OT dependent response of pure MoO$_3$ NFks (Fig. 11i-1) and Au–MoO$_3$ NFks (Fig. 11i-2) indicated the increased response of the MoO$_3$ NFks with Au functionalization. The results further revealed 10 times better response for the Au–MoO$_3$ sensor than pure MoO$_3$ NF, while the optimum OT was reduced from 450 °C to 400 °C. The dynamic response/recovery transients in Fig. 11j depict the excellent reversible response, which, when exposed to reducing gas, increased and restored the initial values on account of exposure to natural air. From the

results, it was concluded that the Au–MoO$_3$ NFks, owing to their enhanced surface area and formation of Schottky barriers at the interface between Au and MoO$_3$, promote gaseous oxygen dissociation, which ultimately resulted in enhanced sensor response toward H$_2$S gas.

MoO$_3$ nanoplates (NPts)

Nanoplates have been actively used as sensing elements in sensing devices and are mainly synthesized *via* wet chemical approaches such as hydrothermal or solvothermal due to their simple operation, low cost, and controlled morphology. Chen and coworkers[149] developed α-MoO$_3$ NPts using molybdate-based inorganic–organic hybrids and demonstrated their superior sensing performance toward ethanol gas. The TEM image in Fig. 12a displays several overlapping quadrilateral plates (average length ∼1–2 mm). The sensitivity of the α-MoO$_3$ NPts as a function of the concentrations in Fig. 12b presents the highest response of the sensor to ethanol vapors among other tested reagent vapors. The response of the α-MoO$_3$ NPts sensors to ethanol *versus* the OT in Fig. 12c shows that the OT causes no apparent influence on the response in the low concentration range, whereas, in the higher concentration region, the α-MoO$_3$ NPts show better sensitivity at lower temperatures.

In addition, UV light illumination is one of the alternative ways to improve the recovery speed. On illuminating the sensor with UV light, the adsorbed oxygen ions on the surface are removed, thus providing a clean surface with more fresh interaction sites that are readily available for interaction with the target gas. Using this method, Kalanur *et al.*[79] prepared an H$_2$ sensor by depositing Pd NPs on hydrothermally synthesized
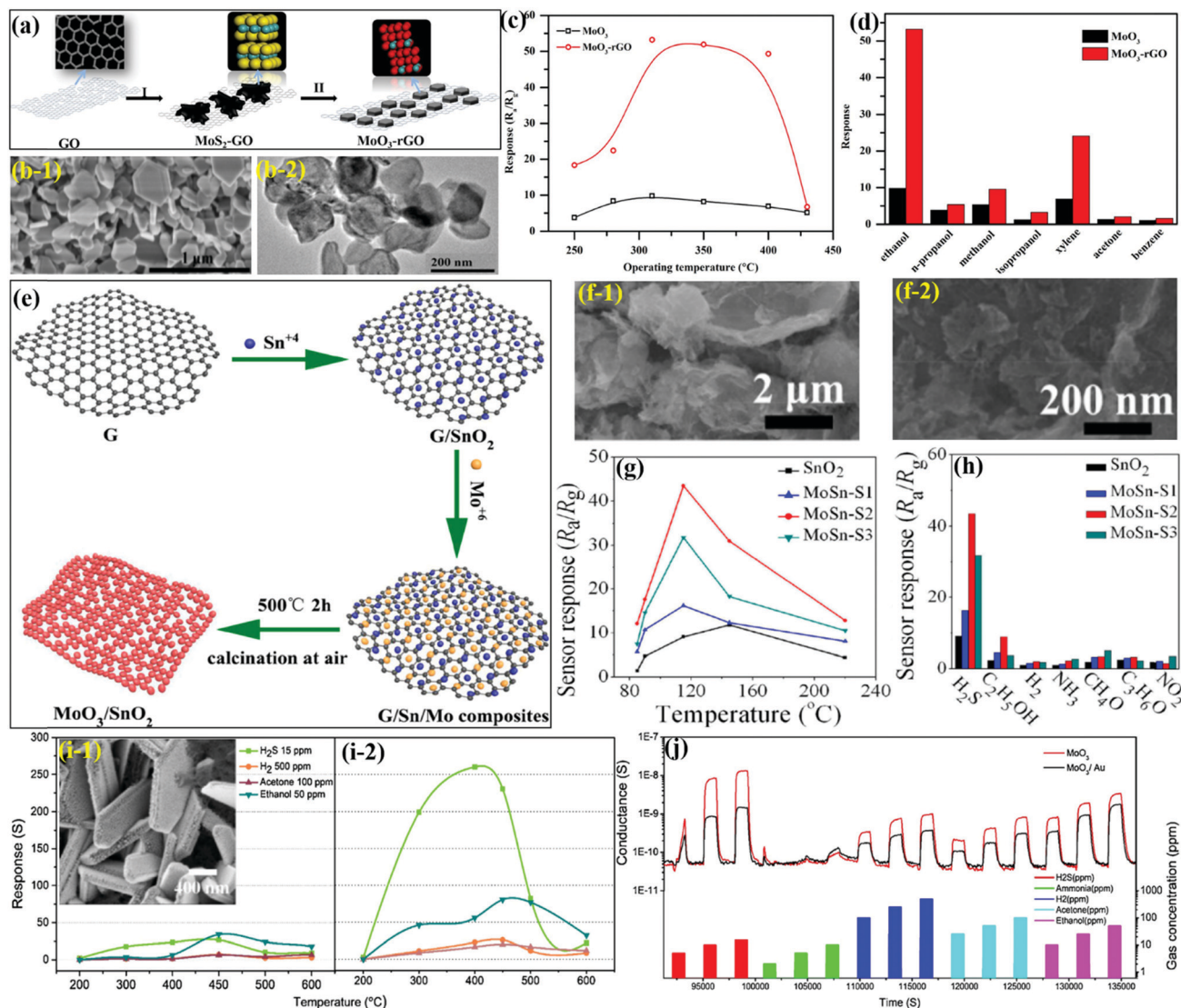
Fig. 11 (a) Schematic diagram of the preparation of MoO_3-rGO; (b) SEM and TEM images of MoO_3-rGO; (c) response to 100 ppm of ethanol under different OTs; (d) response of the sensors toward different VOCs. Reproduced with permission from ref. 146, copyright 2019 Elsevier. (e) Illustration for the preparation process of MoO_3/SnO_2 NFs; (f) SEM images of MoSn-S2; (g) sensor responses to 10 ppm H_2S concentration; (h) response to 10 ppm of various test gases. Reproduced with permission from ref. 147, copyright 2019 American Chemical Society. (i) Response toward various gases at different OTs. (Left) Pure MoO_3 NF and (Right) Au−MoO_3 NFks, (inset) SEM image of Au−MoO_3 NFks; (j) dynamic response of Au−MoO_3 toward H_2 (100, 250, 500 ppm), acetone (25, 50, 100 ppm), and ethanol (10, 25, 50 ppm) at 450 °C. RH = 40% at 20 °C, with an applied voltage equal to 1 V. Reproduced with permission from ref. 148, copyright 2018 Elsevier.

MoO_3 NPts. The SEM images in Fig. 12d-1 for pure MoO_3 NPts revealed their length, width, and thicknesses to be in the range of 1–4 μm, 100–150 nm, and 10–20 nm, respectively. Also, the NPts-type morphology of MoO_3 was found to remain unchanged after Pd deposition and UV exposure (Fig. 12d-2). The TEM image (Fig. 12e) further supported the SEM results wherein the Pd NPs (diameter ∼5–20 nm) were clearly deposited on the smooth surface of MoO_3. The RT I–V characteristics of the sensor in open air (Fig. 12f) displayed that the current level increased with H_2 concentration. The studied mechanism in Fig. 12g indicated the chemochromic effect as a result of the structural changes from H_2 gas. This indicated the co-occurrence of oxygen vacancies and water molecules in the MoO_3 crystal. Due to the

spillover effect, the Pd NPs dissociate the absorbed H_2 molecules into H_2 atoms, which are transferred onto MoO_3 NPts and assisted in generating oxygen vacancies.

Air quality issues caused by exhaust gases from rapid industrialization have become a serious problem worldwide in recent years.[161] In particular, nitrogen dioxide (NO_2), which causes photochemical smog and acid rain, is one of the toxic gases emitted during combustion in industries. The high risk of respiratory and lung diseases will increase when exposed to this gas. Therefore, a reliable NO_2 sensor for air quality monitoring is needed; in this regard, Felix and coworkers[150] utilized a facile polymeric solution method to prepare rectangular α-MoO_3 NPts and demonstrated good NO_2 sensing performance. The SEM
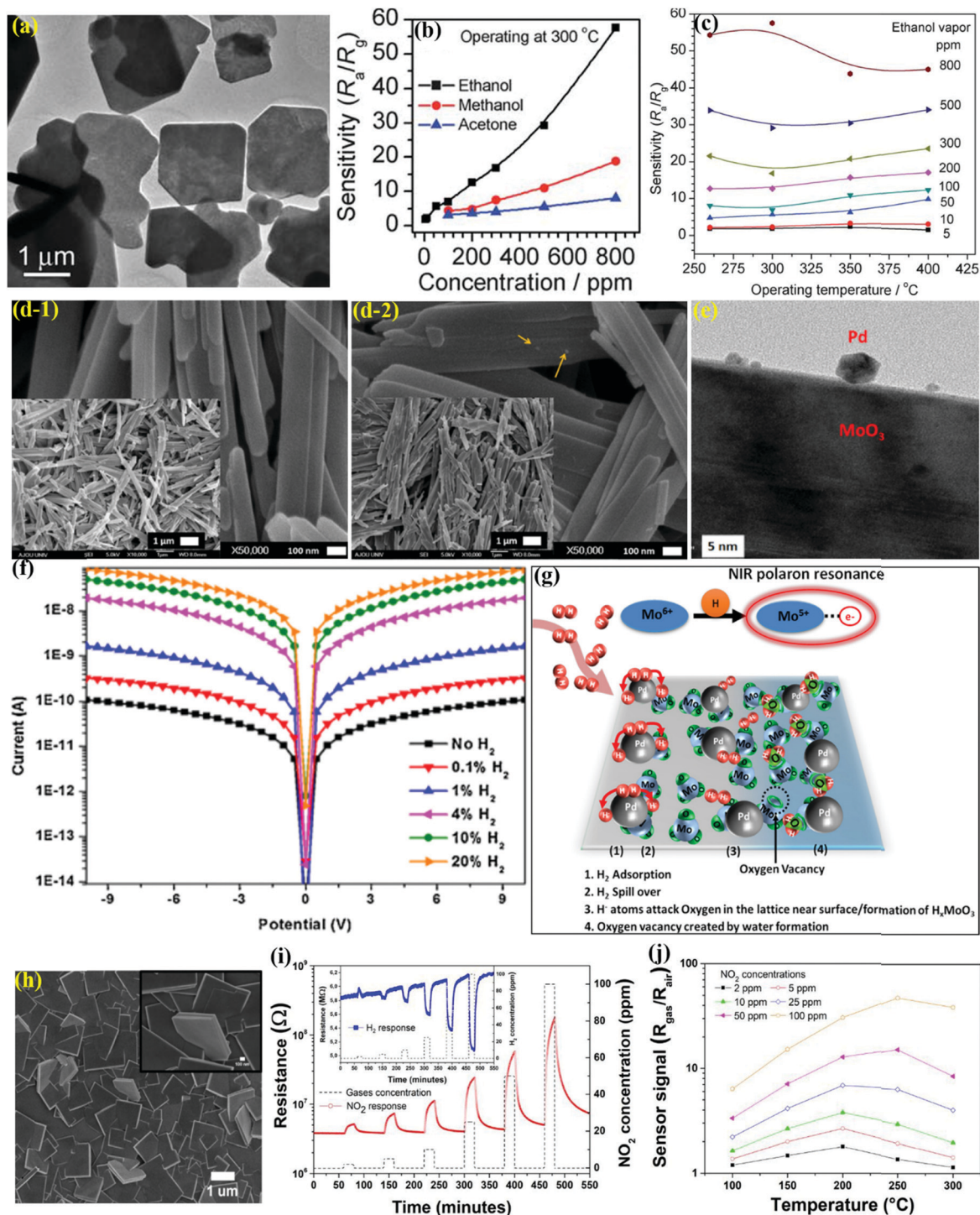
Fig. 12 (a) TEM image of α-MoO$_3$ NPts; (b) the sensitivities of the α-MoO$_3$ NPts sensors as a function of the concentrations of different reagent vapors; (c) the sensitivity changes of the α-MoO$_3$ NPts sensors at various OTs under ethanol vapor in the concentration range of 5–800 ppm. Reproduced with permission from ref. 149, copyright 2011 Royal Society of Chemistry. (d-1) SEM images of MoO$_3$; (d-2) SEM image of the MoO$_3$-Pd nanocomposite. The insets show the corresponding low-resolution images; (e) HRTEM image of the MoO$_3$–Pd nanocomposite; (f) current–voltage characteristics of the MoO$_3$–Pd nanocomposite in the presence of different concentrations of H$_2$ gas at RT; (g) proposed mechanism of the interaction of H$_2$ gas with the MoO$_3$–Pd nanocomposite. Reproduced with permission from ref. 79, copyright 2017 Elsevier. (h) SEM image of the as-grown MoO$_3$ nanostructures prepared on silicon substrates at 400 °C for 1 h with 3-layer depositions; (i) transient gas sensing response as a function of the NO$_2$ concentration at 250 °C for the layered α-MoO$_3$ nanoplates, (inset) transient H$_2$ sensing response as a function of the concentration at 250 °C; (j) sensor signal as a function of the OT at different NO$_2$ concentrations. Reproduced with permission from ref. 150, copyright 2020 Royal Society of Chemistry.

image in Fig. 12h illustrated well-faceted rectangular NPts morphology of the α-MoO$_3$ samples prepared at 400 °C for 1 h as a function of the number of layers deposition. The transient response curves in Fig. 12i reveal that the resistance for NO$_2$ increased, while an opposite behavior was observed for H$_2$ gas. Also, the sensor was able to exhibit a highly reversible response down to sub-ppm values for both gases. The response results as a function of the OT and NO$_2$ concentration in Fig. 12j revealed an increase-maximum-decrease kind of pattern for all the tested concentration ranges. The results indicate that the unique synthetic method assisted in the growth of 2-D MoO$_3$ NPts on crystalline substrates, thus eliminating the requirement of any transfer process and leading to the development of a high-performance gas sensor.

MoO$_3$ nanolamella (NLm)

Various VOCs are extremely volatile and harmful to people even at low concentrations, and formaldehyde (HCHO) is one of them, which has recently become a major indoor pollutant. Overexposure to this VOC can cause throat irritation, eye irritation, and even cytotoxic effects. Shen and coworkers[151] utilized an ST method to developed Ni-doped α-MoO$_3$ NLm and demonstrated a promising formaldehyde gas sensor. The SEM image in Fig. 13a indicates the lamellar-shaped morphology of the nanocomposite, whereas the OT dependent sensing results in Fig. 13b revealed that the response followed an IMD pattern. Besides, the optimized

Ni/α-MoO$_3$ NLm indicated a ∼4 fold response as compared to pristine MoO$_3$ under identical testing conditions, thus revealing the benefits of doping Ni NPs in MoO$_3$. The dynamic response characteristics of the sensors for increasing the formaldehyde concentration. Fig. 13c represents a fast response/recovery of the Ni/α-MoO$_3$ NLm at all concentration values (detection limit ∼3 ppm). The selectivity results in Fig. 13d further attest to the high response of Ni/α-MoO$_3$ NLm toward formaldehyde, among other tested gases. The improved formaldehyde sensing performance of Ni/α-MoO$_3$ NLm was the result of formation of the p–n junction and the increase in the concentration of oxygen vacancies.

MoO$_3$ nanopaper (NPr)

Working in the direction of 'one stone two birds', Lee and coworkers[152] designed a free-standing, flexible, semitransparent ultrathin MoO$_3$ NPr sensor (Fig. 13e) from MoO$_3$ NBs for the detection of TMA and H$_2$S gas. Due to the presence of Lewis-acid sites, MoO$_3$ exhibited high sensitivity toward both TMA and H$_2$S. The SEM images in Fig. 13f1 to f4 confirmed the formation of uniform MoO$_3$ NPr, which consists of highly interconnected MoO$_3$ NBs coated on the electrodes. MoO$_3$ NBs with a width of 200–400 nm and length of 100–200 μm could bridge two electrodes over the gap (100 μm). The OT-dependent MoO$_3$-NPr sensor in Fig. 13g depicted maximum responses to TMA and H$_2$S at 325 and 250 °C, respectively. The selectivity of the MoO$_3$-NPr sensor at 325 °C in Fig. 13h revealed a good selectivity
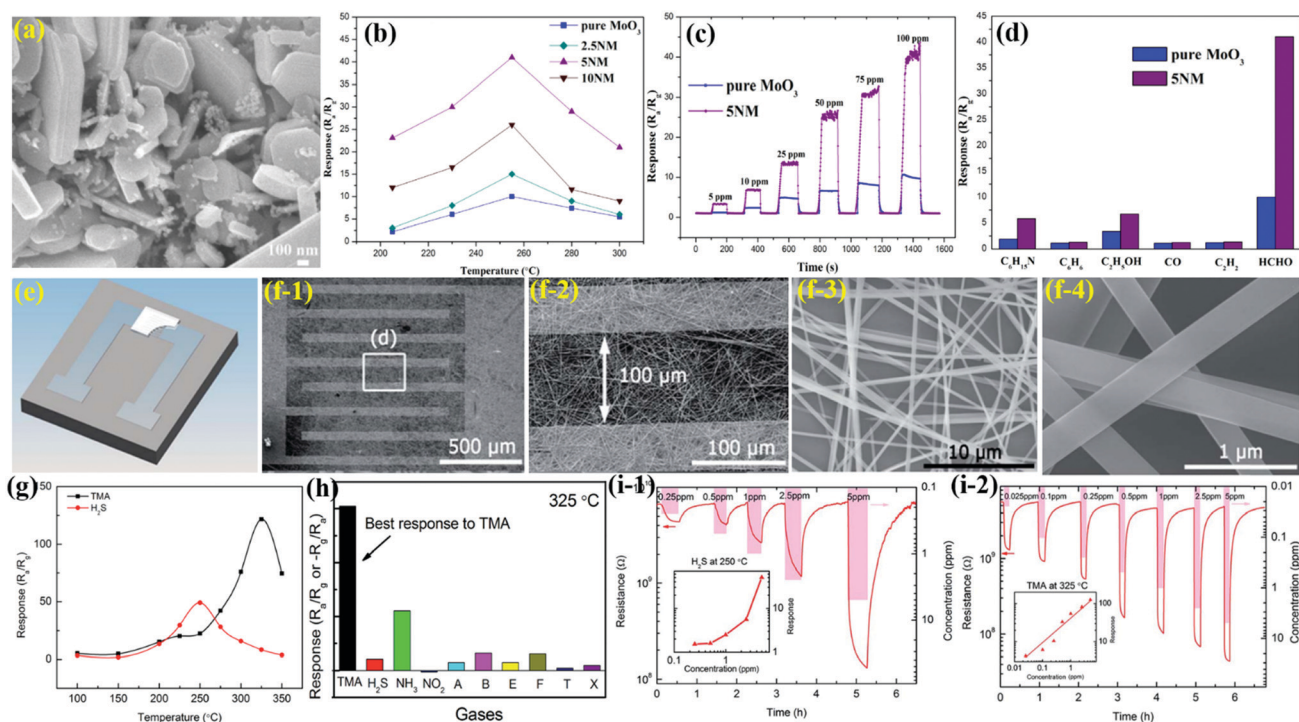
Fig. 13 (a) SEM images of 5 mol% Ni-doped α-MoO$_3$; (b) response vs. optimum OT of the sensors to formaldehyde gas at a concentration of 100 ppm; (c) gas-sensing transients to 5–100 ppm formaldehyde operated at optimal OT; (d) comparison of the response the sensor to 100 ppm of different test gases at 255 °C. Reproduced with permission from ref. 151, copyright 2017 Elsevier. (e) Schematic figure of the MoO$_3$-NPr gas sensor; (f) SEM images of the MoO$_3$-NPr gas sensor; (g) responses of the MoO$_3$-NPr sensor to 5 ppm TMA and H$_2$S with respect to the OT; (h) selectivity of the MoO$_3$-NPr sensor at 325 °C; (i) response–recovery curves of the MoO$_3$-nanopaper sensor to different H$_2$S concentrations at 250 °C and 325 °C, (insets) the response of the sensor to various gas concentrations. Reproduced with permission from ref. 152, copyright 2017 Royal Society of Chemistry.

toward TMA, whereas the dynamic sensing curves of the MoO$_3$-NPr sensor in Fig. 13i revealed that the sensor could detect both H$_2$S (25 ppb) and TMA (4.26 ppb) gases at a very low concentration, which is much better than the detection results of human nose. It was concluded that the high chemical affinity of MoO$_3$ to H$_2$S analytes was the reason for its sensitive, selective, and reversible detection at 250 °C, whereas the acid–base interaction between acidic MoO$_3$ and basic TMA was responsible for its detection at 325 °C.

MoO$_3$ thin films (TFm)

The thin-film (TFm) morphology is one of the extensively explored 2-D structures of oxide materials for gas sensing applications. For MoO$_3$, numerous techniques, including spray pyrolysis, sol–gel, sputtering, pulsed laser deposition, chemical vapor deposition, thermal evaporation, and electrochemical deposition, have been taken into practice for the deposition of MoO$_3$ films.[65,67,68,71] The research group of Pandeeswari et al.[153] have utilized the spray pyrolysis technique to develop α-MoO$_3$ film for the detection of TMA vapors in a mixed environment at low OT. The FESEM image in Fig. 14a clearly presents a film surface morphology for α-MoO$_3$ TFm consisting of rectangular crystallites with an average width of 62 nm and length of 450 nm. The response of the film for different TMA concentrations in Fig. 14b indicate an increase in the response up to 50 ppm, over which the response became saturated (curve a), which could be due to the limited number of oxygen-adsorption sites. With the increase in the TMA concentration, more electrons were freed-up, which decreased the electrical resistance (curve b). The transient response/recovery curves in Fig. 14c reveal an instantaneous change in the resistance, while for a given concentration of TMA, the T_{rec} was greater than T_{res}. The selectivity results of the α-MoO$_3$ TFm sensor in a mixed-vapor environment (Fig. 14d) revealed very little variation in the resistance to TMA gas, thus revealing a good selectivity toward TMA.

In order to further enhance the sensor response compared to the above-mentioned gas sensors, it is essential to adjust the morphology, modify the surface, or combine other oxide and 2-D materials. The group of Mane et al.[154] prepared MoO$_3$/V$_2$O$_5$ TFm using the chemical spray pyrolysis (CSP) deposition method (Fig. 14e) for the detection of NO$_2$ gas. The variation in response of MoO$_3$/V$_2$O$_5$ TFm toward NO$_2$ at different OT in Fig. 14f presents an IMD pattern, while the maximum response was observed at 200 °C. The dynamic response curves of MoO$_3$/V$_2$O$_5$ in Fig. 14g revealed that both T_{res} and T_{rec} decrease with an increase in the OT, whereas the larger T_{rec} at lower OT was ascribed to more prominently adsorbed O$_2^-$ species on the sensor surface. The gas response results in Fig. 14h show that the response of gases for MoO$_3$/V$_2$O$_5$ TFm varied in the pattern of CO < CO$_2$ = H$_2$S < NH$_3$ < SO$_2$ < NO$_2$. The higher gas response of 80% for NO$_2$ gas could be due to the unpaired e$^-$ in nitrogen, which forms the bond with the oxygen present on the surface and subsequently promotes chemisorption.

Flexible and wearable gas sensors using flexible substrates have been an active area of research to overcome the problem of the operating temperature. In addition, most of the sensors fabricated so far have been based on the deposition of sensing layers on mechanically rigid substrates such as alumina, glass, quartz, or silicon. In addition, the precise detection of humidity in the indoor climate has also emerged as a research hotpot in recent times;[136,140,162–164] thus, Ma and coworkers[156] prepared α-MoO$_3$ TFm by a simple solution method and prepared a transparent humidity sensor, which consisted of laser-etched fluorine-doped tin oxide (FTO) electrode, onto which the annealed α-MoO$_3$ thin film was coated (Fig. 14i). The SEM image in Fig. 14j revealed that the FTO substrate has an important influence on the film formation process as the morphologies of the film on the channels and FTO electrodes are not exactly the same. Fig. 14k represented the excellent transmittance of the prepared sensing device derived from the thin α-MoO$_3$ film and transparent FTO substrate, which are particularly helpful in achieving superior response to humidity under ambient conditions (Fig. 14l). The dynamic current–time curve in Fig. 14m revealed the superfast T_{res} and T_{rec} of the humidity sensor. In addition, the sensor possesses good anti-interference ability as its selectivity for moisture was much high than toward other test gases (Fig. 14n) under similar testing conditions.

MoO$_3$ microsheets (MSh)

The high degree of anisotropy and chemical functionality of the 2D microsheets have attracted researchers to develop reliable and robust gas sensors. Jiang et al.[157] developed MoO$_3$ MSh by thermally oxidizing the MoO$_2$ nanospheres, which were prepared by the HT method. The FESEM micrographs of MoO$_3$ MSh in Fig. 15a depict the formation of homogeneous MSh with the length and thickness of a single MSh of 2–3 μm and 150 nm, respectively. The OT-dependent response of the MoO$_3$ MSh in Fig. 15b indicated an IMD pattern with a maximum at 275 °C. In addition, the cross-sensitivity of the prepared sensor to TEA among a variety of interfering gases in Fig. 15c reveals that the MoO$_3$ MSh response to TEA was highest when compared to the precursor MoO$_2$ and commercial MoO$_3$ material. The stability results of the MoO$_3$ MSh sensor during 5 month exposure to TEA gas (Fig. 15d) indicated negligible deviation of the baseline resistance (in the air), thus demonstrating an excellent repeatability of the sensor. Besides, the sensor response and recovery time measured during this period remained highly stable. The high content of O^{2-} vacancy on the MoO$_3$ surface and its chemical reaction with TEA gas molecules were identified as the prime reasons for the excellent sensing performance of the sensor.

MoO$_3$ micro-planks (MPks)

Lamellar structures such as micro-planks have recently received a lot of attention due to their large domain structures made up of abundantly assembled nanosheets. MoO$_3$ has a tendency to form a lamellar structure in order to achieve high sensing properties. Halwar et al.[158] put forth a screen printing method for the production of MoO$_3$ MPk and CuO-doped MoO$_3$ MPk for CO detection. The FESEM image in Fig. 15e illustrated the wooden plank-like structure of the agglomerated MoO$_3$ particles having thickness, width, and length in the range of 1–1.8 μm, ~7.32 μm, and 31.13 μm, respectively. Besides, the surface of
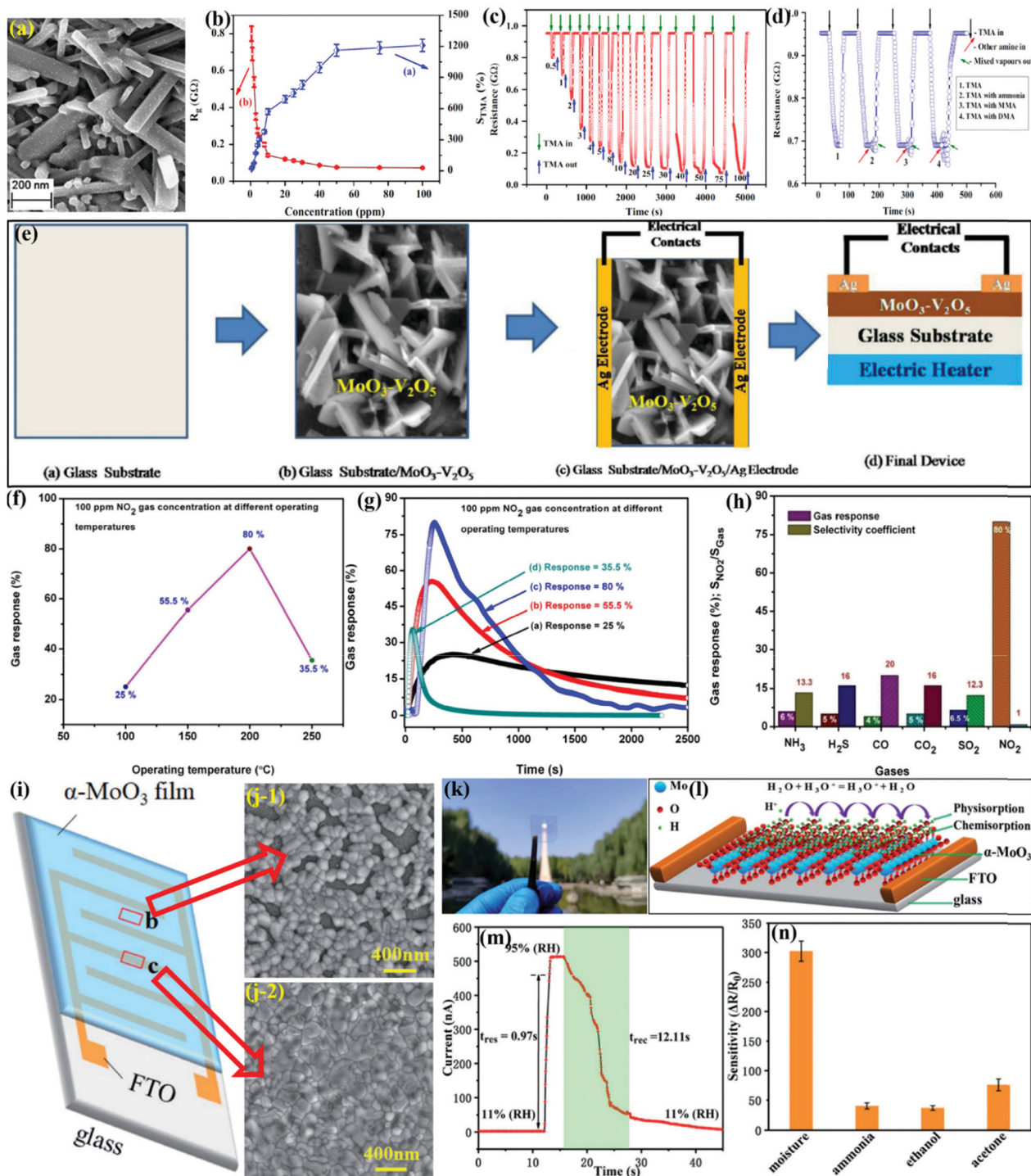
Fig. 14 (a) SEM micrograph of spray-deposited α-MoO₃ TFm with a thickness of 520 nm; (b) response of α-MoO₃ film for different TMA concentrations with error bars; (c) transient response of α-MoO₃ film for different TMA concentrations; (d) transient TMA sensing response of α-MoO₃ film in mixed amine environment. Reproduced with permission from ref. 153, copyright 2014 Elsevier. (e) The technological flow for the MoO₃–V₂O₅ gas sensor device fabrication; (f) the variation in response of (MoO₃)₀.₄(V₂O₅)₀.₆ TFm at different OTs; (g) the transient response curves of typical (MoO₃)₀.₄(V₂O₅)₀.₆ TFm; (h) the gas response and selectivity coefficient study of typical (MoO₃)₀.₄(V₂O₅)₀.₆ TFm operating at an OT of 200 °C for 100 ppm concentration of various gases. Reproduced with permission from ref. 154, copyright 2018 Elsevier. (i) Schematic device structure of the transparent humidity sensor; (j) SEM images of the α-MoO₃ TFm on the surface of channel and FTO electrode; (k) photograph of the transparent device; (l) schematic diagram of the humidity sensing mechanism for the α-MoO₃ TFm; (m) dynamic response/recovery curve for one cycle; (n) sensitivity of the device to different analytes. Reproduced with permission from ref. 156, copyright 2020 Royal Society of Chemistry.
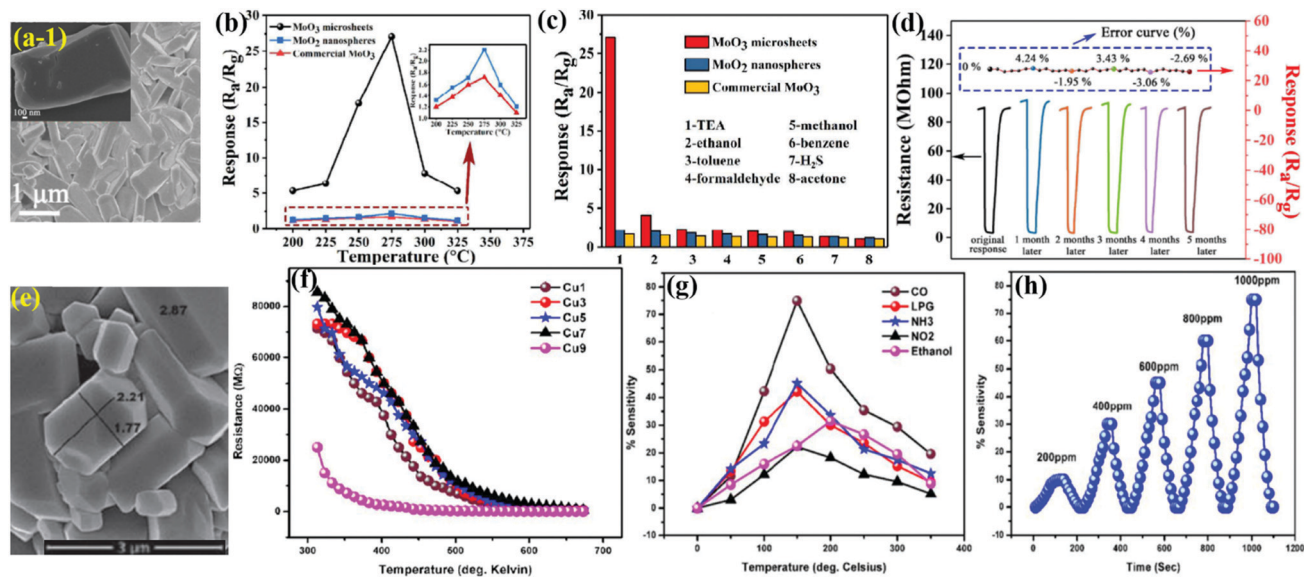
Fig. 15 (a) Typical FESEM image of the MoO₃ MSh; (b) responses of the sensors to 100 ppm TEA in the OT range of 200–325 °C; (c) responses of the sensors to different gases at 275 °C; (d) dynamic response of MoO₃ MSh-based sensors at 275 °C during 5 months exposure to 100 ppm TEA. Reproduced with permission from ref. 157, copyright 2018 Royal Society of Chemistry. (e) SEM micrographs of Cu9; (f) variation of resistance *versus* temperature for different samples; (g) sensitivity *versus* temperature for different gases at varied OT; (h) sensitivity *versus* time for various CO gas concentrations in ppm. Reproduced with permission from ref. 158, copyright 2019 IOP Publishing.

MPk was uniform with very clear boundaries and a few gaps. The results in Fig. 15f indicate that the resistance decreases with an increase in the OT, thus revealing its n-type behavior. The CO sensing results in Fig. 15g presents that the prepared materials have good sensitivity toward CO gas and the response was the highest among other test gases, while the transient curves in Fig. 15h demonstrate an increase in the sensor response with increasing CO concentration and the sensor also demonstrated quick T_{res} and T_{rec} to CO gas. Later it was concluded that the superior sensing performance was due to the collective effects of the thermal energy, excess oxygen species, and catalytic property of the copper dopants.

Three-dimensional (3-D) MoO₃ nanostructures for gas sensors

Among various morphological structures, 3-D hierarchical nano-structures (HNS) are assembled from 0-D (nanoparticles), 1-D (nanowires, nanorods, nanotubes, *etc.*), and 2-D (nanosheets) materials have become increasingly popular among researchers for various applications.[165–168] In particular, these 3-D HNS owing to their large SSA and minimized interparticle agglomerations, provides easier gas molecule diffusion and faster charge propaga-tion on the material's surface, thus resulting in high sensitivity and a faster response sensing speed.[10,169] To date, a variety of 3-D MoO₃ nanostructures, including nano/micro-flower,[83,84,166–168,170] hierarchical,[53,73,130–135] nanoarrays,[177–179] hollows spheres,[180,181] core–shell,[182–184] microcage,[185] nanopompon,[186] and microbox[187] have been designed and used in gas sensing applications (Table 3).

MoO₃ nanoflower (NFLs)

As discussed above, 3-D hierarchical nanostructures such as nano-flowers are generally constructed by low-dimensional construction units, which is an effective way to enhance the sensing properties. The group of Sui *et al.*[83] utilized a surfactant-free ST route to prepare 3-D α-MoO₃ NFLs (diameters ∼3–5 μm) consisting of microrods with diameters in the range of 150–200 nm and grown radially from the center of the NFLs. The SEM images (Fig. 16a-1) illustrate the flower-like coral morphology (average diameters ∼150–200 nm and lengths ∼2–3 μm) that seemingly grow from the MoO₂ flower center. The same results were further confirmed by the TEM image in Fig. 16a-2. The sensing results in Fig. 16b indicate that depreciation in α-MoO₃ NFLs sensor response with increasing OT from 250 to 370 °C was observed for TEA gas. In addition, superior response and high selectivity were further confirmed from the cross-sensitivity results, as shown in Fig. 16c. The transient response results for the sensor in Fig. 16d illustrate a fast response and recovery of the sensor toward TEA gas. The exciting sensing performance is the result of the high electronic conduction of the n-type MoO₃ and less agglomerated 3-D hierarchically assembled structures of MoO₃ NFLs, which provide more active sites for the adsorption of TEA molecules.

In addition, the availability of different precursors also allows different nanostructures to be synthesized using a single-step or double-step HT procedure. For example, the flower-like morphol-ogy exhibits numerous edge sites, which interact strongly with gas analytes due to their high catalytic reactivity, thus providing a high sensing response.[188] Liu *et al.*[84] utilized sodium citrate and PEG-assisted HT method to prepare hierarchical MoO₃ NFLs (Fig. 16e) for ethanol gas sensing. The SEM image in Fig. 16e displays the hierarchical and rose-like NFls architectures composed of densely packed thin porous NSs (thickness ∼15–18 nm) arranged in a multilayered stacked structure. The OT-dependent response of MoO₃ NFLs to ethanol in Fig. 16f presents an IMD response pattern with the maximum at 300 °C. Besides, the response depicts no sign of saturation with the gas concentration increasing from 100 to 700 ppm,

Table 3 A detailed overview of the gas sensing performance using 3-D MoO₃-based gas sensors

Class	Material	Synthesis route/morphology	Gas	Conc. (ppm)	Operating temp. (°C)	Response	Resp./Reco. time (s/s)	Ref.
Nano/Micro flower	MoO₃	Solvothermal + calcination	TEA	100	250	416	3/1283	83
	MoO₃	Hydrothermal	Ethanol	400	300	40	7/12	84
	MoO₃	Hydrothermal	Ethanol	100	350	22^a	20/25 (300 ppm)	166
	MoO₃	Hydrothermal	Ethanol	300	300	37.1	N.G.	167
	MoO₃/WO₃	Hydrothermal	Ethanol	100	320	28.5	13/10	168
	Zn/MoO₃	Hydrothermal	CO	50	240	31.23	10/14	170
Hierarchical nanostructures	MoO₃	Hydrothermal	Ethanol	200	340	34^a	N.G.	171
	MoO₃	Solvothermal	TEA	10	170	931.2	N.G.	172
	MoO₃	Hydrothermal	Ethanol	100	250	19.8	15/15	173
	MoO₃	Hydrothermal	Ethanol	400	300	32	3.2/2.4	77
	SnO₂/MoO₃	Chemical synthesis	Ethanol	100	260	814	1/8	174
	Fe₂O₃/MoO₃	Sacrificial template	TMA	100	240	18.6	12/106	175
	MoO₃	Hydrothermal + calcination	Ethanol	200	260	80	16/10	57
	MoO₃/In₂O₃	Hydrothermal	Ethanol	100	185	7	11/94	176
Nanoarrays	Y/MoO₃	Solid state chemical reaction	Xylene	100	370	28.3	1/15	177
	MoO₃	Solid state chemical reaction	Xylene	100	370	19.2	1/15	178
	Fe/MoO₃	Solid state chemical reaction	Xylene	100	340	28.5	2/21	179
Hollow spheres	Au/MoO₃	Solvothermal	Xylene	100	250	22.1	118/289	180
	MoO₃/Bi₂Mo₃O₁₂	Solvothermal	TMA	50	170	25.8	7.1/N.G. (100 ppm)	181
Core–shell	MoO₃/ZnO	Hydrothermal + atomic layer deposition	Ethanol	200	350	7.6	44.8/119/8	182
	MoO₃/NiO	Hydrothermal + sintering	Acetone	100	350	20.3	17/131	183
	MoO₃/Fe₂(MoO₄)₃	Hydrothermal + calcination	H₂S	1	70	1.7	20/70	184
Microcage	MoO₃	Hydrothermal	Ethanol	200	350	43	N.G.	185
Nano pompon	Ni/MoO₃	Solvothermal	Xylene	100	250	62.6	1/50	186
Microbox	MoO₃	Hydrothermal	Ethanol	100	260	78	15/5	187

^{a} Not given.
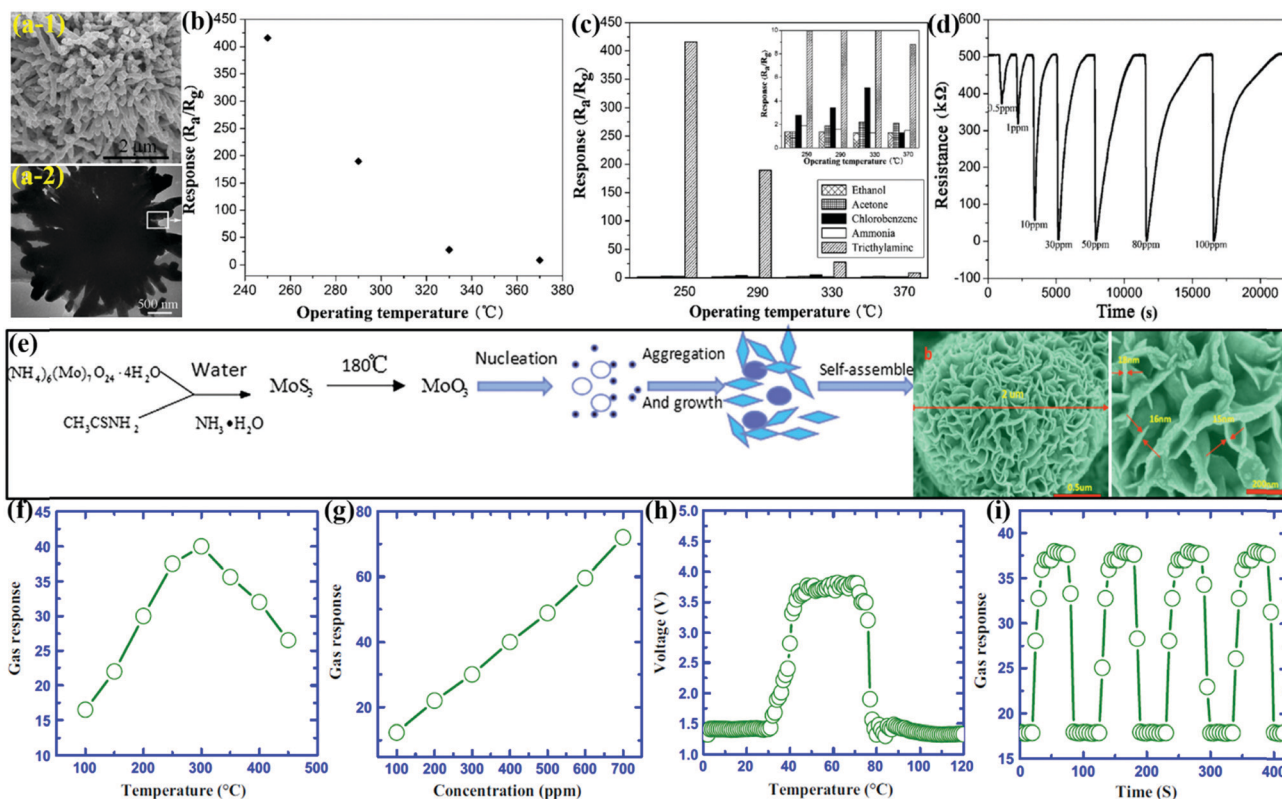
Fig. 16 (a) Typical SEM and TEM images of α-MoO₃ flower-like HNS; (b) the responses of the α-MoO₃ thick-film sensor *versus* the OT to 100 ppm TEA gas; (c) the responses of the α-MoO₃ thick-film sensor to 100 ppm gases at different OTs; (d) the transient response-recovery characteristics of the α-MoO₃ sensor with different concentrations of TEA gas at the OT of 250 °C. Reproduced with permission from ref. 83, copyright 2015 Elsevier. (e) Schematic illustration of the possible formation process for the MoO₃ NFL architectures and the SEM image of the aggregated state of NFLs; (f) gas response to ethanol (400 ppm) at a series of OT; (g) gas response to varied ethanol concentrations at OT of 300 °C; (h) gas response and recovery curves of the sensors; (i) repeat response–recovery characteristics of the sensors. Reproduced with permission from ref. 84, copyright 2016 Springer.

as shown in Fig. 16g. The voltage of the sensor under different OT revealed the highest voltage from 40 to 80 °C (Fig. 16h), whereas the voltage sharply increases when ethanol gas is purged in the chamber while it returns to its original state when the ethanol gas is out of the measurement chamber. The repetitive response results in Fig. 16i demonstrated no significant change in the sensor response while delivering a fast T_{res} and T_{rec} for the sensor. The excellent response to ethanol was accredited to the high SSA and high S/V ratio of MoO_3 NFLs, which assisted in improving the reaction sites for gas analytes.

Wang *et al.*[170] experimentally carried out and theoretically verified (with DFT) the detection of CO using Zn-doped MoO_3 hierarchical microflowers using density of states (Scheme 5). As can be seen, a significant amount of deformation of the Zn–MoO_3 surface was observed on account of the adsorption of CO, and a charge transfer value of 0.451e was obtained, thus indicating strong chemisorption. Electron transfer during the adsorption process was verified from the distinct continuous region in Scheme 5b, which is related to the formation of new chemical bonds. A shifting to the lower energy after adsorption was observed in the DOS curves, which indicate the chemical action in this system. Finally, the introduction of Zn atom promoted the adsorption ability of $MoO_3(010)$, which supports the experimental results showing the superior gas-sensing performance of Zn–MoO_3 samples to CO.

MoO_3 hierarchical nanostructures (HNS)

Hierarchical nanostructures are perceived as one of the most promising materials and have been widely used in gas sensors due to nanoporous structures with less agglomerated architectures. Li *et al.*[171] presented the hexadecyl trimethyl ammonium bromide (CTAB)-assisted HT synthesis of α-MoO_3 HNS NBs, which self-assembled into bundles and aggregate into bird's nest-like shape HNS and demonstrated superior ethanol sensing performance. The SEM and TEM images in Fig. 17a-1 and a-2 respectively display the presence of a bird's nest-like HNS with perfectly aligned nano- or micro-porous structures. The width of the single NB is about 250–500 nm, which is wider than that of the monodispersed NBs; this could be due to the side-sharing assembly of the two NBs with the help of CATB. The OT-dependent response of the MoO_3 NBs and MoO_3 HNS in Fig. 17b reveals the ∼2.3 folds higher response of MoO_3 HNS than its counterpart at 340 °C, while its response is always higher than that of MoO_3 NBs at all the temperature values. The transient response curves in Fig. 17c demonstrate the good repeatability of sensor response at its ground state, although the response/recovery kinetic property of the MoO_3 HNS was much better than that of the MoO_3 NBs. The superior sensing performance was accredited to the nanoporous geometry, which, owing to its minimized stacking configuration, provides abundant sites for chemical reaction as well as effective diffusion channels for gases.
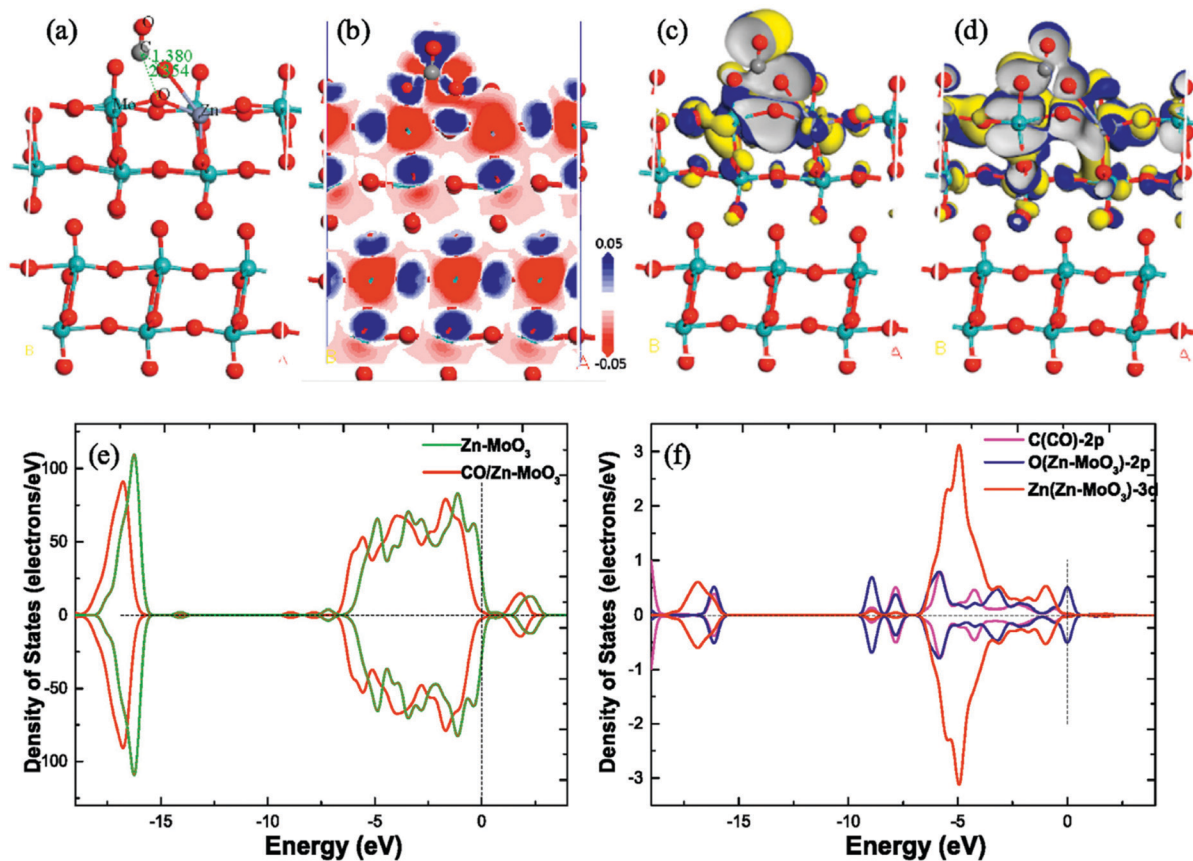
Scheme 5 (a) The structure, (b) deformation charge density, (c) HOMO, (d) LUMO, (e) DOS, and (f) PDOS of CO-adsorbed MoO3 (010) adsorption system. Reproduced with permission from ref. 170, copyright 2020 Elsevier.
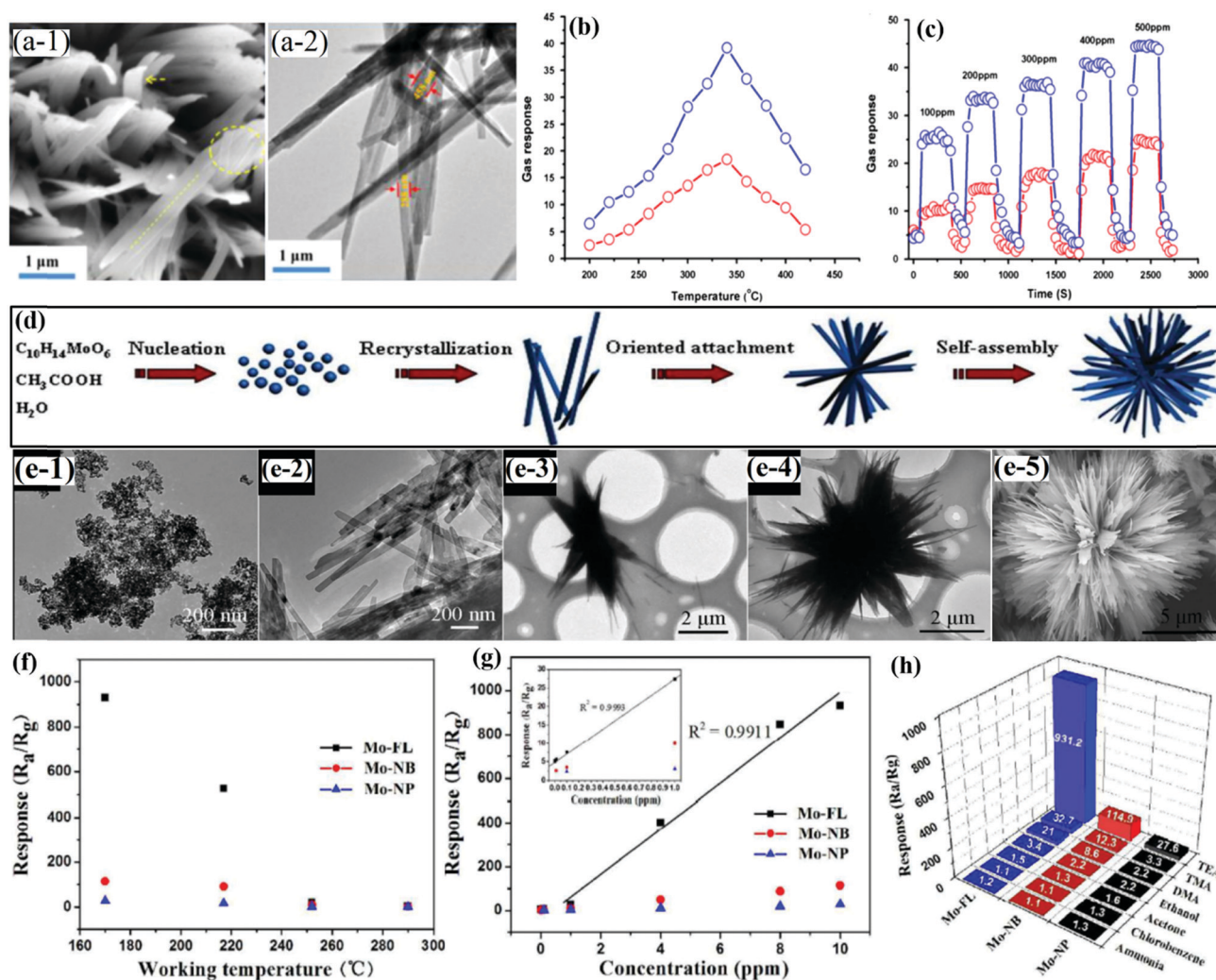
Fig. 17 (a) SEM and TEM images of nest-like MoO$_3$; (b) response vs. temperature toward 200 ppm ethanol; (c) ethanol concentration vs. response property at 340 °C, blue line symbol for nest-like MoO$_3$ and red for monodispersed MoO$_3$ NBs. Reproduced with permission from ref. 171, copyright 2015 Elsevier. (d) Schematic of the formation process of the α-MoO$_3$ NFLs; (e-1 to e-4) TEM micrographs of the intermediate products collected at different reaction stages; (e-5) SEM images of the α-MoO$_3$ product prepared for 8 h; (f) the response vs. OT to 10 ppm TEA gas; (g) the response vs. varied TEA concentration; (h) the response to 10 ppm of various gases, reproduced with permission from ref. 172, copyright 2015 Royal Society of Chemistry.

In another work, Sui and coworkers[172] prepared a 3-D flower-like α-MoO$_3$ HNS from 1-D single-crystalline NBs *via* a one-step template-free ST method and achieved the fast detection of TEA at 170 °C. The growth process of α-MoO$_3$ HNS, as depicted in Fig. 17d, revealed the formation of flower-like nanostructures from precursor nanoparticles and nanobelts. The mechanism of formation was further supported by the TEM images in Fig. 17e1 to e4. The SEM image in Fig. 17e5 displays the presence of numerous NBs (thickness ∼20–30 nm) with interconnected sharp tips and rough rims, which are radially assembled into flower-like shapes. The temperature-dependent response in Fig. 17f indicated a decrease in the responses of the sensors toward TEA gas with an increase in the OT 170 to 290 °C. The response of the sensor as a function of TEA concentrations in Fig. 17g presented that the MoO$_3$ HNS possesses the highest response among other MoO$_3$ nanostructures. The cross-sensitivity results in Fig. 17h reveal that an excellent response was observed toward TEA gas. The research

group ascribed the superior sensing performance to the following reasons: (1) the fast oxidation of TEA gas, (2) superior electronic conduction of MoO$_3$, (3) 3-D hierarchically assembled structures, and (4) large SSA and pore volume of the α-MoO$_3$ HNS.

As one of the important VOCs, ethanol still requires a reliable and robust sensor for applications in breath analysis, food industries, and the biomedical field. Several approaches have been used to improve the sensing performance of metal oxide-based ethanol sensors. Xia et al.[173] utilized the facile HT method to prepare 3-D porous α-MoO$_3$ sponges with 1-D NRs as the building blocks. The schematic in Fig. 18a illustrates the formation of porous sponges, wherein some NRs randomly grown on the lateral surface of other NRs evolve into a branch, which is well criss-crossed to form porous sponges. The SEM image in Fig. 18b indicates the monodispersed NRs (length of 100–200 nm) assembled into porous, spongy-like hierarchical structure with abundant interconnected hollow spaces. The gas-sensing
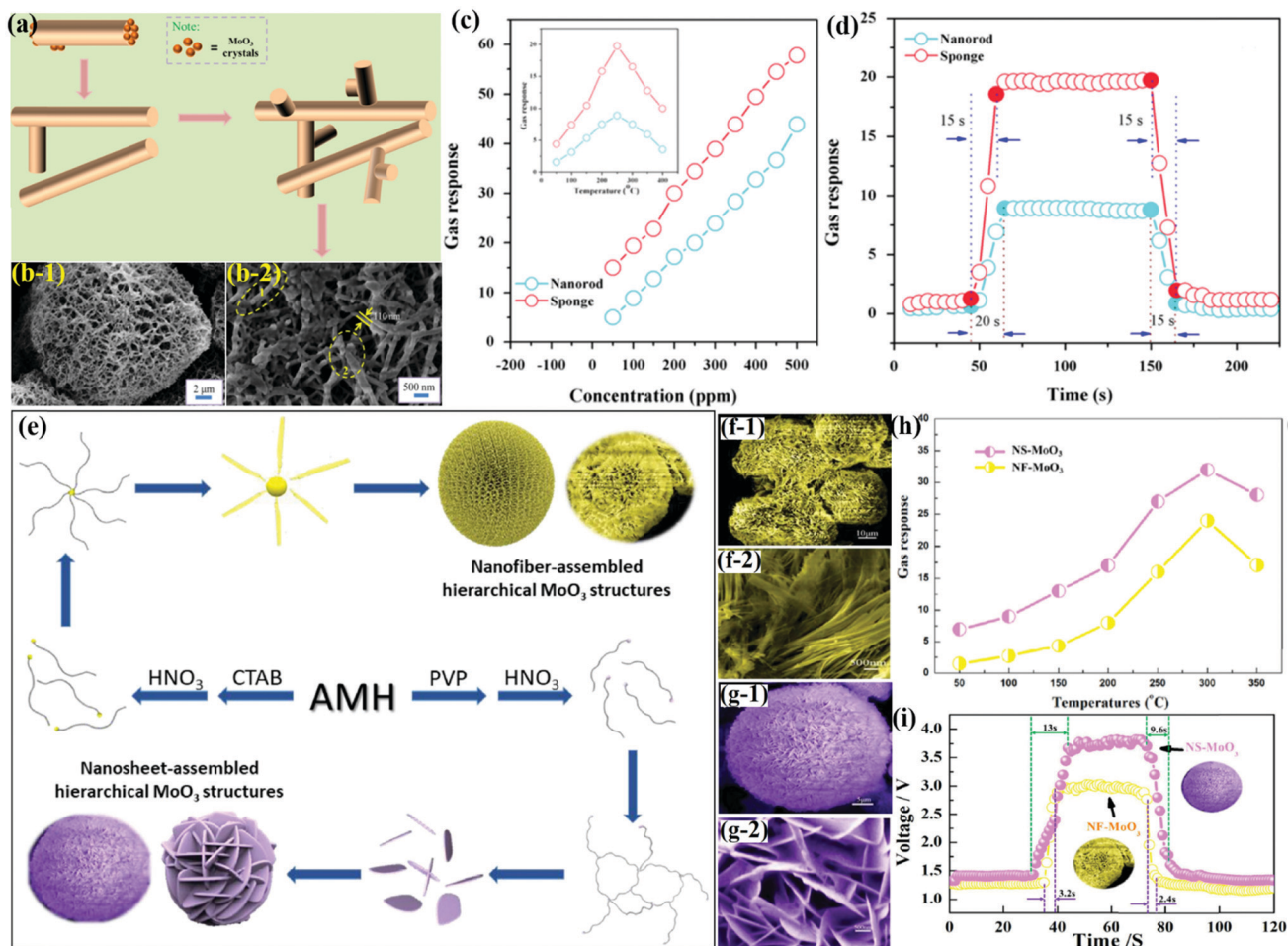
Fig. 18 (a) Schematic illustration of the evolution process of porous α-MoO$_3$ sponges; (b) SEM images of porous α-MoO$_3$ sponges; (c) responses to ethanol with different concentration at 250 °C, (inset) response *versus* the operating temperature of the two sensors exposed to 100 ppm methanol; (d) dynamic ethanol sensing transient toward 100 ppm ethanol at 250 °C. Reproduced with permission from ref. 173, copyright 2016 Elsevier. (e) Schematic diagram of the possible formation mechanism for the NFbs-assembled and the NSs-assembled hierarchical MoO$_3$ structures; (f) SEM images of the NFbs-assembled hierarchical MoO$_3$ structures; (g) SEM images of the NSs-assembled hierarchical MoO$_3$ structures; (h) the gas response to 400 ppm ethanol at different OTs; (i) response–recovery characteristics of the sensors at 300 °C to 400 ppm ethanol. Reproduced with permission from ref. 77, copyright 2019 Elsevier.

performance in Fig. 18c reveals that the 3-D porous α-MoO$_3$ sponges possess ∼2 times greater response than monodispersed MoO$_3$ nanorods in all the concentration ranges. Fig. 18d further indicates that both the sensors possess similar response–recovery dynamics. It was later concluded that the improved sensing performance was not only due to the interconnected porous structures but also due to the significant fraction of the atoms participating in ethanol gas-sensing reaction.

Similarly, Li and coworkers[77] used CTAB and polyvinyl pyrro-lidone (PVP) to respectively prepare NFbs and NSs assembled MoO$_3$ HNS under HT conditions (Fig. 18e). The SEM images of the NFs-assembled MoO$_3$ HNS in Fig. 18f-1 and f-2 clearly demon-strate the presence of a large number of NFs having size in the range of 20–25 μm and assembled around an invisible center. For the NSs-assembled MoO$_3$ HNS in Fig. 18g-1 and g-2, smooth NSs (thickness ∼20–30 nm) were arbitrarily arranged on the surface of the sphere, while numerous NSs were found to cut across each other. The OT-dependent response in Fig. 18h reveals the better

ethanol sensing performance of NS-MoO$_3$ HNS than that of NF-MoO$_3$ HNS. This case was the same as that in the case with the response/recovery results, given in Fig. 18i. It was later concluded at the high response of NS-MoO$_3$ HNS was due to its higher SSA and the scattered intersection of various NSs on the spherical surface, which causes the formation of semi-closed spaces on the surface of NS-MoO$_3$ HNS.

MoO$_3$ nanoarrays (NARs)

From the perspective of human health, most VOCs are toxic and hazardous. Xylene is a carcinogenic gas from the BTX (benzene, toluene, and xylene) group.[14,137] To detect xylene gas, Qin *et al.*[177] utilized a two-step solid-state chemical reaction route to prepare Y-doped α-MoO$_3$ NARs composed of nanorods (NRs). The SEM image in Fig. 19a displays the presence of orderly self-assembly NARs having a diameter of about 30 nm. The cross-sensitivity results in Fig. 19b reveal that the Y/α-MoO$_3$ NARs have better selective response than that of the pristine α-MoO$_3$
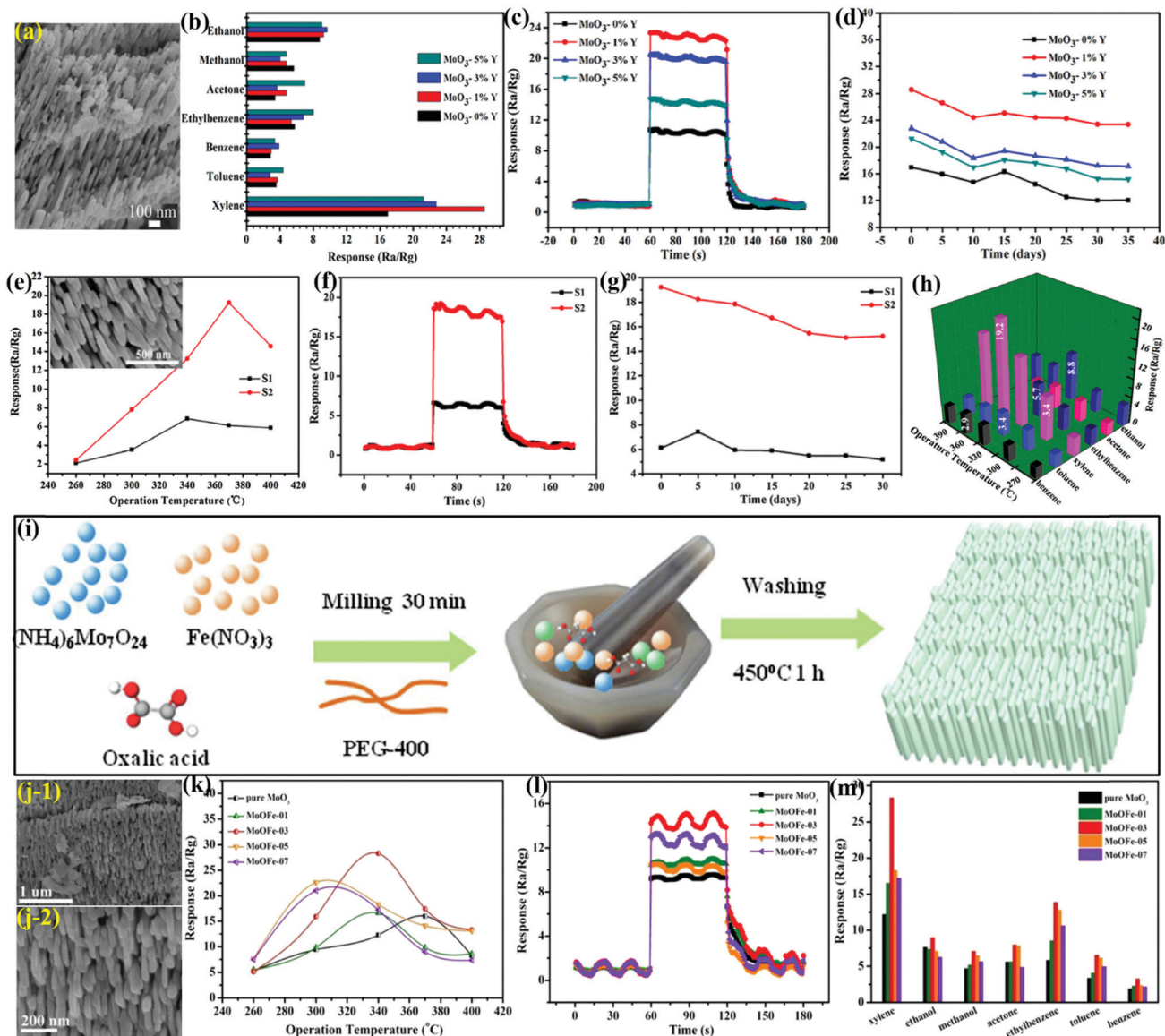
Fig. 19 (a) The SEM image of 1% Y-doped sample; (b) the response curve of the samples to 100 ppm of different gases at the OT of 370 °C; (c) the response/recovery curve of the samples for 100 ppm xylene at 370 °C; (d) the stability of the samples for 100 ppm xylene at 370 °C. Reproduced with permission from ref. 177, copyright 2017 Elsevier. (e) The response to 100 ppm gas at different OTs, (inset) the SEM images of samples S2; (f) the dynamic response curves to 100 ppm xylene at 370 °C; (g) the stability of the samples to 100 ppm xylene at 370 °C; (h) the response of sample S2 to 100 ppm gas at the different OTs. Reproduced with permission from ref. 178, copyright 2017 Elsevier. (i) A schematic representation for the synthesis of Fe-doped MoO₃ NARs; (j) SEM images of MoOFe-03; (k) the response curves of the samples to 100 ppm xylene at different OTs; (l) the response and recovery curves for 100 ppm xylene at 340 °C; (m) the response of the samples to 100 ppm of different gases at 340 °C. Reproduced with permission from ref. 179, copyright 2020 Elsevier.

to all the gases; however, the highest response was observed for xylene gas. The transient response curves in Fig. 19c revealed a very fast response time of the sensors, whereas the long-term stability of the sensors for 30 days in Fig. 19d displayed that the response value decreases with time. It was concluded that the defects induced in α-MoO₃ NARs after Y-doping allow larger contact area between α-MoO₃ and xylene molecules. Besides, the Y dopants, along with increasing electron donor defects and oxygen vacancies, assisted in accelerating the mobility of oxygen ions, thus resulting in better response toward xylene gas.

Similarly, Qin and coworkers[178] utilized a solid-state chemical reaction route to prepare α-MoO₃ 2-D nanoplates (thicknesses ~50 nm) and developed self-assembled orderly NARs (inset of Fig. 19e). The OT-dependent response to xylene in Fig. 19e indicated that the sensor based on S2 (NARs) exhibited better sensing performance than the sensor based on S1 (NPts) but a higher OT due to the close array structure of S2. The transient response in Fig. 19f indicated a fast response/recovery time for both the sensors, wherein the response time was close to 1 s toward xylene gas. The stability results in Fig. 19g reveal that the response was the highest on the 5th day, which observed a sharp

drop on the 10th day and stabilized on the 20th day. Besides, the cross-sensitivity results in Fig. 19h demonstrate the highest response toward xylene gas. This excellent sensing performance was attributed to the relatively larger SSA and preferential exposure of the active crystal face.

To further enhance the sensor performance compared to pristine α-MoO$_3$, Qin and his group[179] used a facile solid-state chemical reaction method to develop Fe-doped α-MoO$_3$ (Fig. 19i). The orderly array structure self-assembled by the NPTs is observed in the SEM images in Fig. 19j. The OT-dependent response to xylene gas in Fig. 19k displayed an IMD pattern, whereas the Fe-loaded samples showed better response at a relatively lower temperature than that of pristine MoO$_3$. The response–recovery transients in Fig. 19l demonstrated a fast response time for all the Fe doped α-MoO$_3$ materials because the presence of Fe ions generates more oxygen vacancies on the surface of the sensor, which is not the case with pure MoO$_3$. The cross-sensitivity results in Fig. 19m revealed that the Fe-doped α-MoO$_3$ NARs displayed the highest response to xylene gas due to the presence of the benzene ring-like structure, which provides a greater number of electrons for reacting with the oxygen species absorbed on the surface of the sensor. It was concluded that the excellent sensing features of Fe-doped MoO$_3$ NARs arise from their larger SSA, which generates more reactive sites, thus resulting in enhanced sensing response to xylene gas.

MoO$_3$ hollow spheres (HSp)

3-D nanostructures, such as hollow spheres and mesoporous structures, have frequently been used for gas sensing applications. There are a plethora of synthetic routes used to design these nanostructures but the solvothermal approach has been paid much more attention due to the easy and cost-effective approach for a controlled morphology. Sui et al.[180] utilized a combination of template-free ST method and the calcination process to synthesize monodisperse, hierarchical α-MoO$_3$ HSp of average diameters $\sim$400–600 nm (Fig. 20a). The OT-dependent sensing performance toward xylene in Fig. 20b displayed an IMD pattern with the maximum response at 250 °C, which was 40 °C less as compared to that of pure α-MoO$_3$ (290 °C). The cross-sensitivity results in Fig. 20c indicate poor selectivity for pure α-MoO$_3$, whereas the optimized Au/α-MoO$_3$ HSp demonstrated maximum sensitivity to xylene gas, among others. Besides, the sensor displayed poor sensing performance to gases including ethanol, hydrogen, ammonia, acetone, formaldehyde, and chlorobenzene (Fig. 20d). The reason for the improved sensing performance could be due to the Au NPs, which on coordinating with the aromatic rings of xylene, dissociate them faster as compared to the other test gases. Using a similar ST strategy, Zhang and coworkers[181] reported for the first time MoO$_3$/Bi$_2$Mo$_3$O$_{12}$ hollow microspheres for detecting TMA gas. The SEM and TEM images in Fig. 20e display the presence of a hollow microsphere (diameter $\sim$1.2 μm) whose surface was found to be smooth with some pores observed on it. The temperature-dependent response toward TMA in Fig. 20f reveals a depreciation in the sensor response as the OT increases from 170 to 330 °C. The real-time gas response results to TMA at 170 °C in Fig. 20g presents an increase in the response with the increase in the TMA concentration, and an excellent linear relationship with TMA was also observed. The cross-sensitivity results in Fig. 20h unveil the excellent response toward TMA gas, which could be ascribed to the unique HSp morphology that provides an excellent surface for
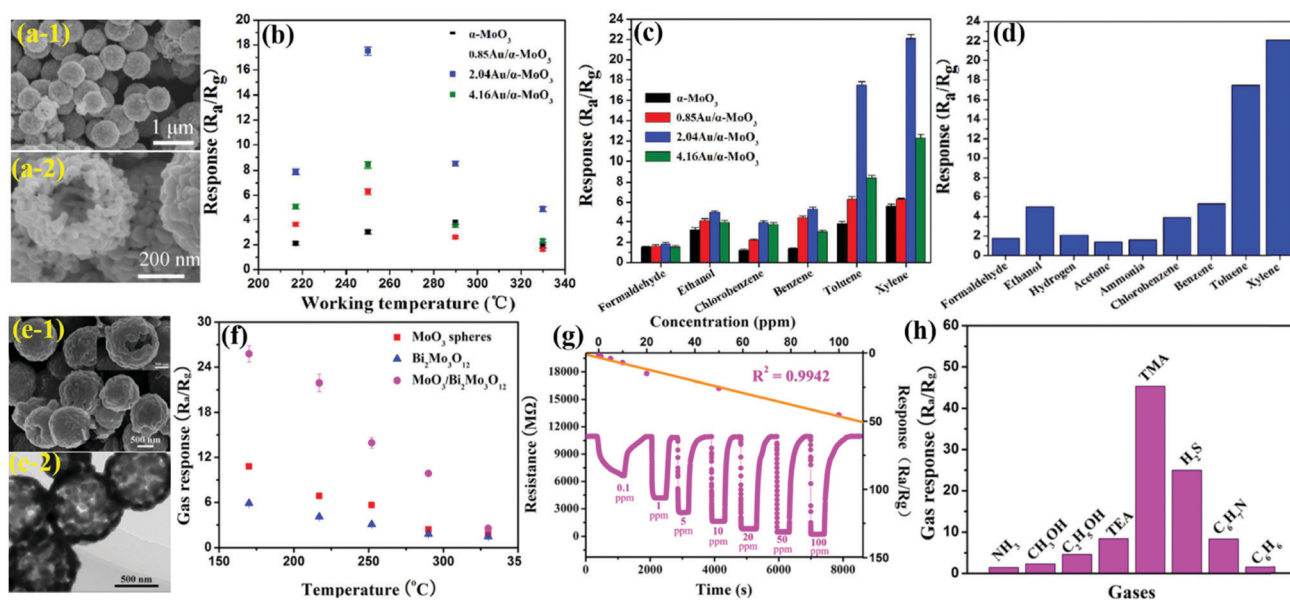
Fig. 20 (a) The SEM images of a single sphere obtained by calcination; (b) the responses vs. the OT to 100 ppm toluene gas; (c) the responses vs. 100 ppm various gases at their relative optimized OTs; (d) the responses of 2.04Au/α-MoO$_3$ sensor versus 100 ppm gases. Reproduced with permission from ref. 180, copyright 2017 American Chemical Society. (e) SEM and TEM images of the calcined MoO$_3$/Bi$_2$Mo$_3$O$_{12}$ spheres; (f) responses of the sensors toward 50 ppm of TMA at different OTs; (g) the gas response–recovery characteristics of the MoO$_3$/Bi$_2$Mo$_3$O$_{12}$ sensor to varied concentrations of TMA measured at 170 °C; (h) the responses of the MoO$_3$/Bi$_2$Mo$_3$O$_{12}$ sensor toward 100 ppm of various gases. Reproduced with permission from ref. 181, copyright 2019 American Chemical Society.

the diffusion and reaction of TMA molecules, and the synergistic effect from the heterojunction between MoO_3 and $Bi_2Mo_3O_{12}$.

MoO_3 core–shell (CSh)

In recent times, researchers have proposed highly effective and advanced sensors based on porous core–shell (CSh) structures with higher selectivity and stability. Lee *et al.*[182] utilized the HT method to prepare the MoO_3 core and the atomic layer deposition (ALD) method to deposit ZnO shell and then prepared MoO_3–ZnO CSh nanorod sensors (Fig. 21a). The SEM image in Fig. 21b-1 depicts a typical rod-like morphology with diameter and length of $\sim$100 nm and $\sim$1000 nm, respectively, whereas the TEM image in Fig. 21b-2 reveals that the NR consists of a central core (diameter $\sim$120 nm) surrounded by a shell (thickness $\sim$30 nm). The OT-dependent sensing performance in Fig. 21c indicates that the MoO_3-ZnO CSh sensor shows better response than pristine MoO_3 at all temperature ranges. The cross-sensitivity results in Fig. 21d revealed that the MoO_3–ZnO CSh sensor showed good selectivity toward ethanol, among others. The long-term stability results in

Fig. 21e showed that the MoO_3–ZnO CSh sensor response is highly stable and repeatable.

Similarly, in another work, Xu and coworkers[183] anchored NiO porous NSs on α-MoO_3 NBs using a simple method and developed the α-MoO_3@NiO CSh P–N heterostructured nanocomposite (Fig. 21f). The SEM images in Fig. 21g revealed the structure of α-MoO_3, which is composed of 1D NBs with a uniform size distribution. This structure of NBs was well-maintained in α-MoO_3@NiO CSh; however, the surface becomes coarser than that of pristine α-MoO_3 NBs, which could be due to the successful growth of NiO NSs on its surface in the process of forming the CSh structure. The sensing results in Fig. 21h exhibit an IMD kind of volcano-shaped pattern toward acetone gas, wherein the optimized α-MoO_3@NiO CSh nanocomposite sensor demonstrated the highest response at its optimal OT due to the highest amount of heterogeneous interfacial bonds. Besides, the response to acetone gas was also the highest (Fig. 21i) among other interfering test gases. The high sensing performance of α-MoO_3@NiO CSh was attributed to its larger SSA, which was readily available for surface reactions and also the formation of p–n heterojunction among NiO and α-MoO_3.
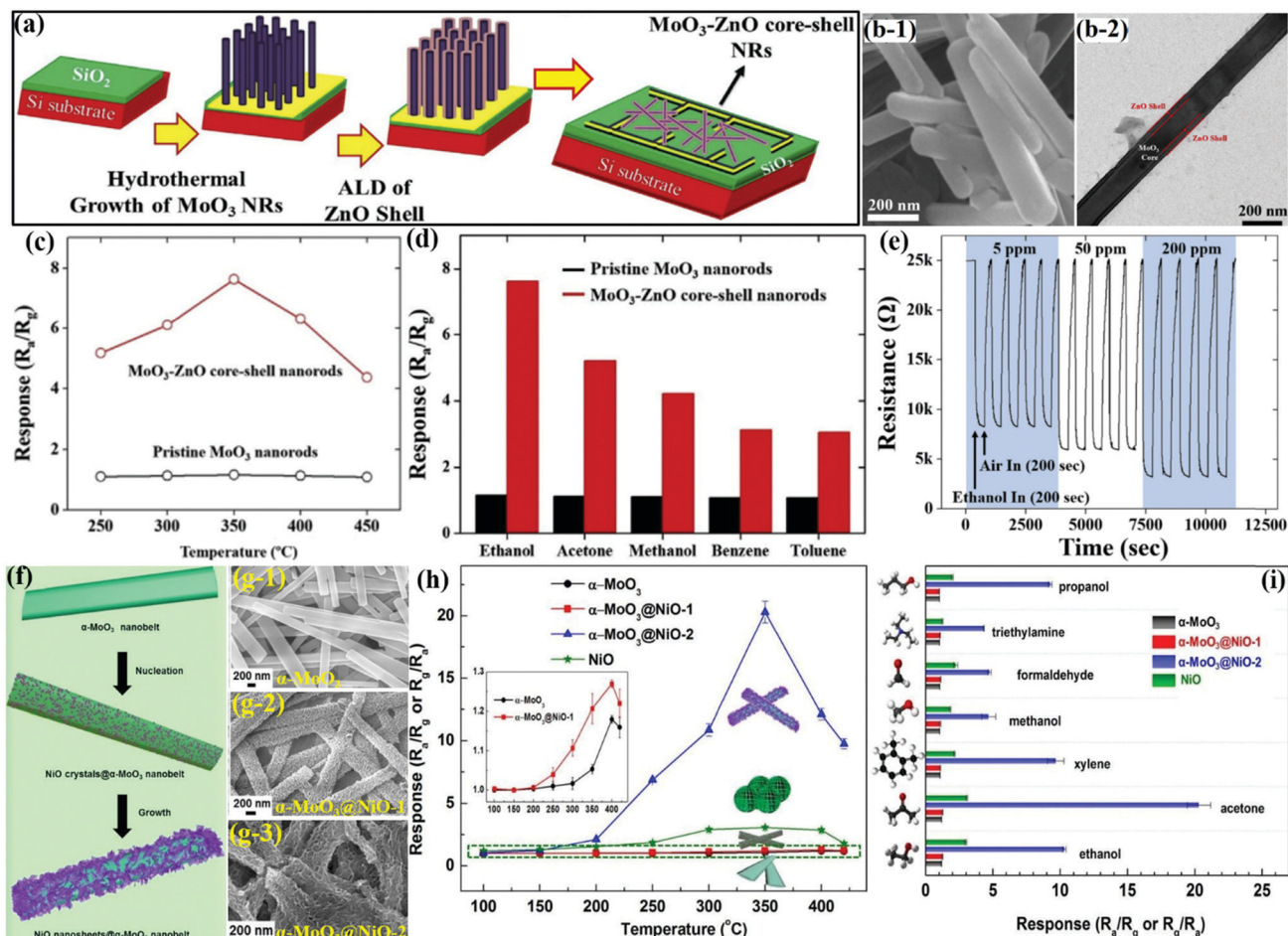
Fig. 21 (a) Schematic representation of the synthesis of MoO_3-ZnO CSh; (b) SEM and TEM images of MoO_3-ZnO CSh NRs; (c) response of the prepared materials to 200 ppm ethanol at different OTs; (d) selectivity of the pristine MoO_3 and MoO_3-ZnO CSh NR sensor at 350 °C; (e) long-term stability of the MoO_3–ZnO CSh NR sensor at 350 °C. Reproduced with permission from ref. 182, copyright 2018 Elsevier. (f) Schematic illustration of the synthesis of α-MoO_3@NiO composites; (g) SEM images of the as-prepared materials; (h) response *vs.* OT for 100 ppm acetone gas; (i) selectivity toward 100 ppm various gases at their optimal OTs. Reproduced with permission from ref. 183, copyright 2019 Royal Society of Chemistry.

MoO$_3$ microcage (MCg)

One of the metal oxide nanostructures, such as the microcage, is known for its peculiar high-surface architectures conducive for adequate oxygen adsorption and ability to interact with target gas species on the surface. Zhu et al.[185] utilized a facile template-free HT method to prepare hollow MoO$_3$ microcage as a result of the inside-out Ostwald-ripening and the acidic etching processes (Fig. 22a). The SEM image in Fig. 22b-1 display the solid MoO$_3$ polyhedrons with a diameter in the range of 1.5–4 μm, while the SEM image of MoO$_3$ MCg in Fig. 22b-2 presents a well-shaped hollow cage structure having a smooth surface and a diameter of

about 1–1.5 μm. Open holes were also observed on the cage surface, which exposes the hollow interior space. The OT-dependent sensing performance to ethanol in Fig. 22c displays an IMD pattern, wherein the hollow cage-based sensor demonstrated better response than the solid polyhedron toward ethanol gas. The response transients of both MoO$_3$-based sensors to ethanol in Fig. 22d indicated good repeatability as no change in the responses after four reversible cycles was observed for both the sensors. It was concluded that gas adsorption and diffusion were highly facilitated in the hollow MoO$_3$ cages, which provided a larger number of surface-active sites for enhancing the ethanol response.
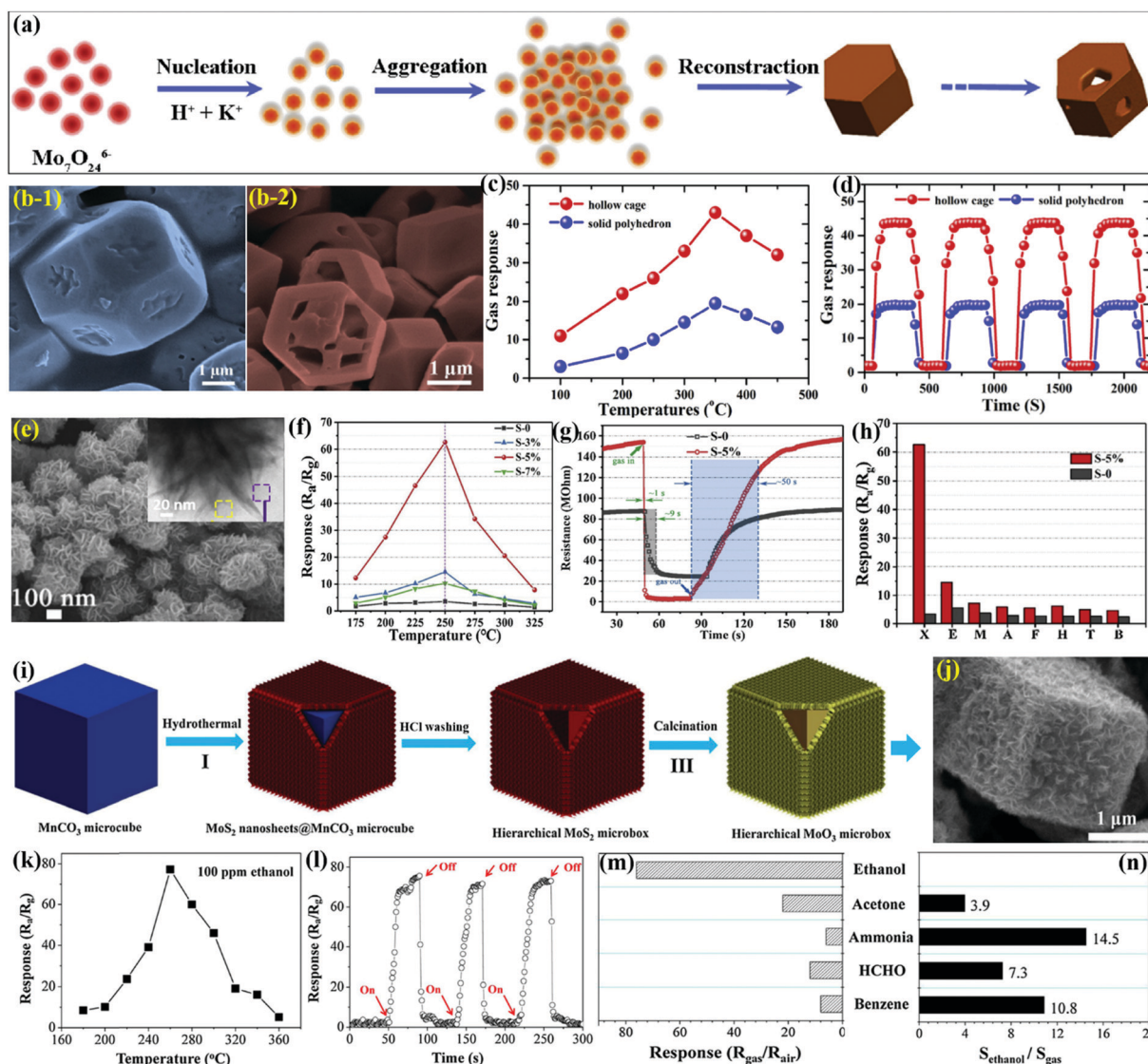
Fig. 22 (a) Growth mechanism of hollow MoO$_3$ cage; (b-1) SEM images of solid MoO$_3$ polyhedrons; (b-2) SEM images of hollow MoO$_3$ MCg; (c) the gas response vs. OT for 200 ppm ethanol gas; (d) the gas response of the two sensors toward different gas concentrations at 350 °C. Reproduced with permission from ref. 185, copyright 2019 Elsevier. (e) FESEM images of S-5% NPMn, (inset) TEM image of S-5%; (f) responses vs. OTs to 100 ppm xylene gas; (g) response and recovery curves of S-0 and S-5% sensors; (h) responses to 100 ppm different test gases (X: xylene, E: ethanol, M: methanol, A: acetone, F: formaldehyde, H: hydrogen sulfide, T: toluene, B: benzene) at 250 °C, reproduced with permission from ref. 186, copyright 2019 Elsevier. (i) Schematic illustration of the formation process of hierarchical MoO$_3$ MBx; (j) FESEM image of hierarchical MoO$_3$ MBx; (k) response of the sensor based on hierarchical MoO$_3$ MBx to 100 ppm of ethanol at different OTs; (l) response/recovery curves of sensors to 100 ppm ethanol at 260 °C; (m) gas response of hierarchical MoO$_3$ MBx to 100 ppm test gases at 260 °C; (n) selectivity to ethanol ($S_{ethanol}$ and S_{gas}, gas responses to ethanol and other gases, respectively). Reproduced with permission from ref. 187, copyright 2017 Elsevier.

MoO$_3$ nano-pompon (NPMn)

Xylene is one of the major VOCs commonly used in the paint industry, and its overexposure may cause skin irritation, hearing and memory loss, and may pose a risk of neurasthenia syndrome. The accurate detection of this toxic analyte is, therefore, essential to ensure a healthy and clean working environment. Jiang et al.[186] used a facile ST method to develop Ni-doped MoO$_3$ NPMn and demonstrated superior xylene sensing properties. The SEM image in Fig. 22e unveils the presence of rough pompons having a diameter of 200–300 nm, while the inset (TEM image) unveils the presence of 2-D NSs assembling into the pompons. The OT-dependent sensing response in Fig. 22f indicates an IMD pattern, wherein peak performance was observed at 250 °C. Besides, Ni/MoO$_3$ NPMn displayed a better sensing response than pristine MoO$_3$ at every temperature range. The transient response curves in Fig. 22g reveal a very fast T_{res} for the optimized Ni/MoO$_3$ NPMn toward xylene gas due to an increase in the number of reactive sites by Ni doping. The cross-sensitivity results in Fig. 22h reveal that Ni/MoO$_3$ NPMn demonstrated better response to every gas (highest for xylene) than pristine MoO$_3$ under similar testing conditions. It was concluded that the high SSA obtained and finely-tuned crystallite size after Ni-doping induced changes in the oxygen composition and were responsible for the improved xylene sensing performance.

MoO$_3$ microboxes (MBx)

Other metal oxide nanostructures, such as microboxes, are known for their hierarchical and hollow structures to enhance the sensitivity due to their accessible surface to adsorbed oxygen species and more active sites. Furthermore, their high surface-to-volume ratio mass transfer accessibility could help to achieve rapid response/recovery to the target gas. Zhang et al.[187] used the HT method to prepare hierarchical MoO$_3$ MBx from MnCO$_3$ microcubes (MCBs) as the templates. Fig. 22i revealed the formation of MoO$_3$ MBx, wherein, firstly, the nanocomposite of uniform MnCO$_3$ MCBs and MoS$_2$ NSs was prepared by an NT method to form MoS$_2$@MnCO$_3$ CSh MCBs, following which the MnCO$_3$ MCBs templates were removed by HCl washing to obtain the hierarchical MoS$_2$ MCBs, which were calcined at high temperatures to prepare hierarchical MoO$_3$ MBx. The SEM image in Fig. 22j revealed the presence of regular MCBs of size about 2–3 μm along with some small openings on its surface, which indicated the hierarchical and hollow MCB structure of the MoO$_3$ samples. The OT-dependent sensing response in Fig. 22k indicated an IMD pattern with the maximum response to ethanol gas at 260 °C. The reproducibility of the sensor toward ethanol gas tested in 3 cycles (Fig. 22l) represented no change in the sensing performance along with a fast T_{rec} of the sensor. The cross-sensitivity results in Fig. 22m and selectivity coefficients in Fig. 22n indicate that under identical testing conditions, the sensor responded excellently to ethanol, which was a result of the hierarchical and hollow structure of MoO$_3$ MBx.

Conclusion and future scope

This review follows the recent progress and developments made in the thematic domain of gas sensing for various MoO$_3$ nanostructures. Herein, we have summarized the different morphologies and structures of MoO$_3$, each with a peculiar sensing performance toward a particular target gas. Various top-down and bottom-up approaches to fabricate MoO$_3$ nanostructures with different sizes and shapes have been discussed in detail. This comprehensive review concluded the very fact that the morphologies of MoO$_3$ that possess a high surface-to-volume ratio, e.g., nanotubes, nanoflowers, hierarchical nanostructures, core–shell, and microspheres, have been able to attract great attention of the researchers as these morphologies allow for the easy penetration of gas molecules in their porous structure, thus resulting in high sensor response. The sensing performance of these nanostructures has been reviewed to detect various hazardous and flammable gases and organic vapors such as ammonia, nitrogen dioxide, hydrogen sulfide, chlorine, carbon monoxide, ethanol, formaldehyde, acetone, and methanol. Generally, MoO$_3$-based gas sensors show high sensitivity and lower detection limit; however, their selectivity and operation temperature are major concerns. Some strategies are used to overcome the problem, such as surface modification using noble metal NPs or doping/modification with other material and light illumination but they do not entirely fulfill the requirement for the usage of MoO$_3$ in commercial applications. Following are the key conclusions of MoO$_3$-based gas sensors to improve their sensing performance.

(a) The response could be enhanced using porous and hollow structures as they can provide fast adsorption–desorption, diffusion, and transmission of gas molecules to achieve high sensor response at low concentrations.

(b) Surface modification using noble metals or doping of metal ions could increase the number of reaction sites on the surface, which results in more oxygen vacancies to interact with the target gas and enhance the selectivity.

(c) The formation of heterostructures or composites with other oxides or 2-D materials can form abundant oxygen vacancies and create more active sites for the interaction. This can control the Fermi level and transfer the electrons from a higher energy level to a lower energy level, leading to increased response value and fast response.

(d) Light illumination/irradiation could help to achieve high sensor response and fast T_{res}/T_{rec} at RT by generating photo-induced electron–hole pairs on the MoO$_3$ surface via the chemisorption process.

Although there has been extraordinary progress in designing gas sensors using novel nanostructures, there are still many challenges and problems toward achieving high sensing performance, reproducible synthesis process, high selectivity, miniaturization of the sensor, and power consumption/operation temperature. This is very important because the mass-scale production of sensor devices requires a reliable and reproducible process. One of the key challenges is the durability of the sensor at RT since humidity is the main interference in a room temperature sensor. Thus, from a practical point of view, it is important to investigate the sensing performance under different humid conditions to establish the relationship between the sensing properties and the environmental conditions. Another key challenge is the selectivity or the interference of gases, which can often hinder the sensing performance.

There have been few reports on gas sensors for detecting specific gases but not all gases, and sometimes, the detection of a specific gas out of a mixture of gases is a major concern. In the case of resistance-based sensors, it is difficult to discriminate the gases that can give similar resistive change/response. To enhance the selectivity and remove undesirable confounders, a diffusion filter layer can be made with microporous materials (e.g., zeolite and metal–organic frameworks, active carbon, and polymers (e.g., Nafion65)).[189] In this case, only the filtered molecule can reach the surface of the sensing material. Güntner et al.[190] demonstrated superior selective sensing toward formaldehyde using zeolite membranes. With a zeolite Mobile-Five (MFI)/Al_2O_3 membrane, the Pd-doped SnO_2 sensor displayed astounding selectivity ($>$100) for formaldehyde (down to 30 ppb) at 90% relative humidity.

Lastly, the important aspect to consider is OT in the case of MoO_3-based gas sensors. Undoubtedly, temperature plays a vital role in SMOx-based gas sensors to achieve fast response/recovery speed and high sensitivity. At low temperatures, the reaction rate on the metal oxide surface is sluggish, resulting in poor sensor response. By increasing the temperature, the thermal energy given is high enough to overcome the activation energy barrier for the surface reaction; thus, the reaction rate increases and the sensor displays increasing response to the target gas. However, in order to achieve high sensor response, we need to compromise the power consumption. To solve this issue, the idea of a low-powered or self-powered microheater has been proposed with advanced MEMS technology so as to achieve the best possible sensing performance with less power consumption. In addition, an in-depth study of the gas sensing mechanism of MoO_3 nanostructures and metal oxides is still needed. Several models and hypotheses on the metal oxide-based gas sensing system are described by researchers but there is no such model that works for an wide range of gas molecules. Additional analysis may be needed by some advanced tools such as DFT or first principles study.

In conclusion, the key motive of this review was not only to summarize the state-of-the-art but also to inspire readers and excite curiosity, driving them to further investigate MoO_3-based gas sensors. Future directions for understanding more about MoO_3-based nanostructures, their sensing mechanism, and future applications have been discussed.

Conflicts of interest

There are no conflicts to declare.

Acknowledgements

References

1 T. Hong, J. Kim and M. Lee, *Appl. Energy*, 2018, **228**, 1707–1713.
2 L. Pang, J. Zhang, X. Cao, X. Wang, J. Liang, L. Zhang and L. Guo, *Indoor Air*, 2020, ina.12746.

3 K. Santhanam and N. Ahamed, *ChemEng.*, 2018, **2**, 38.
4 R. Malik, V. K. Tomer and N. Joshi, *ACS Appl. Mater. Interfaces*, 2018, **10**, 34087–34097.
5 R. Malik, V. K. Tomer and V. Chaudhary, *Functionalized Graphene Nanocomposites and their Derivatives*, Elsevier, 2019, pp. 323–338.
6 H. Chojer, P. T. B. S. Branco, F. G. Martins, M. C. M. Alvim-Ferraz and S. I. V. Sousa, *Sci. Total Environ.*, 2020, **727**, 138385.
7 R. S. Andre, R. C. Sanfelice, A. Pavinatto, L. H. C. Mattoso and D. S. Correa, *Mater. Des.*, 2018, **156**, 154–166.
8 E. G. Snyder, T. H. Watkins, P. A. Solomon, E. D. Thoma, R. W. Williams, G. S. W. Hagler, D. Shelow, D. A. Hindin, V. J. KiFarmu and P. W. Preuss, *Environ. Sci. Technol.*, 2013, **47**, 11369–11377.
9 V. K. Tomer and S. Duhan, *Sens. Actuators, B*, 2016, **223**, 750–760.
10 R. Malik, V. K. Tomer, V. Chaudhary, M. S. Dahiya, P. S. Rana, S. P. Nehra and S. Duhan, *ChemistrySelect*, 2016, **1**, 3247–3258.
11 J. He, L. Xu, P. Wang and Q. Wang, *Integr. VLSI J.*, 2017, **58**, 286–294.
12 S. Feng, F. Farha, Q. Li, Y. Wan, Y. Xu, T. Zhang and H. Ning, *Sensors*, 2019, **19**, 3760.
13 R. Malik, V. K. Tomer, N. Joshi, V. Chaudhary and L. Lin, in *Nanosensors for Smart Cities*, ed. P. K. S. B. Han, V. K. Tomer, T. A. Nguyen and A. Farmani, Elsevier, 2020, pp. 251–266.
14 R. Malik, V. K. Tomer, V. Chaudhary, M. S. Dahiya, S. P. Nehra, S. Duhan and K. Kailasam, *Sens. Actuators, B*, 2018, **255**, 3564–3575.
15 R. Malik, V. K. Tomer, V. Chaudhary, M. S. Dahiya, S. P. Nehra, P. S. Rana and S. Duhan, *Sens. Actuators, B*, 2017, **239**, 364–373.
16 S. De Vito, G. Di Francia, E. Esposito, S. Ferlito, F. Formisano and E. Massera, *Pattern Recognit. Lett.*, 2020, **136**, 264–271.
17 F. Wu, T. Wu and M. Yuce, *Sensors*, 2018, **19**, 21.
18 A. Mirzaei, S. G. Leonardi and G. Neri, *Ceram. Int.*, 2016, **42**, 15119–15141.
19 R. Kumar, *Eur. J. Mol. Clin. Med.*, 2020, **7**, 3438–3441.
20 P. K. Mishra, R. Malik, V. K. Tomer and N. Joshi, *Functional Nanomaterials: Advances in gas sensing technologies*, Springer, Singapore, 2020, pp. 285–302.
21 V. K. Tomer, S. Devi, R. Malik, S. P. Nehra and S. Duhan, *Sens. Actuators, B*, 2016, **229**, 321–330.
22 R. Malik, V. K. Tomer, V. Chaudhary, N. Joshi and S. Duhan, *Metal Oxide Nanocomposites*, Wiley, 2020, pp. 265–301.
23 M. S. Kamal, S. A. Razzak and M. M. Hossain, *Atmos. Environ.*, 2016, **140**, 117–134.
24 C. Wang, L. Yin, L. Zhang, D. Xiang and R. Gao, *Sensors*, 2010, **10**, 2088–2106.
25 Y. Jian, W. Hu, Z. Zhao, P. Cheng, H. Haick, M. Yao and W. Wu, *Nano-Micro Lett.*, 2020, **12**, 1–43.
26 N. Joshi, V. K. Tomer, R. Malik and J. Nie, *Functional Nanomaterials: Advances in gas sensing technologies*, Springer, Singapore, 2020, pp. 143–159.

27 Y.-F. Sun, S.-B. Liu, F.-L. Meng, J.-Y. Liu, Z. Jin, L.-T. Kong and J.-H. Liu, *Sensors*, 2012, **12**, 2610–2631.

28 V. Kumar, K. H. Kim, P. Kumar, B. H. Jeon and J. C. Kim, *Coord. Chem. Rev.*, 2017, **342**, 80–105.

29 D. J. Wales, J. Grand, V. P. Ting, R. D. Burke, K. J. Edler, C. R. Bowen, S. Mintova and A. D. Burrows, *Chem. Soc. Rev.*, 2015, **44**, 4290–4321.

30 E. Llobet, *Sens. Actuators, B*, 2013, **179**, 32–45.

31 V. K. Tomer and S. Duhan, *Appl. Phys. Lett.*, 2015, **106**, 063105.

32 S. M. Majhi, A. Mirzaei, H. W. Kim, S. S. Kim and T. W. Kim, *Nano Energy*, 2021, **79**, 105369.

33 R. Malik, V. K. Tomer, Y. K. Mishra and L. Lin, *Appl. Phys. Rev.*, 2020, **7**, 021301.

34 V. K. Tomer, R. Malik, V. Chaudhary, A. Baruah and L. Kienle, *Noble Metal-Metal Oxide Hybrid Nanoparticles*, Elsevier, 2019, pp. 283–302.

35 Y. Wu, N. Joshi, S. Zhao, H. Long, L. Zhou, G. Ma, B. Peng, O. N. Oliveira, A. Zettl and L. Lin, *Appl. Surf. Sci.*, 2020, **529**, 147110.

36 I. A. de Castro, R. S. Datta, J. Z. Ou, A. Castellanos-Gomez, S. Sriram, T. Daeneke and K. Kalantar-zadeh, *Adv. Mater.*, 2017, **29**, 1701619.

37 Z. Wei and S. Zhuiykov, *Nanoscale*, 2019, **11**, 15709–15738.

38 H. J. Lunk and H. Hartl, *ChemTexts*, 2017, **3**, 1–23.

39 Z. Lei, X. Yang, J. Dong and X. Yi, *Chem. Mater.*, 2009, **21**, 5681–5690.

40 H. Ren, S. Sun, J. Cui and X. Li, *Cryst. Growth Des.*, 2018, **18**, 6326–6369.

41 P. Song, Q. Wang, J. Li and Z. Yang, *Sens. Actuators, B*, 2013, **181**, 620–628.

42 S. Alizadeh and S. A. Hassanzadeh-Tabrizi, *Ceram. Int.*, 2015, **41**, 10839–10843.

43 H. Peelaers, M. L. Chabinyc and C. G. Van De Walle, *Chem. Mater.*, 2017, **29**, 2563–2567.

44 L. Cheng, M. Shao, X. Wang and H. Hu, *Chem. – Eur. J.*, 2009, **15**, 2310–2316.

45 Y. Zhao, J. Liu, Y. Zhou, Z. Zhang, Y. Xu, H. Naramoto and S. Yamamoto, *J. Phys.: Condens. Matter*, 2003, **15**, L547.

46 M. B. Sreedhara, H. S. S. R. Matte, A. Govindaraj and C. N. R. Rao, *Chem. – Asian J.*, 2013, **8**, 2430–2435.

47 J. H. Kim, J. K. Dash, J. Kwon, C. Hyun, H. Kim, E. Ji and G. H. Lee, *2D Mater.*, 2019, **6**, 015016.

48 Y. Gong, Y. Dong, B. Zhao, R. Yu, S. Hu and Z. Tan, *J. Mater. Chem. A*, 2020, **8**, 978–1009.

49 K. Inzani, T. Grande, F. Vullum-Bruer and S. M. Selbach, *J. Phys. Chem. C*, 2016, **120**, 8959–8968.

50 A. Chithambararaj, N. S. Sanjini, S. Velmathi and A. Chandra Bose, *Phys. Chem. Chem. Phys.*, 2013, **15**, 14761–14769.

51 S. Balendhran, S. Walia, H. Nili, J. Z. Ou, S. Zhuiykov, R. B. Kaner, S. Sriram, M. Bhaskaran and K. Kalantar-zadeh, *Adv. Funct. Mater.*, 2013, **23**, 3952–3970.

52 Y. Zhu, Y. Yao, Z. Luo, C. Pan, J. Yang, Y. Fang, H. Deng, C. Liu, Q. Tan, F. Liu and Y. Guo, *Molecules*, 2019, **25**, 18.

53 J. Wang, Q. Zhou, S. Peng, L. Xu and W. Zeng, *Front. Chem*, 2020, **8**, 339.

54 M. Morales-Luna, S. A. Tomás, M. A. Arvizu, M. Pérez-González and E. Campos-Gonzalez, *J. Alloys Compd.*, 2017, **722**, 938–945.

55 A. A. Mane and A. V. Moholkar, *Appl. Surf. Sci.*, 2017, **405**, 427–440.

56 S. Yang, G. Lei, Z. Lan, W. Xie, B. Yang, H. Xu, Z. Wang and H. Gu, *Int. J. Hydrogen Energy*, 2019, **44**, 7725–7733.

57 H. Yan, P. Song, S. Zhang, Z. Yang and Q. Wang, *RSC Adv.*, 2015, **5**, 72728–72735.

58 E. Comini, L. Yubao, Y. Brando and G. Sberveglieri, *Chem. Phys. Lett.*, 2005, **407**, 368–371.

59 D. Kwak, M. Wang, K. J. Koski, L. Zhang, H. Sokol, R. Maric and Y. Lei, *ACS Appl. Mater. Interfaces*, 2019, **11**, 10697–10706.

60 Q. Wei, P. Song, Z. Li, Z. Yang and Q. Wang, *Vacuum*, 2019, **162**, 85–91.

61 A. Dey, *Mater. Sci. Eng., B*, 2018, **229**, 206–217.

62 A. Bag and N. E. Lee, *J. Mater. Chem. C*, 2019, **7**, 13367–13383.

63 S. Ud-Din, M. Z. Ahmad, K. Qureshi, I. A. Bhatti, M. Zahid, J. Nisar, M. Iqbal and M. Abbas, *Mater. Res. Bull.*, 2018, **100**, 120–130.

64 S. Shen, X. Zhang, X. Cheng, Y. Xu, S. Gao, H. Zhao, X. Zhou and L. Huo, *ACS Appl. Nano Mater.*, 2019, **2**, 8016–8026.

65 Q. Fu, J. Chen, C. Shi and D. Ma, *ACS Appl. Mater. Interfaces*, 2013, **5**, 6024–6029.

66 L. P. Babu Reddy, H. G. Rajprakash and Y. T. Ravikiran, *AIP Conference Proceedings*, American Institute of Physics Inc., 2019, vol. 2142, p. 070022.

67 J. Song, X. Ni, L. Gao and H. Zheng, *Mater. Chem. Phys.*, 2007, **102**, 245–248.

68 A. Ashok, S. N. Vijayaraghavan, S. V. Nair and M. Shanmugam, *RSC Adv.*, 2017, **7**, 48853–48860.

69 K. E. Lee, L. Liu and T. L. Kelly, *J. Phys. Chem. C*, 2014, **118**, 27735–27741.

70 H. U. Kim, J. Son, A. Kulkarni, C. Ahn, K. S. Kim, D. Shin, G. Y. Yeom and T. Kim, *Nanotechnology*, 2017, **28**, 175601.

71 S. A. Khalate, R. S. Kate, H. M. Pathan and R. J. Deokate, *J. Solid State Electrochem.*, 2017, **21**, 2737–2746.

72 J. Zhang, P. Song, Z. Li, S. Zhang, Z. Yang and Q. Wang, *J. Alloys Compd.*, 2016, **685**, 1024–1033.

73 X. Fu, P. Yang, X. Xiao, D. Zhou, R. Huang, X. Zhang, F. Cao, J. Xiong, Y. Hu, Y. Tu, Y. Zou, Z. Wang and H. Gu, *J. Alloys Compd.*, 2019, **797**, 666–675.

74 K. Xu, W. Wei, Y. Sun, W. Lu, T. Yu, Y. Yang and C. Yuan, *Powder Technol.*, 2019, **345**, 633–642.

75 K. He, S. He, W. Yang and Q. Tian, *J. Alloys Compd.*, 2019, **808**, 151704.

76 R. Nadimicherla, H. Y. Li, K. Tian and X. Guo, *Solid State Ionics*, 2017, **300**, 128–134.

77 H. Ji, W. Zeng and Y. Li, *Phys. E*, 2019, **114**, 113646.

78 D. Chen, M. Liu, L. Yin, T. Li, Z. Yang, X. Li, B. Fan, H. Wang, R. Zhang, Z. Li, H. Xu, H. Lu, D. Yang, J. Sun and L. Gao, *J. Mater. Chem.*, 2011, **21**, 9332–9342.

79 S. S. Kalanur, I. H. Yoo and H. Seo, *Sens. Actuators, B*, 2017, **247**, 357–365.

80 F. Ji, X. Ren, X. Zheng, Y. Liu, L. Pang, J. Jiang and S. Liu, *Nanoscale*, 2016, **8**, 8696–8703.

81 D. Wang, Y. Cheng, K. Wan, J. Yang, J. Xu and X. Wang, *Vacuum*, 2020, **179**, 109487.

82 X. Luo, K. You, Y. Hu, S. Yang, X. Pan, Z. Wang, W. Chen and H. Gu, *Int. J. Hydrogen Energy*, 2017, **42**, 8399–8405.

83 L. L. Sui, Y. M. Xu, X. F. Zhang, X. L. Cheng, S. Gao, H. Zhao, Z. Cai and L. H. Huo, *Sens. Actuators, B*, 2015, **208**, 406–414.

84 Y. Liu and W. Zeng, *J. Mater. Sci.: Mater. Electron.*, 2016, **27**, 12996–13001.

85 N. Joshi, L. F. da Silva, F. M. Shimizu, V. R. Mastelaro, J. C. M'Peko, L. Lin and O. N. Oliveira, *Microchim. Acta*, 2018, **185**(4), 213, DOI: 10.1007/s00604-019-3532-4.

86 N. Joshi, L. F. Da Silva, H. Jadhav, J. C. M'Peko, B. B. Millan Torres, K. Aguir, V. R. Mastelaro and O. N. Oliveira, *RSC Adv.*, 2016, **6**, 92655–92662.

87 N. Joshi, L. F. da Silva, H. S. Jadhav, F. M. Shimizu, P. H. Suman, J. C. M'Peko, M. O. Orlandi, J. G. Seo, V. R. Mastelaro and O. N. Oliveira, *Sens. Actuators, B*, 2018, **257**, 906–915.

88 N. Joshi, V. Saxena, A. Singh, S. P. Koiry, A. K. Debnath, M. M. Chehimi, D. K. Aswal and S. K. Gupta, *Sens. Actuators, B*, 2014, **200**, 227–234.

89 N. Joshi, M. L. Braunger, F. M. Shimizu, A. Riul and O. N. Oliveira, *Two-Dimensional Transition Metal Dichalcogenides for Gas Sensing Applications*, Springer, Cham, 2020, pp. 131–155.

90 K. Wetchakun, T. Samerjai, N. Tamaekong, C. Liewhiran, C. Siriwong, V. Kruefu, A. Wisitsoraat, A. Tuantranont and S. Phanichphant, *Sens. Actuators, B*, 2011, **160**, 580–591.

91 N. Joshi, T. Hayasaka, Y. Liu, H. Liu, O. N. Oliveira and L. Lin, *Microchim. Acta*, 2018, **185**, 1–16.

92 T. Wagner, S. Haffer, C. Weinberger, D. Klaus and M. Tiemann, *Chem. Soc. Rev.*, 2013, **42**, 4036–4053.

93 M. M. Xavier, P. R. Nair and S. Mathew, *Analyst*, 2019, **144**, 1475–1491.

94 C. Dong, R. Zhao, L. Yao, Y. Ran, X. Zhang and Y. Wang, *J. Alloys Compd.*, 2020, **820**, 153194.

95 S. Yang, C. Jiang and S. Huai Wei, *Appl. Phys. Rev.*, 2017, **4**, 021304.

96 S. Yang, Y. Liu, W. Chen, W. Jin, J. Zhou, H. Zhang and G. S. Zakharova, *Sens. Actuators, B*, 2016, **226**, 478–485.

97 S. He, W. Li, L. Feng and W. Yang, *J. Alloys Compd.*, 2019, **783**, 574–582.

98 Y. Liu, S. Yang, Y. Lu, N. V. Podval'naya, W. Chen and G. S. Zakharova, *Appl. Surf. Sci.*, 2015, **359**, 114–119.

99 S. Bai, C. Chen, D. Zhang, R. Luo, D. Li, A. Chen and C. C. Liu, *Sens. Actuators, B*, 2014, **204**, 754–762.

100 S. Yang, Z. Wang, Y. Hu, X. Luo, J. Lei, D. Zhou, L. Fei, Y. Wang and H. Gu, *ACS Appl. Mater. Interfaces*, 2015, **7**, 9247–9253.

101 Z. Li, W. Wang, Z. Zhao, X. Liu and P. Song, *Mater. Sci. Semicond. Process.*, 2017, **66**, 33–38.

102 A. A. Mane and A. V. Moholkar, *Solid-State Electron.*, 2018, **139**, 21–30.

103 S. Yang, Y. Liu, T. Chen, W. Jin, T. Yang, M. Cao, S. Liu, J. Zhou, G. S. Zakharova and W. Chen, *Appl. Surf. Sci.*, 2017, **393**, 377–384.

104 F. Qu, X. Zhou, B. Zhang, S. Zhang, C. Jiang, S. Ruan and M. Yang, *J. Alloys Compd.*, 2019, **782**, 672–678.

105 Z. Li, P. Song, Z. Yang and Q. Wang, *Ceram. Int.*, 2018, **44**, 3364–3370.

106 S. Yang, Z. Wang, Y. Zou, X. Luo, X. Pan, X. Zhang, Y. Hu, K. Chen, Z. Huang, S. Wang, K. Zhang and H. Gu, *Sens. Actuators, B*, 2017, **248**, 160–168.

107 P. Yang, X. Li, H. Huang, S. Yang, X. Zhang, Y. Hu, Z. Wang and H. Gu, *Int. J. Hydrogen Energy*, 2020, **45**, 23841–23850.

108 S. Bai, J. Han, X. Fan, J. Guo, R. Luo, D. Li and A. Chen, *New J. Chem.*, 2020, **44**, 2402–2407.

109 M. M. Mohamed, T. M. Salama, M. Morsy, R. M. A. Shahba and S. H. Mohamed, *Sens. Actuators, B*, 2019, **299**, 126960.

110 B. Geeta Rani, S. Raisri, R. Kailasa, M. Sai Bhargava Reddy, H. Maseed and K. Venkateswara Rao, *J. Mater. Sci.*, 2020, **55**, 8109–8122.

111 S. Kumar, A. Singh, R. Singh, S. Singh, P. Kumar and R. Kumar, *Sens. Actuators, B*, 2020, **325**, 128974.

112 T. Thomas, Y. Kumar, J. A. Ramos Ramón, V. Agarwal, S. Sepúlveda Guzmán, R. Reshmi, S. Pushpan, S. L. Loredo and K. C. Sanal, *Vacuum*, 2021, **184**, 109983.

113 S. Bai, C. Chen, M. Cui, R. Luo, A. Chen and D. Li, *RSC Adv.*, 2015, **5**, 50783–50789.

114 B. Mandal, Aaryashree, M. Das, M. Than Htay and S. Mukherjee, *Mater. Res. Bull.*, 2019, **109**, 281–290.

115 X. Chu, S. Liang, W. Sun, W. Zhang, T. Chen and Q. Zhang, *Sens. Actuators, B*, 2010, **148**, 399–403.

116 G. T. Santos, A. A. Felix and M. O. Orlandi, *Surfaces*, 2020, **4**, 9–16.

117 R. Xu, N. Zhang, L. Sun, C. Chen, Y. Chen, C. Li and S. Ruan, *RSC Adv.*, 2016, **6**, 106364–106369.

118 R. Malik and V. K. Tomer, *Renewable Sustainable Energy Rev.*, 2021, **135**, 110235.

119 Y. Wu, Q. Huang, J. Nie, J. Liang, N. Joshi, T. Hayasaka, S. Zhao, M. Zhang, X. Wang and L. Lin, *J. Nanosci. Nanotechnol.*, 2019, **19**, 5310–5316.

120 H. Liu, Y. Liu, Y. Chu, T. Hayasaka, N. Joshi, Y. Cui, X. Wang, Z. You and L. Lin, *Sens. Actuators, B*, 2018, **263**, 94–102.

121 V. K. Tomer, R. Malik and N. Joshi, *J. Nanosci. Nanotechnol.*, 2019, **19**, 5052–5053.

122 Y. Han, D. Huang, Y. Ma, G. He, J. Hu, J. Zhang, N. Hu, Y. Su, Z. Zhou, Y. Zhang and Z. Yang, *ACS Appl. Mater. Interfaces*, 2018, **10**, 22640–22649.

123 S. Yang, G. Lei, L. Tan, H. Xu, J. Xiong, Z. Wang and H. Gu, *J. Alloys Compd.*, 2021, **877**, 160200.

124 A. Gusain, N. J. Joshi, P. V. Varde and D. K. Aswal, *Sens. Actuators, B*, 2017, **239**, 734–745.

125 A. Mekki, N. Joshi, A. Singh, Z. Salmi, P. Jha, P. Decorse, S. Lau-Truong, R. Mahmoud, M. M. Chehimi, D. K. Aswal and S. K. Gupta, *Org. Electron.*, 2014, **15**, 71–81.

126 A. Singh, A. Kumar, A. Kumar, S. Samanta, N. Joshi, V. Balouria, A. K. Debnath, R. Prasad, Z. Salmi, M. M. Chehimi, D. K. Aswal and S. K. Gupta, *Appl. Phys. Lett.*, 2013, **102**, 132107.

127 A. Singh, Z. Salmi, N. Joshi, P. Jha, A. Kumar, H. Lecoq, S. Lau, M. M. Chehimi, D. K. Aswal and S. K. Gupta, *RSC Adv.*, 2013, **3**, 5506–5523.

128 S. Thomas, N. Joshi and V. K. Tomer, *Functional Nanomaterials: Advances in Gas Sensing Technologies*, Springer Singapore, Singapore, 2020.

129 V. K. Tomer, N. Thangaraj, S. Gahlot and K. Kailasam, *Nanoscale*, 2016, **8**, 19794–19803.

130 V. K. Tomer, P. V. Adhyapak, S. Duhan and I. S. Mulla, *Microporous Mesoporous Mater.*, 2014, **197**, 140–147.

131 R. Malik, P. S. Rana, V. K. Tomer, V. Chaudhary, S. P. Nehra and S. Duhan, *Microporous Mesoporous Mater.*, 2016, **225**, 245–254.

132 V. K. Tomer, R. Malik and K. Kailasam, *ACS Omega*, 2017, **2**, 3658–3668.

133 R. Malik, V. Chaudhary, V. K. Tomer, P. S. Rana, S. P. Nehra and S. Duhan, *Ceram. Int.*, 2016, **42**, 10892–10901.

134 R. Malik and V. K. Tomer, *J. Mater. Chem. A*, 2018, **6**, 10718–10730.

135 V. K. Tomer, K. Singh, H. Kaur, M. Shorie and P. Sabherwal, *Sens. Actuators, B*, 2017, **253**, 703–713.

136 V. K. Tomer and S. Duhan, *Sens. Actuators, B*, 2015, **220**, 192–200.

137 V. K. Tomer, R. Malik and V. Chaudhary, *Appl. Mater. Today*, 2019, **16**, 193–203.

138 R. Malik, V. K. Tomer, V. Chaudhary, M. S. Dahiya, A. Sharma, S. P. Nehra, S. Duhan and K. Kailasam, *J. Mater. Chem. A*, 2017, **5**, 14134–14143.

139 C. Anichini, W. Czepa, D. Pakulski, A. Aliprandi, A. Ciesielski and P. Samorì, *Chem. Soc. Rev.*, 2018, **47**, 4860–4908.

140 E. Poonia, P. K. Mishra, V. Kiran, J. Sangwan, R. Kumar, P. K. Rai, R. Malik, V. K. Tomer, R. Ahuja and Y. K. Mishra, *J. Mater. Chem. C*, 2019, **7**, 5477–5487.

141 J. Nie, Y. Wu, Q. Huang, N. Joshi, N. Li, X. Meng, S. Zheng, M. Zhang, B. Mi and L. Lin, *ACS Appl. Mater. Interfaces*, 2019, **11**, 1699–1705.

142 Y. Wang, R. Zhang, Z. Zhang, J. Cao and T. Ma, *Adv. Mater. Interfaces*, 2019, **6**, 1901429.

143 R. K. Jha and N. Bhat, *Adv. Mater. Interfaces*, 2020, **7**, 1901992.

144 F. Rahman, A. Zavabeti, M. A. Rahman, A. Arash, A. Mazumder, S. Walia, S. Sriram, M. Bhaskaran and S. Balendhran, *ACS Appl. Mater. Interfaces*, 2019, **11**, 40189–40195.

145 H. Yan, P. Song, S. Zhang, J. Zhang, Z. Yang and Q. Wang, *Sens. Actuators, B*, 2016, **236**, 201–207.

146 Z. Tang, X. Deng, Y. Zhang, X. Guo, J. Yang, C. Zhu, J. fan, Y. Shi, B. Qing and F. Fan, *Sens. Actuators, B*, 2019, **297**, 126730.

147 X. Gao, Q. Ouyang, C. Zhu, X. Zhang and Y. Chen, *ACS Appl. Nano Mater.*, 2019, **2**, 2418–2425.

148 H. M. M. Munasinghe Arachchige, D. Zappa, N. Poli, N. Gunawardhana and E. Comini, *Sens. Actuators, B*, 2018, **269**, 331–339.

149 D. Chen, M. Liu, L. Yin, T. Li, Z. Yang, X. Li, B. Fan, H. Wang, R. Zhang, Z. Li, H. Xu, H. Lu, D. Yang, J. Sun and L. Gao, *J. Mater. Chem.*, 2011, **21**, 9332–9342.

150 A. A. Felix, R. A. Silva and M. O. Orlandi, *CrystEngComm*, 2020, **22**, 4640–4649.

151 J. Shen, S. Guo, C. Chen, L. Sun, S. Wen, Y. Chen and S. Ruan, *Sens. Actuators, B*, 2017, **252**, 757–763.

152 H. Y. Li, L. Huang, X. X. Wang, C. S. Lee, J. W. Yoon, J. Zhou, X. Guo and J. H. Lee, *RSC Adv.*, 2017, **7**, 3680–3685.

153 R. Pandeeswari and B. G. Jeyaprakash, *Biosens. Bioelectron.*, 2014, **53**, 182–186.

154 A. A. Mane, S. A. Nikam and A. V. Moholkar, *Mater. Chem. Phys.*, 2018, **216**, 294–304.

155 S. Farzi-kahkesh, M. B. Rahmani and A. Fattah, *Mater. Sci. Semicond. Process.*, 2020, **120**, 105263.

156 H. Ma, H. Fang, W. Wu, C. Zheng, L. Wu and H. Wang, *RSC Adv.*, 2020, **10**, 25467–25474.

157 W. Jiang, D. Wei, S. Zhang, X. Chuai, P. Sun, F. Liu, Y. Xu, Y. Gao, X. Liang and G. Lu, *New J. Chem.*, 2018, **42**, 15111–15120.

158 D. K. Halwar, V. V. Deshmane and A. V. Patil, *Mater. Res. Express*, 2019, **6**, 105913.

159 V. K. Tomer, S. Duhan, A. K. Sharma, R. Malik, S. P. Nehra and S. Devi, *Colloids Surf., A*, 2015, **483**, 121–128.

160 A. Kumar, N. Joshi, S. Samanta, A. Singh, A. K. Debnath, A. K. Chauhan, M. Roy, R. Prasad, K. Roy, M. M. Chehimi, D. K. Aswal and S. K. Gupta, *Sens. Actuators, B*, 2015, **206**, 653–662.

161 S. Duhan and V. K. Tomer, in *Advanced Sensor and Detection Materials*, ed. A. Tiwari and M. M. Demir, John Wiley and Sons Ltd, 2014, pp. 149–192.

162 V. K. Tomer, S. Devi, R. Malik, S. P. Nehra and S. Duhan, *Microporous Mesoporous Mater.*, 2016, **219**, 240–248.

163 V. K. Tomer, S. Duhan, P. V. Adhyapak and I. S. Mulla, *J. Am. Ceram. Soc.*, 2015, **98**, 741–747.

164 V. K. Tomer and S. Duhan, *Sens. Actuators, B*, 2015, **212**, 517–525.

165 P. V. Adhyapak, S. P. Meshram, V. Tomar, D. P. Amalnerkar and I. S. Mulla, *Ceram. Int.*, 2013, **39**, 7367–7378.

166 Y. Li, *Phys. E*, 2017, **94**, 22–24.

167 H. Ji, W. Zeng and Y. Li, *Mater. Res. Bull.*, 2019, **118**, 110476.

168 Y. Sun, L. Chen, Y. Wang, Z. Zhao, P. Li, W. Zhang, Y. Leprince-Wang and J. Hu, *J. Mater. Sci.*, 2017, **52**, 1561–1572.

169 V. K. Tomer and S. Duhan, *J. Mater. Chem. A*, 2016, **4**, 1033–1043.

170 J. Wang, Q. Zhou, Z. Wei, L. Xu and W. Zeng, *Ceram. Int.*, 2020, **46**, 29222–29232.

171 T. Li, W. Zeng, Y. Zhang and S. Hussain, *Mater. Lett.*, 2015, **160**, 476–479.

172 L. Sui, X. Song, X. Cheng, X. Zhang, Y. Xu, S. Gao, P. Wang, H. Zhao and L. Huo, *CrystEngComm*, 2015, **17**, 6493–6503.

173 Y. Xia, C. Wu, N. Zhao and H. Zhang, *Mater. Lett.*, 2016, **171**, 117–120.

174 H. Li, D. Zhu, Z. Yang, W. Lu and Y. Pu, *Appl. Surf. Sci.*, 2019, **489**, 384–391.

175 Y. Xu, J. Yang, J. Liu, B. Li and L. Han, *Dalton Trans.*, 2020, **49**, 8114–8121.

176 J. Hu, M. Zhang, X. Wang, Y. Sun, P. Li, W. Zhang, K. Lian, L. Chen and Y. Chen, *RSC Adv.*, 2017, **7**, 23478–23485.

177 H. Qin, J. Xie, H. Xu, Y. Li and Y. Cao, *Mater. Res. Bull.*, 2017, **93**, 256–263.

178 H. Qin, Y. Cao, J. Xie, H. Xu and D. Jia, *Sens. Actuators, B*, 2017, **242**, 769–776.

179 S. Wang, J. Xie, J. Hu, H. Qin and Y. Cao, *Appl. Surf. Sci.*, 2020, **512**, 145722.

180 L. Sui, X. Zhang, X. Cheng, P. Wang, Y. Xu, S. Gao, H. Zhao and L. Huo, *ACS Appl. Mater. Interfaces*, 2017, **9**, 1661–1670.

181 F. Zhang, X. Dong, X. Cheng, Y. Xu, X. Zhang and L. Huo, *ACS Appl. Mater. Interfaces*, 2019, **11**, 11755–11762.

182 W. I. Lee, M. Bonyani, J. K. Lee, C. Lee and S. B. Choi, *Curr. Appl. Phys.*, 2018, **18**, S60–S67.

183 K. Xu, S. Duan, Q. Tang, Q. Zhu, W. Zhao, X. Yu, Y. Yang, T. Yu and C. Yuan, *CrystEngComm*, 2019, **21**, 5834–5844.

184 X. Gao, C. Li, Z. Yin and Y. Chen, *RSC Adv.*, 2015, **5**, 37703–37709.

185 L. Zhu, W. Zeng, Y. Li and J. Yang, *Phys. E*, 2019, **106**, 170–175.

186 W. Jiang, L. Meng, S. Zhang, X. Chuai, Z. Zhou, C. Hu, P. Sun, F. Liu, X. Yan and G. Lu, *Sens. Actuators, B*, 2019, **299**, 126888.

187 J. Zhang, P. Song, J. Li, Z. Yang and Q. Wang, *Sens. Actuators, B*, 2017, **249**, 458–466.

188 R. Kumar, W. Zheng, X. Liu, J. Zhang and M. Kumar, *Adv. Mater. Technol.*, 2020, **5**, 1901062.

189 H. Singh, V. K. Tomer, N. Jena, I. Bala, N. Sharma, D. Nepak, A. De Sarkar, K. Kailasam and S. K. Pal, *J. Mater. Chem. A*, 2017, **5**, 21820–21827.

190 A. T. Güntner, S. Abegg, K. Wegner and S. E. Pratsinis, *Sens. Actuators, B*, 2018, **257**, 916–923.

191 J. Li, L. Wang, H. Liu, J. Zhao, X. Li, H. Wei and Y. Han, *J. Alloys Compd.*, 2017, **694**, 939–945.

192 J. Li, H. Liu, H. Fu, L. Xu, H. Jin, X. Zhang, L. Wang and K. Yu, *J. Alloys Compd.*, 2019, **788**, 248–256.

193 Y. Mo, Z. Tan, L. Sun, Y. Lu and X. Liu, *J. Alloys Compd.*, 2020, **812**, 152166.

194 X. Li, D. Jiang, Y. Fan, N. Zhang, C. Liu, S. Adimi, J. Zhou, S. Wen and S. Ruan, *Inorg. Chem. Front.*, 2020, 7, 1704–1712.

195 D. Jiang, W. Wei, F. Li, Y. Li, C. Liu, D. Sun, C. Feng and S. Ruan, *RSC Adv.*, 2015, **5**, 39442–39448.

196 Z. Li, W. Wang, Z. Zhao, X. Liu and P. Song, *RSC Adv.*, 2017, 7, 28366–28372.

197 H. Fu, Z. Wu, X. Yang, P. He, X. An, S. Xiong and D. Han, *Appl. Surf. Sci.*, 2021, **542**, 148721.

198 S. Zhang, P. Song, J. Zhang, Z. Li, Z. Yang and Q. Wang, *RSC Adv.*, 2016, **6**, 50423–50430.